

DISSERTATION

# Oxide layer design for transparent electrodes and charge transport components

carried out for the purpose of obtaining the degree of

**Dr.techn.**

by

**Dipl.-Ing. Selina Götz**

Matrikelnummer 01225379

submitted at TU Wien at the Institute of Applied Physics,  
in collaboration with the AIT Austrian Institute of Technology GmbH

under the supervision of

Univ.Prof. Dipl.-Ing. Dr.techn. Markus Valtiner

and

Dr. Theodoros Dimopoulos

Wien, February 2023



Ich erkläre an Eides statt, dass ich die vorliegende Dissertation selbstständig und ohne fremde Hilfe unter der Betreuung von Univ. Prof. Dipl.-Ing. Dr.techn. Markus Valtiner und Dr. Theodoros Dimopoulos verfasst habe. Es wurden keine anderen als die angegebenen Quellen und Hilfsmittel benutzt bzw. die wörtlich oder sinngemäß entnommenen Stellen als solche kenntlich gemacht.

Wien, February 7, 2023



*Für meine Eltern*



*Herr Janosch, soll man 10 000 Schritte am Tag gehen?  
"Wenn man nicht zu schreiten weiß, helfen auch 100 000 Schritte nichts. Wondrak  
hingegen setzt vollendet einen Fuß vor den anderen. Deswegen reicht bei ihm ein  
Schritt am Tag. Ein toller Schritt wohlgemerkt."  
- Janosch*



---

## ACKNOWLEDGEMENTS

---

Firstly, I want to thank Prof. Markus Valtiner for his excitement about so many topics which enabled this collaboration as well as for introducing me to his lab at TU Wien. In this regard I want to thank Dominik Dworschak and Martin Wess for patiently teaching and helping me with the ICP-MS setup.

Another thanks goes to Giovanni Ligorio from Humboldt Universität zu Berlin and David Stock at University of Innsbruck for performing the XPS and UPS measurements and for taking the time to analyse the data and explain the results. Then I would like to acknowledge the fruitful collaboration with Toby Meyer and Stéphanie Narbey from Solaronix who contributed their materials and experience to the successful development of the perovskite solar cells. And in this regard, I also want to acknowledge the contribution of our colleagues at Plansee, Jörg Winkler, Christian Linke, and Enrico Franzke by developing the sputtering targets that were essential for this thesis.

Further, I would like to thank the AIT Austrian Institute of Technology and especially the ECH (former PVS) unit for granting my position for the past years.

My foremost biggest thanks goes to Theodoros Dimopoulos who always supported me, guided me and encouraged me in all my questions and doubts. I appreciate everything you taught me and that you never lose your sense of humor.

However, my time would have been just half as enjoyable without the rest of the group. So, thank you Stefan, Domenico, Philipp, Ankit, Christiane, and especially Maximilian for countless shared lunches, cakes, coffee breaks and all other pleasant distractions.





---

## CONTENTS

---

Kurzfassung	ix
Abstract	xi
1 INTRODUCTION	1
1.1 Motivation	1
1.2 Working principle of solar cells and OLEDs	2
1.3 The role of transition metal oxides in optoelectronics	4
1.3.1 General electronic structure	4
1.3.2 Energy level alignment and the importance of the work function	5
1.3.3 Oxide layer fabrication by sputter deposition	5
1.4 Transparent electrodes	6
1.5 Aim and structure of the thesis	7
2 MOLYBDENUM OXIDE	9
2.1 Characterization of Molybdenum Oxide thin films	10
2.1.1 DC magnetron sputtering of MoO <sub>x</sub>	10
2.1.2 Crystal structure and annealing effects	13
2.2 Transparent electrodes based on Molybdenum Oxide	14
2.2.1 DMD electrode architecture	14
2.2.2 Surface morphology, electronic structure and composition	17
2.2.3 Mechanical, thermal and chemical stability	19
2.3 Summary	21
3 MOLYBDENUM TITANIUM OXIDE – MTO	23
3.1 Characterization of MTO thin films	25
3.1.1 DC magnetron sputtering of MTO	25
3.1.2 Crystal structure and annealing effects	27
3.2 Transparent electrodes based on MTO	29
3.2.1 DMD electrode architecture	29
3.2.2 Surface morphology, electronic structure and composition	32
3.2.3 Mechanical and chemical stability	36
3.3 Summary	37
4 WATER STABILITY OF MOLYBDENUM OXIDE AND MTO	39
4.1 Dissolution experiments	40
4.1.1 The stability of MoO <sub>x</sub> in liquid water	40

4.1.2	Comparing the stability of MTO and MoO <sub>x</sub>	42
4.2	Humidity-driven degradation	43
4.3	Summary	51
5	NIOBIUM-DOPED TITANIUM OXIDE – TNO	53
5.1	Characterization of TNO thin films	54
5.1.1	DC magnetron sputtering of TNO	54
5.1.2	Crystal structure and annealing effects	56
5.2	Transparent electrodes based on TNO	57
5.2.1	DMD architecture	57
5.2.2	Surface morphology, electronic structure and composition	60
5.2.3	Mechanical stability	64
5.3	Mesoporous titanium oxide	65
5.4	Summary	68
6	DEVICES	69
6.1	Perovskite solar cells	69
6.1.1	p-i-n structure using MTO	70
6.1.2	mesoporous n-i-p structure using TNO	71
6.2	Organic light-emitting diodes (OLEDs)	73
6.2.1	mesoporous n-i-p architecture using TNO	74
6.2.2	p-i-n architecture using MTO	75
6.3	Summary	77
7	CONCLUSIONS AND OUTLOOK	79
8	APPENDIX	81
8.1	Methods and Instrumentation	81
8.1.1	Materials and deposition methods	81
8.1.2	Sample characterization	83
8.1.3	Optical simulations	85
8.1.4	Tauc method	85
8.2	Copyright clearances	86
	Bibliography	90
	List of Publications	106

---

## KURZFASSUNG

---

Die Entwicklung von optoelektronischen Bauelementen der nächsten Generation wie Solarzellen und Leuchtdioden (OLEDs) beinhaltet deren Übertragung auf flexible Substrate für eine kostengünstige, industrielle Herstellung sowie für neuartige flexible Anwendungen, die leichte, biegsame Lösungen für die Energie- oder Lichterzeugung bieten. Zu den größten Herausforderungen gehören die Suche nach geeigneten Materialien und Bauteilen, die vielen Biegezyklen standhalten, aber auch die Senkung der Verarbeitungstemperaturen unter  $\sim 100^\circ\text{C}$  da die meisten flexiblen Substrate keine höheren Temperaturen vertragen.

Diese Anforderungen haben die Suche nach hochflexiblen transparenten Elektroden vorangetrieben. Trotz der Knappheit von Indium ist der derzeitige kommerzielle Standard für transparente Elektroden Indium-Zinn-Oxid (ITO), das auf Glassubstraten einen niedrigen Flächenwiderstand und eine hohe Transparenz aufweist. Bei der Übertragung auf flexible Substrate verringert sich jedoch die Transparenz und Leitfähigkeit aufgrund der niedrigeren Verarbeitungstemperaturen, und die Elektrode versagt aufgrund der Sprödigkeit des Materials schnell unter Biegebeanspruchung.

In dieser Arbeit werden drei Metalloxide für den Einsatz in flexiblen transparenten Elektroden untersucht. Die dünnen Oxidschichten werden durch Magnetronspütern abgeschieden, einer kontrollierbaren Herstellungstechnik, die mit industriellen Produktionsstandards und den Anforderungen flexibler Substrate kompatibel ist. Die einzelnen Oxidschichten werden für Oxid/Metall/Oxid (DMD) Schichtmaterialien optimiert und bieten hohe Transparenz im sichtbaren Spektrum durch destruktive Interferenz des reflektierten Lichts und gute elektrische Leitfähigkeit durch die dünne Metallschicht.

Bei den untersuchten Oxiden handelt es sich um Molybdänoxid ( $\text{MoO}_x$ ), ein gemischtes Molybdän-Titanoxid (MTO) und niob-dotiertes Titanoxid (TNO). Sie werden auf starren (Glas) und flexiblen (PET) Substraten abgeschieden und hinsichtlich ihrer Transmission im Sichtbaren, ihres elektrischen Schichtwiderstands sowie ihrer mechanischen und chemischen Stabilität charakterisiert. Vor allem auf PET zeigen die DMD-Elektroden eine bessere Leistung (unter Berücksichtigung ihrer Transparenz und ihres Schichtwiderstands) als kommerzielle ITO-Elektroden. Darüber hinaus weisen die DMD-Elektroden eine deutlich höhere mechanische Stabilität bei Biegetests auf, da der relative Widerstand nach mehreren tausend Biegezyklen nur um einen Faktor 3 ansteigt, während die kommerzielle

ITO-Elektrode bereits nach einigen hundert Biegungszyklen einen Anstieg des relativen Widerstands auf das Tausendfache erfährt.

Hinsichtlich der chemischen Stabilität wird festgestellt, dass das gesputterte  $\text{MoO}_x$  in flüssigem Wasser und in feuchten Umgebungsbedingungen extrem instabil ist, was zur Auflösung der Schicht und zur Veränderung der Materialeigenschaften führt. Im Gegensatz dazu wird das  $\text{MoO}_3$  in MTO durch das Titan stabilisiert, wodurch die Reaktions- und Auflösungsraten in Feuchtigkeit bzw. Wasser verringert werden.

Da  $\text{MoO}_x$  und  $\text{TiO}_2$  bereits als geeignete Materialien für Loch-/ Elektronen-Transportschichten in Solarzellen und LEDs bekannt sind, bestand die Idee darin, diese Materialien so einzusetzen, dass sie gleichzeitig als transparente Elektrode und Ladungstransportkomponente fungieren können. Zu diesem Zweck werden die entwickelten DMD-Elektroden in Prototypen von Perowskit-Solarzellen und organischen LEDs eingesetzt. Obwohl die Charakterisierung der Zellen darauf hindeutet, dass der direkte Ladungstransport durch Grenzflächendefekte im Oxid behindert wird, liefert die Leistung der DMDs in Kombination mit herkömmlichen Ladungstransportschichten vielversprechende Ergebnisse und die Materialien zeigen so ihr Potenzial als transparente Elektroden für flexible Bauelemente.

---

## ABSTRACT

---

The development of next-generation optoelectronic devices like solar cells and organic light-emitting diodes (OLEDs) involves their transfer onto flexible substrates for low-cost industrial fabrication as well as for novel flexible applications, offering light-weight, bendable solutions for energy or light generation. The main challenges include the search for suitable materials and device components that can withstand many bending cycles but also the reduction of processing temperatures below  $\sim 100^\circ\text{C}$  since most flexible substrates do not tolerate higher temperatures.

These requirements have driven the search for highly flexible transparent electrodes. Despite the scarcity of indium, the current commercial standard for transparent electrodes is indium-tin-oxide (ITO), which provides low resistivity and high transparency on glass substrates. However, when transferred to flexible substrates, the general performance is decreased because of lower processing temperatures and the electrode quickly fails under bending due to the intrinsic brittleness of the material.

In this thesis three metal oxides are investigated for the use in flexible transparent electrodes. Thin oxide films are deposited via magnetron sputtering at room temperature providing a controllable fabrication technique that is compatible with industrial production standards and the requirements of flexible substrates. The single oxide layers are optimized for dielectric/metal/dielectric (DMD) stacks, providing visible transparency through destructive interference of the reflected light and good electrical conductivity through the thin metal layer.

The studied oxides comprise molybdenum oxide ( $\text{MoO}_x$ ), a mixed molybdenum titanium oxide (MTO) and niobium-doped titanium oxide (TNO). They are deposited on rigid (glass) and flexible (PET) substrates and characterized in terms of visible transmittance, electrical sheet resistance as well as mechanical and chemical stability. Especially on PET, the DMD electrodes show higher figure of merit (taking their transparency and sheet resistance into account) than the commercial ITO. Moreover, the DMD electrodes show significantly higher mechanical stability under bending, resulting in an increase of relative resistance below 3 after several thousand bending cycles, where the commercial ITO electrode showed detrimental failure with an increase above 1000.

Concerning the chemical stability it is found that the sputtered  $\text{MoO}_x$  is extremely unstable in liquid water and humid conditions, leading to disintegration of the layer and

changes of material properties. In contrast, in MTO the  $\text{MoO}_3$  is stabilized by the presence of titanium, lowering the reaction and dissolution rate in humidity and water, respectively.

Finally, since  $\text{MoO}_x$  and  $\text{TiO}_2$  are already known as suitable materials for hole/electron transport layers in solar cells and LEDs, the idea was to use these materials such that they can simultaneously act as transparent electrode and charge transport component. To this end, the developed DMD electrodes are implemented in prototype perovskite solar cells and organic LEDs. Although the device characterization suggests that direct charge transport is inhibited by interfacial defects in the oxide, the performance of the DMDs in combination with traditional charge transport layers yields promising results showing their potential as transparent electrodes for flexible devices.

---

## INTRODUCTION

---

### 1.1 MOTIVATION

The issue of climate and energy crisis has become an omnipresent topic, which influences our daily life and every-day decisions. Whether it concerns the general reduction of energy and resource consumption, the transition to renewable energy sources or avoiding the use of critical materials in our electronic products, the wide set of challenges on the way towards a more sustainable future is known to everyone by this time. The urgency and importance of these issues motivated the work behind this thesis. Without going into further details, it is implied that the search for sustainable and low-cost energy sources and efficient electronics contributes to tackling the aforementioned challenges and that it has driven the research on next-generation solar cells and organic light-emitting diodes (OLEDs), which are investigated in this thesis.

Both, solar cells and OLEDs, are based on semiconductor materials connected with two electrodes. In fact, they have very similar stack architectures but operate in opposite direction: while a solar cell absorbs light to generate electrical current, an OLED uses electrical current to emit light. Their basic device structure is, however, the same: a p-n or a p-i-n junction. In a solar cell, photogenerated charges (electrons and holes) are separated at the junction and subsequently extracted at the respective electrode, whereas in the OLED case, electrons and holes are injected from the electrodes, recombine and, as a result, light is emitted. The more efficient these charges are transported across the junction, the more efficient the device will operate. Finding compatible materials that have suitable electronic and optical properties to achieve efficient light absorption/emission and charge extraction/injection has been the core of recent developments in optoelectronics. Additional challenges comprise compatibility with flexible substrates and large-scale fabrication techniques, e.g., roll-to-roll production, which mainly constrain the device thickness and processing temperatures [1, 2]. Besides the demands for industrial production, flexible substrates and devices also offer new opportunities in terms of device operation and integration. Being light-weight, cost-effective and possibly even semitransparent, flexible solar cells could be more easily incorporated in facades, foils and fabrics. This way, new and large areas would become available for photovoltaic energy generation (e.g., building-

or device-integrated photovoltaics, smart windows, and space applications).

This has led to third generation optoelectronic devices including organic or hybrid perovskite solar cells and LEDs [3, 4, 5, 6] which are based on solution-processable thin films as active material. With only a few hundred nanometers of thickness, they are compatible with the demands for flexible applications and have achieved promising device efficiencies already in the early stages [7], continuously reporting record efficiencies (currently at 25.5% [8]) since then. However, there are some challenges that still have to be resolved before their commercialisation. This mainly concerns stability issues of the active material itself [9, 10] as well as of the adjacent charge transport layers but also the replacement of scarce or brittle materials such as indium oxide [11]. Since the devices are layered stacks consisting of different materials, there are many possibilities for innovation and optimization.

## 1.2 WORKING PRINCIPLE OF SOLAR CELLS AND OLEDs

For the conversion of light into electricity, firstly, light has to be absorbed in the solar cell. This occurs when the band gap energy of the semiconducting absorber material is equal or smaller than the energy of the incoming photon. Given the solar spectrum, with its maximal intensity in the visible wavelength range, a suitable band gap ( $\lesssim 2$  eV) is the main energetic restriction for an efficient absorber material. If this is the case, the incoming photon can excite an electron from the valence band to the conduction band, creating an electron-hole pair. In the following, it is essential to separate the electrons from the holes before they recombine. This separation is achieved by combining a p-type and an n-type semiconductor, forming a p-n junction. The carrier concentration gradient in the depletion region creates an electric field which counteracts the diffusion of charges across the junction. When an electron-hole pair is created, the charges are ideally swept across the p-n junction before they can recombine. Successfully separated charges can then be collected by the opposite electrodes. For an efficient charge separation and collection, the energy band alignment of the p-type and n-type semiconductor interface and of the adjacent electrodes is essential.

To determine the efficiency of a photovoltaic device, we want to evaluate how much of the incoming light is converted into electrical energy. To this end, a bias is applied to the solar cell and the current-voltage (IV) curves are analysed in dark and illuminated conditions. From these IV-curves, the most important parameters can be derived, such as the open-circuit voltage ( $V_{OC}$ ), the short-circuit current ( $I_{SC}$ ) and the maximum power point (MPP), as illustrated in Figure 1.1. The fill factor (FF), which is derived from these parameters, is a key measure for the deviation from the ideal diode behavior, mainly caused by parasitic resistances, namely the series and shunt resistance,  $R_S$  and  $R_{sh}$ . The



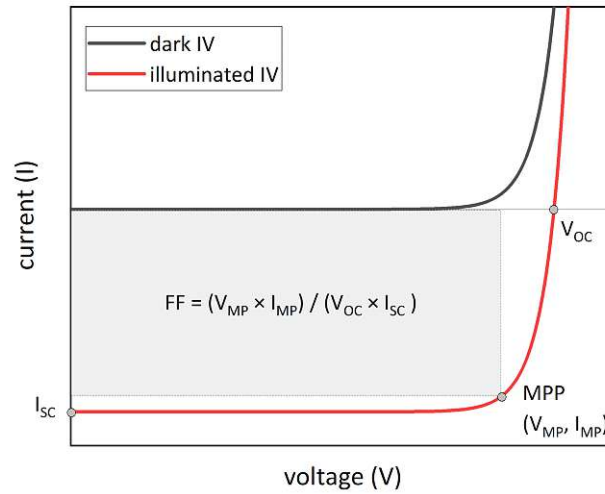


**Figure 1.1:** Schematic IV-curves of a solar cell in dark and illuminated conditions, including the most essential solar cell parameters.

series resistance originates from ohmic resistances of each material and their contacts, whereas the shunt resistance is caused by manufacturing defects, allowing the light-induced current to bypass the diode. To avoid a reduction of the fill factor, a small series resistance is required, while the shunt resistance should be as high as possible. Finally, the solar cell efficiency  $\eta$  is determined as:

$$\eta = \frac{I_{SC} \cdot V_{OC} \cdot FF}{P_{in}}$$

where  $P_{in}$  is the input power of the incident light, standardized to  $1000 \text{ W/m}^2$ .

The emerging thin film photovoltaic devices based on organic or perovskite absorbers are better described as p-i-n junctions, where the 'i' refers to an undoped ('intrinsic') semiconductor layer which is sandwiched between a p-type and an n-type material. When in contact, the Fermi levels of the p-i-n layer align, causing a shift in the energy levels that promotes charge separation.

Similarly, organic LEDs (OLEDs) also consist of a p-i-n structure, where the lowest unoccupied molecular orbital (LUMO) of the intrinsic semiconductor is aligned with the n-type layer/cathode and the highest occupied molecular orbital (HOMO) is aligned with the p-type layer/anode. But instead of collecting the charges created by light, the charge carriers are injected into the active layer, where they can recombine to emit light. Here, the band gap energy determines the wavelength, i.e., the colour of the emitted light. To analyse the performance of OLEDs, not only the IV-curves are measured to characterize their electrical behaviour, but also the luminance is acquired to determine

the amount of light that is emitted. The luminance introduces another key parameter for OLED performance: the turn-on voltage, i.e., the applied bias necessary to overcome a certain luminance threshold (in this thesis 1 cd/m<sup>2</sup>). The smaller the turn-on voltage, the smoother the energy band alignment of the different layers and the more efficient the charge carrier injection. The efficiency of an OLED will be reported as current efficacy, obtained by dividing the luminance by the current density, yielding a measure of how much light is emitted per input current.

### 1.3 THE ROLE OF TRANSITION METAL OXIDES IN OPTOELECTRONICS

#### 1.3.1 General electronic structure

The use of transition metal oxides (TMOs) in (opto)electronics stems predominantly from their particular electronic structure. Due to the ionic character of oxides, the total density of states can often be separated in contributions from the O 2*p* and the metal *d* orbitals. Although a detailed understanding of the energy bands requires the computation of orbital hybridization, the general electronic features of most TMOs can be well described by considering the *d*-band occupancy. The O 2*p* states are completely filled and form the majority of the valence band, while the conduction band has mainly *d* band character. The occupancy of *d* bands can be related to the average oxidation state and determines the electronic character of the oxide, as presented in Figure 1.2. TMOs with totally empty *d* bands are insulators, which is the case for the completely stoichiometric oxides, e.g. TiO<sub>2</sub>, MoO<sub>3</sub>, WO<sub>3</sub>.

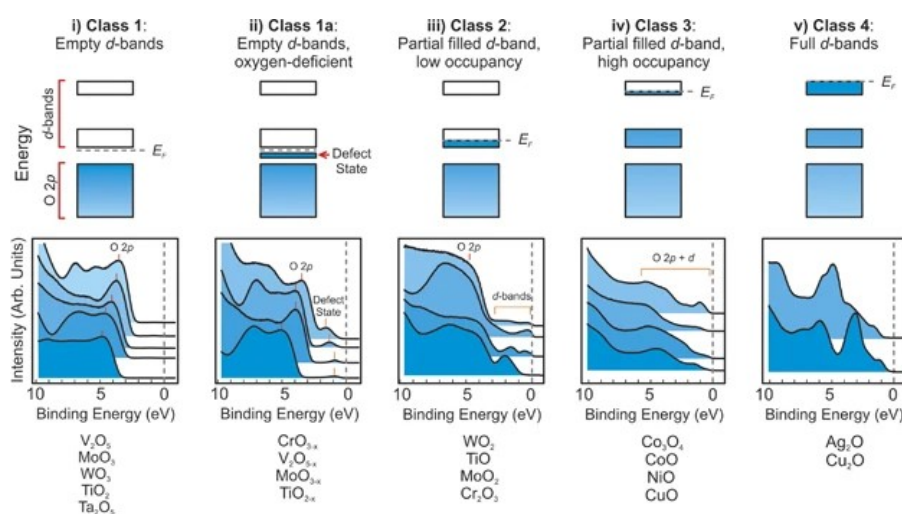


**Figure 1.2:** Schematic energy band diagrams of various transition metal oxides, reproduced with permission (8.2) from [12].

However, they have a natural tendency to form an oxygen deficiency, making them primarily n-type materials. With increasing oxygen deficiency, a defect state is formed within the band gap, arising from a shallow filling of metal  $d$  states ( $\text{TiO}_{2-x}$ ,  $\text{MoO}_{3-x}$ ) and making them semiconducting. When the  $d$  states are partially occupied, the electronic structure becomes metallic or semi-metallic, being the case for e.g.  $\text{TiO}$ ,  $\text{MoO}_2$ ,  $\text{WO}_2$ . When the number of electrons in the  $d$  bands becomes larger, the electronic properties are determined by electron-electron interactions, yielding Mott-Hubbard insulators (e.g.  $\text{NiO}$ ,  $\text{CuO}$ ) [12].

### 1.3.2 Energy level alignment and the importance of the work function

For devices like solar cells, thin film transistors or organic LEDs to operate efficiently, the energetic barrier for charge extraction/injection between the electrode and the active material needs to be as small as possible. To achieve close alignment of the respective energy levels, thin oxide buffer layers are often introduced to facilitate the charge transfer across the interfaces. Because of the broad diversity in electronic properties of TMOs, they are particularly versatile buffer layers for all types of electrodes. The decisive parameter for energy alignment is the oxide's work function [13]. Metal oxides with high work function are used as hole transport material for anodes, including for instance  $\text{MoO}_3$ ,  $\text{WO}_3$  and  $\text{NiO}$ . The low-work-function TMOs on the other hand are used as electron transport buffer layers at the cathode, predominantly  $\text{TiO}_2$  and  $\text{ZnO}$  [14, 12].

### 1.3.3 Oxide layer fabrication by sputter deposition

Metal oxides can be deposited using various vapour- and solution-phase techniques, each having their advantages in terms of controllability, scalability and costs [15]. One common technique for depositing (semi)conducting metal oxides is magnetron sputtering. The main advantages include the possibility of film growth at room temperature, and a precise control of film thickness and composition via the deposition parameters, such as sputtering power and pressure.

To date, sputter deposition of oxide layers generally involves two of the following sputtering modes: reactive DC mode sputtering from a metallic target or RF sputtering from an oxide target. While the latter enables direct sputtering of insulating materials in their targeted composition, the former technique involves reaction processes at the target surface, the gas phase and on the substrate surface [16]. During reactive sputtering, oxygen is added to the process gas such that the metal atoms react with the oxygen and an oxide film is formed. Although the specific reactions can be complex, the average oxygen content in the film can be directly controlled via the oxygen partial pressure. Both options usually lead to a decreased deposition rate, making the technique less appealing

for industrial purposes, where high deposition rates of several nm/min are required, e.g. for roll-to-roll manufacturing.

#### 1.4 TRANSPARENT ELECTRODES

The efficient operation of optoelectronic devices like solar cells and OLEDs largely depends on the performance of transparent electrodes. The challenge is to efficiently conduct electrical current while transmitting as much light as possible. The most commonly applied transparent electrode is tin-doped indium oxide (ITO). Its wide band gap ( $>3.5$  eV), high charge carrier density ( $\sim 10^{21}$  cm<sup>3</sup>) and high mobility ( $\sim 20 - 100$  cm<sup>2</sup>/V/s) make it a unique material for this purpose [17, 18]. However, due to the scarcity and high cost of indium, other transparent conductive oxides have been explored to complement ITO on the electronics market, the most popular being fluorine-doped tin oxide (FTO) and Aluminium- or Gallium-doped zinc oxide (AZO, GZO) [17, 19, 20]. These oxides have different electronic properties which is another point of consideration for the implementation in devices.

When aiming for flexible applications, these transparent conductive oxides have common disadvantages: they are rather brittle, they require a certain thickness to achieve low resistivity and, often, elevated deposition or annealing temperatures ( $<200^\circ\text{C}$ ) are involved which damage most flexible substrates like Polyethylenterephthalat (PET), Polyethylen-naphthalat (PEN), polycarbonate, or cellulose-based foils. Although flexible ITO electrodes are commercially available, the performance of ITO on PET is drastically reduced as compared to glass because of the omitted high-temperature processing, leading to higher sheet resistance and lower average transmittance. Furthermore, due to the thickness of hundreds of nanometers and the brittleness of the oxides, bending leads to the formation of cracks which impede the flow of electrical current. Alternatives for flexible transparent electrodes include metal networks and nanowires, carbon nanotubes and graphene, or organic semiconductors like PEDOT:PSS [21, 22].

Another compelling solution that is sometimes overlooked is presented in the form of oxide/metal/oxide triple layers [20]. In this case, a thin metal layer reduces the sheet resistance and it preserves the conductivity under bending due to its intrinsically high ductility. The transmittance can be maximized by choosing the oxide thicknesses such that destructive interference of the reflected light is achieved (see Figure 1.3)[21]. To this end, several configurations using ITO, AZO, GZO, FTO and many more have been investigated [21, 20, 23].

Furthermore, as the metal interlayer yields very good lateral conductivity such that the oxide layer does not have to be highly conductive itself, also non-conductive layers can

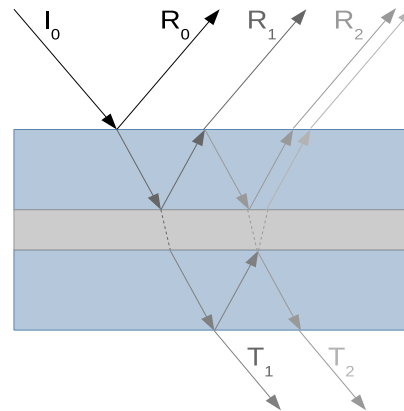


**Figure 1.3:** Schematic representation of the internal reflections within an oxide/metal/oxide stack.  $I_0$  is the incoming light, which is partially reflected ( $R_0$ ) at the first interface. Another part is transmitted but is again partially reflected at the oxide/metal interface and contributes to the overall reflectance when passing the first interface as  $R_1$ . The overall transmittance ( $T_1, T_2, \dots$ ) is maximized by choosing the oxide thickness such that the reflected light  $R_0, R_1, R_2, \dots$  interferes destructively.

be used to form a dielectric/metal/dielectric (DMD) structure. This offers a much wider range of materials to tailor the optical properties of the transparent electrode without loss of conductivity. The early DMD structures have been studied for application as transparent heat-mirrors using  $\text{TiO}_2/\text{Ag}/\text{TiO}_2$  stacks that show high reflectivity ( $<90\%$ ) in the near infra red while having high transmittance ( $>80\%$ ) in the visible regime [24]. Since then, DMD structures have also been studied as transparent electrodes using various high refractory metal oxides, mainly including transition metal oxides like  $\text{ZnO}$ ,  $\text{TiO}_2$ ,  $\text{MoO}_3$ ,  $\text{WO}_3$  [25, 26, 27, 28, 29, 30, 31, 32]. This gives an additional advantage in terms of device-specific design of the electrode. When using DMD electrodes as cathode, it is beneficial to choose a dielectric with low work function, whereas for an anode, the work function should be high to facilitate charge carrier transport. In this way, the transparent electrode additionally undertakes the role of a charge transport layer, where the top dielectric layer replaces the oxide buffer layer.

## 1.5 AIM AND STRUCTURE OF THE THESIS

In the present thesis, different transition metal oxides are investigated for the use in DMD electrodes which simultaneously act as selective charge transport layers. More specifically, the focus lies on abundant transition metal oxides that have the potential to make transparent electrodes a more sustainable component for optoelectronic devices in terms of material criticality and production costs, and ideally increase the device efficiency by suitable energy band alignment. In chapters 2, 3, and 5 the properties of the sputtered oxide layers are characterized and optimized for the use in the DMD

transparent electrodes. The objective is to use sputter deposition at room temperature and at high deposition rates to ensure compatibility with flexible (plastic) substrates and industrial large-scale fabrication. With this, it is intended to develop a viable alternative to the commercial ITO. Chapter 4 focuses on the stability of the TMO layers in humidity and water. The surface reactions with water influence not only the durability for further processing and long-term reliability but also important electronic properties like the oxide's work function. This can have an impact on the applicability in optoelectronic devices. The implementation of the DMD electrodes in flexible perovskite solar cells and organic LEDs is finally shown in chapter 6. The experimental details, used methods and materials are all summarized in the Appendix 8.1.

---

## MOLYBDENUM OXIDE

---

*Partial results of the work presented in this chapter have been published in:*

*Goetz, S. et al. Fast sputter deposition of MoO<sub>x</sub>/metal/MoO<sub>x</sub> transparent electrodes on glass and PET substrates. Journal of Materials Science 56, 9047–9064 (2021). [33], reproduced under the corresponding copyright agreement (8.2).*

Molybdenum oxides comprise a large family of materials with different stoichiometries and corresponding properties. Depending on the oxygen deficiency, there exists a range from stoichiometric MoO<sub>3</sub> (with Mo<sup>6+</sup> oxidation state), to MoO<sub>2</sub> (with Mo<sup>4+</sup> oxidation state). While MoO<sub>3</sub> is an n-type semiconductor with wide band gap (~3 eV), MoO<sub>2</sub> is reported to have significantly lower band gap or (semi-)metallic properties [34, 35, 36]. In between these stoichiometries, oxygen-deficient oxides, such as Mo<sub>9</sub>O<sub>26</sub>, Mo<sub>18</sub>O<sub>52</sub> or Mo<sub>4</sub>O<sub>11</sub>, have an average oxidation state between 6+ and 4+. As the oxygen deficiency increases, the band gap is lowered and states are induced within the band gap, which leads to broad optical absorption around 900 nm and changes the visual appearance of the oxide from transparent (MoO<sub>3</sub>) to blue (MoO<sub>3-x</sub>) [36, 37]. In MoO<sub>3</sub> the valence band consists mainly of O 2p orbitals while the conduction band is dominated by the empty Mo 4d orbitals. As oxygen is removed, the Mo 4d states are partially occupied and the increasing amount of metallic Mo-Mo bonds finally leads to the predicted metallic behaviour of MoO<sub>2</sub> [38]. The electronic band structure gives MoO<sub>3</sub> its high work function (between 4.7 and 6.9 eV [14, 39, 40]), making it a compelling hole-extraction or hole-injection layer in solar cells and organic LEDs [41]. This wide range in the reported work function values is mainly caused by surface reactions with water, when MoO<sub>3</sub> is exposed to ambient conditions [42, 40]. As will be discussed in more detail in Chapter 4, MoO<sub>3</sub> has a high affinity to react with humidity, leading to larger variations in the work functions. Furthermore, variations in the oxidation state as well as in the crystal structure also lead to different work function values [39].

The most stable crystal phase of stoichiometric MoO<sub>3</sub> is the orthorhombic  $\alpha$ -phase, which is characterized by a stratified (two dimensional) morphology. This is composed of double layer sheets of distorted MoO<sub>6</sub> octahedra, held together in the vertical direction by weak Van der Waals forces [43]. The MoO<sub>6</sub> building block is common even for amorphous

$\text{MoO}_x$  (having a local coordination, without the long-range order), where the octahedra are connected via vertices instead of edges [40].

In this chapter, sputtered  $\text{MoO}_3$  layers are investigated. With a properly engineered  $\text{MoO}_x$  target, providing high electrical conductivity and compactness, it was possible to deposit all layers in direct current (DC) magnetron sputtering mode, leading to high deposition rates for  $\text{MoO}_3$ , which are compatible with industrial scale production.  $\text{MoO}_3$ -based dielectric/metal/dielectric (DMD) transparent electrodes are demonstrated on glass and PET substrates, where the latter shows a higher figure of merit than the reported evaporated electrodes in the literature.

## 2.1 CHARACTERIZATION OF MOLYBDENUM OXIDE THIN FILMS

### 2.1.1 DC magnetron sputtering of $\text{MoO}_x$

*This section includes additional data that has not been published in [33].*

A suboxide  $\text{MoO}_{2.7}$  target (10.16 cm in diameter) was specially designed by mixing  $\text{MoO}_2$  and  $\text{MoO}_3$  powders as starting material, which were then hot-pressed in a graphite mold. The target was finally machined and bonded onto a copper back plate, as shown in Figure 2.1 (a). This target was used to prepare  $\text{MoO}_x$  thin films (with  $x \leq 3$ ). The electrical conductivity of the target is above  $10^4 \text{ S/m}$ , which enables operation in DC magnetron sputtering mode, leading to high deposition rates that are compatible with industrial fabrication. Unless stated otherwise, a sputtering power of 163 W (corresponding to a power density of  $2 \text{ W/cm}^2$ ) is applied for the deposition, yielding sufficiently high deposition rates without jeopardizing the lifetime of the target. As comparison, for typical

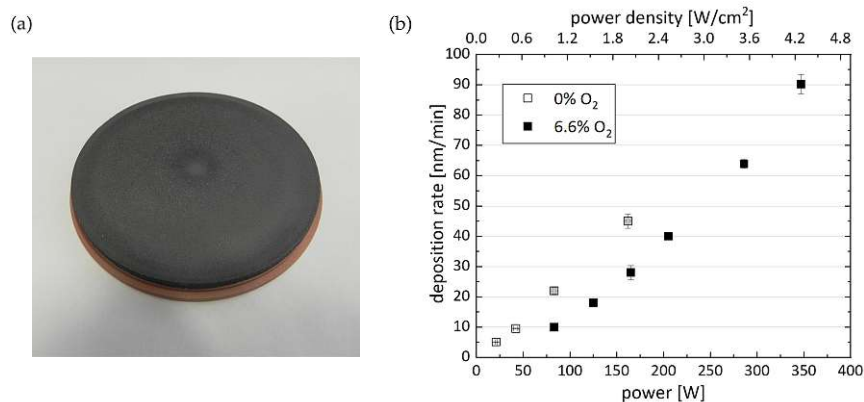


**Figure 2.1:** (a) Photograph of the  $\text{MoO}_{2.7}$  target with the copper back plate. (b) Sputter deposition rates as a function of sputtering power at different oxygen contents.



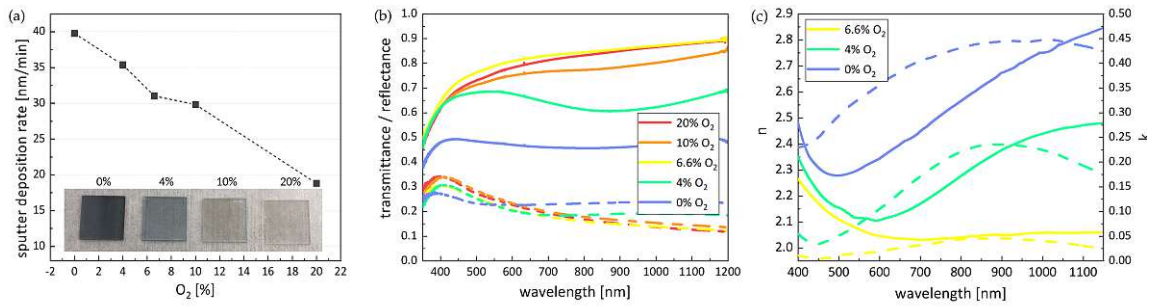


**Figure 2.2:** (a) Sputter deposition rate as a function of oxygen content. The inset shows a photograph of 50 nm thick films sputtered with different oxygen content. (b) Transmittance and reflectance spectra of 50 nm thick films sputtered with 0, 4, 6.6, 10 and 20% O<sub>2</sub>. (c) Refractive index  $n$  and extinction coefficient  $k$  of 0, 4 and 6.6% O<sub>2</sub> samples.

RF sputtering from an insulating MoO<sub>3</sub> target sputtering rates of 1.6 - 4.7 nm/min are reported for the same power density of 2 W/cm<sup>2</sup> [44].

Without the addition of oxygen to the process gas, deposition rates of 45 nm/min (see Figure 2.1 (a)) are achieved. However, in this conditions the sputtered film visually appear dark grey, suggesting increased light absorption and a lack of oxygen. Therefore, in order to obtain transparent films, oxygen is added to the process gas. As the deposition rate generally decreases with increasing content of reactive gas (see Figure 2.2 (a)), only the minimal amount of oxygen is added that can be technically realised with the sputter system (6.6% O<sub>2</sub>). This results in a deposition rate of 31 nm/min, yielding a transparent layer. In fact, it was found that a higher oxygen content in the plasma of 10% and 20% O<sub>2</sub>, respectively, does not further increase the transparency of the layer (see Figure 2.2 (b)). However, without sufficient purging of the gas lines or pre-sputtering of the target, a sample with intermediate oxygen content between 0% and 6.6% was obtained (denoted as 4% O<sub>2</sub>), which is interesting to study in terms of the dependence of optical properties on the oxygen content. Figure 2.2 (b) shows a gradual decrease in transmittance of 50 nm thick films with decreasing oxygen content. The 4% sample demonstrates the impact of oxygen vacancies which generate a broad absorption around 900 nm ([37]). It should be noted at this point, that the small difference between the 10% and 20% is also attributed to a small lack of oxygen due to the sputtering history, leading to an accumulation of reduced Mo on the target surface.

The increased optical absorption is also confirmed when calculating the refractive index using a TMM algorithm 8.1.3. The result is shown in Figure 2.2 (c). While the imaginary part of the refractive index,  $k$ , is negligible for the 6.6% sample, it increases when oxygen is removed from the system. Firstly, a maximum around 900 nm is observed for the 4% sample, which indicates the formation of a defect band around 1.5 eV, related to electrons trapped in oxygen vacancies (also visible in the absorption coefficient  $\alpha$ , shown in Figure

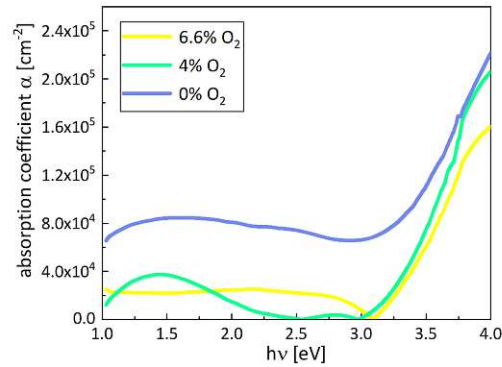


**Figure 2.3:** The absorption coefficient  $\alpha$  for samples sputtered with 0, 4 and 6.6%  $O_2$  as a function of the photon energy

2.3) [45, 46]. The lower oxygen content leads to reduced oxidation states of Mo ( $Mo^{+4}$  and  $Mo^{+5}$ ) which serve as acceptor states. The absorption processes are then associated with a charge transfer from lower to higher Mo oxidation states [37]. A further lack of oxygen (as in the 0% sample) leads to an increase in optical absorption and a broadening over the whole visible range as metallic Mo-Mo bonds are formed and an increased number of electrons occupy the d-d bands [34].

The optical band gap is extracted from the optical spectra using the Tauc method (8.1.4). Assuming an indirect band gap, the reactively sputtered films yield similar values of 2.93, 2.95, 3.01 and 3.0 eV for 4, 6.6, 10, 20%  $O_2$ , respectively. Only the non-reactively sputtered layer (i.e. 0%  $O_2$ ) shows a significantly reduced band gap of 2.53 eV. An error of approx. 0.02 eV can be assumed depending on the fitting range in the linear Tauc fit. All values agree well with the reported values in the literature ranging from 2.4 eV to 3.5 eV, sensitively depending on the oxygen content [43, 47, 14, 48].

Furthermore, the electrical resistivity is obtained from linear current-voltage curves after sputtering Au contacts for an in-line 4-wire resistivity set-up. The measurements confirm the more metallic nature of non-reactively sputtered, suboxidic films yielding a resistivity of  $3 \Omega \cdot \text{cm}$  for a 100 nm thick film. For comparison, the resistivity of a reactively sputtered film with the same thickness is  $350 \Omega \cdot \text{cm}$ . These resistivity values agree with the values in the literature ([45, 34]) and are consistent with the observation that the electrical resistance decreases when oxygen is withdrawn from the system. As the d-d bands are partially filled, the Fermi level shifts to higher energies, leading to an increased conductivity.

### 2.1.2 Crystal structure and annealing effects

The following section is additional data which has not been published elsewhere

All sputtered  $\text{MoO}_x$  layers are amorphous without any additional heat treatment. The XRD patterns show no reflection peaks, irrespective of the oxygen content or the film thickness, as shown in Figure 2.4 (a). The SEM cross-sections in Figure 2.4 (b) confirm the amorphous nature of the thicker films, where no intrinsic nanostructure is visible. The non-reactively sputtered film (0%  $\text{O}_2$ ) appears very dense and shows a 5-10 nm thin top layer with slightly darker contrast. This may be related to a top layer with a higher degree of oxidation due air exposure.

When exposing the films to elevated temperatures (e.g. on a hot plate), they start to crystallise. For 50 nm thin films, first peaks arise in the XRD pattern (not shown) at a temperature of  $300^\circ\text{C}$  and small crystallites start to form. However, the diffraction peaks are rather small and obscure. Thus, further annealing is performed with 300-400 nm thick films at  $350^\circ\text{C}$  for 2 hours in air. As shown in Figure 2.5 (a), distinct reflections are detected after the annealing. The most pronounced reflections correspond to the orthorhombic  $\text{MoO}_3$  phase (COD-1011043). Interestingly, there is a strong preference in the  $(0n0)$  direction, where  $n$  is an even number, i.e. the  $(020)$  at  $12.70^\circ$ ,  $(040)$  at  $25.56^\circ$  and  $(060)$  at  $38.76^\circ$ . Additionally, there are some smaller peaks which can not be assigned to any  $\text{MoO}_x$  phase. Instead, they agree best with a Sodium Molybdenum Oxide,  $\text{Na}_6(\text{Mo}_{10}\text{O}_{33})$  (COD-1534417). This means, that during the annealing process, Na diffuses from the glass substrate to the  $\text{MoO}_3$  film where it reacts and forms a composite crystal

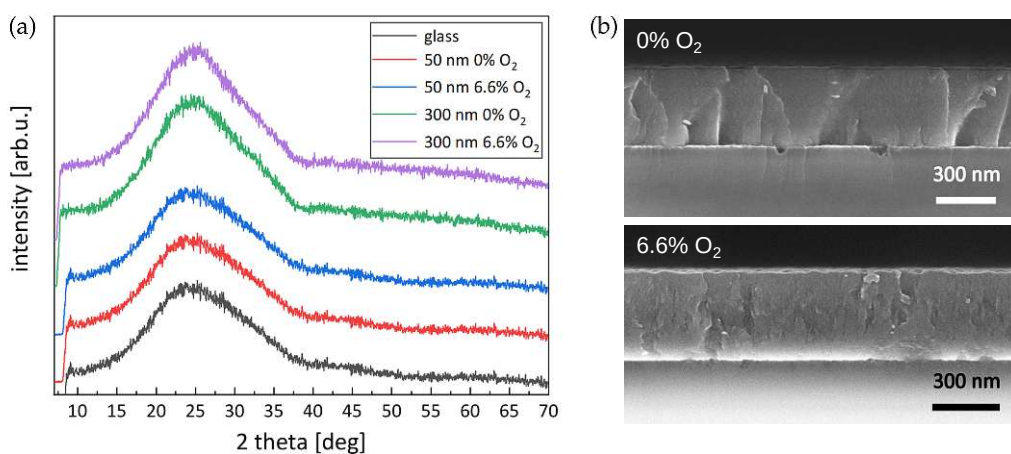


**Figure 2.4:** (a) XRD diffractogram of as-deposited, amorphous films on glass. (b) SEM cross section images of 300 nm thick films sputtered with (bottom) and without oxygen (top).

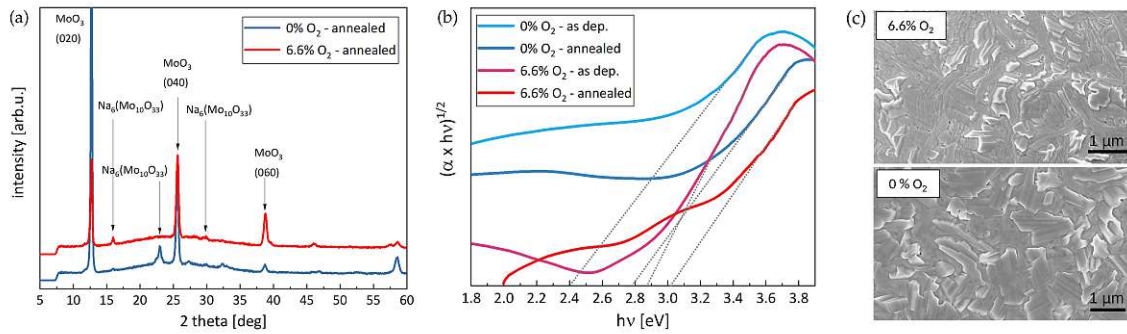


**Figure 2.5:** (a) XRD measurement of 300 nm thick films after annealing for 2 hours at 350°C in air. (b) Tauc plots for indirect transitions of the annealed and as-deposited films. (c) Corresponding SEM images of the annealed films.

phase. Similarly, this  $\text{Na}_6(\text{Mo}_{10}\text{O}_{33})$  phase even dominates the XRD pattern of annealed, 50 nm thin  $\text{MoO}_3$  films, because it is easier to diffuse through a thin  $\text{MoO}_3$  layer. EDX measurements confirm the agglomeration of Na- and Mo-rich crystallites in the annealed samples.

Figure 2.5 (c) shows the Tauc plots before and after the annealing of 300 nm thick  $\text{MoO}_x$  films. For the non-reactively sputtered films, the band gap increases from 2.4 eV to 2.8 eV. As the annealing is performed in air, additional oxygen is incorporated in the film, narrowing the defect band and reducing the absorption. Similarly, for the reactively sputtered film, the band gap increases from 2.9 eV to 3.0 eV after the annealing. In this case, the films becomes fully stoichiometric  $\text{MoO}_3$  as the defect band around 1.5 eV vanishes due to the filling of oxygen vacancies which are still present in the as deposited sample.

## 2.2 TRANSPARENT ELECTRODES BASED ON MOLYBDENUM OXIDE

### 2.2.1 DMD electrode architecture

With  $\text{MoO}_3$  being a known hole transport/injection layer in solar cells and organic LEDs, its implementation as the dielectric layer in dielectric/metal/dielectric (DMD) electrodes could combine the functionality of a transparent electrode and a hole-selective layer.

For the reported DMD electrodes, the  $\text{MoO}_3$ /metal/ $\text{MoO}_3$  architecture is realized with Ag and Au as metal layer. While Ag is the metal of choice concerning low optical losses and lower cost, its lower stability and tendency to react may in turn favour Au as metal layer. When using Ag in the  $\text{MoO}_3$ -based DMD electrode, the Ag film is oxidized during the reactive sputtering of the top  $\text{MoO}_3$  layer, leading to detrimental losses of the electrode's conductivity. Therefore, a work around has been implemented, as depicted in Figure 2.6(a), introducing an additional layer of  $\text{MoO}_x$  sputtered without oxygen,  $D_2$ . This

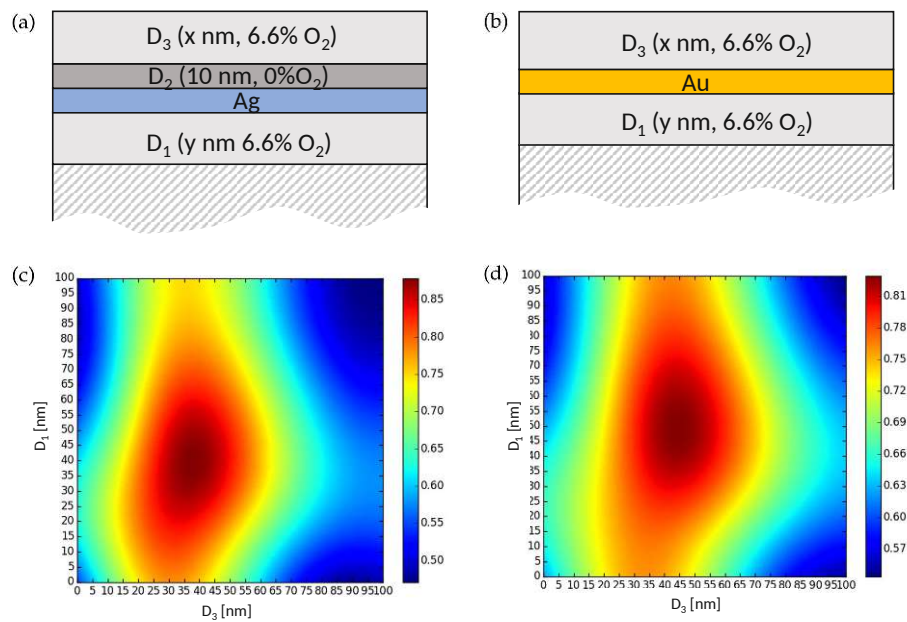


**Figure 2.6:** Schematic representation of the DMD electrode architecture using (a) Ag (where an interfacial layer  $D_2$  is sputtered without  $O_2$ ) and (b) Au as metal layer. (c),(d) TMM simulations where the average optical transmittance (400-700 nm) is calculated for different top and bottom  $MoO_x$  layer thicknesses with Ag and Au as metal layer, respectively.

interfacial layer has to be chosen in a way that minimizes optical losses, but sufficiently protects the underlying Ag from oxidation during the reactive deposition of the top  $MoO_3$  layer,  $D_3$ . Since it was found that the transmittance of non-reactively sputtered  $MoO_x$  increases as the sputter power is decreased, the intermediate layer  $D_2$  is deposited at low power (21 W) to keep the optical losses to a minimum. As a result, the thickness of  $D_2$  is chosen at 10 nm yielding sufficient protection of the Ag layer without compromising the transparency. When using Au as metal layer, no protective interfacial layer is needed. This simplifies the electrode architecture and, thus, reduces the deposition time 2.6 (b). In order to determine the layer thicknesses which maximize the visible transmittance of the DMD electrode, TMM simulations (8.1.3) are performed. The refractive index of the metal layer is taken from literature and the thickness is set to 14 nm for Ag and to 10 nm for Au. The interfacial layer for the case of Ag is omitted for simplicity, assuming a homogeneous top  $MoO_3$  layer in all cases. The refractive index is from 2.2 and the top and bottom  $MoO_3$  thickness is varied from 0 to 100 nm. The results are shown in 2.6 (c-d), yielding a broad window where the average transmittance is maximized (dark red region).

As next step, the DMD electrodes were experimentally realized with the aim to obtain an optimum trade-off between high optical transmittance and low sheet resistance. Figures 2.7 (a) and (b) show the transmittance spectra and the sheet resistance ( $R_s$ ) values for  $D_1(45 \text{ nm})/Ag(t)/D_2(10 \text{ nm})/D_3(35 \text{ nm})$  electrodes, with  $t=10,11,12,14 \text{ nm}$  on the glass and PET substrates, respectively. Sheet resistance values range from 14-5  $\Omega/\text{sq}$ , decreasing

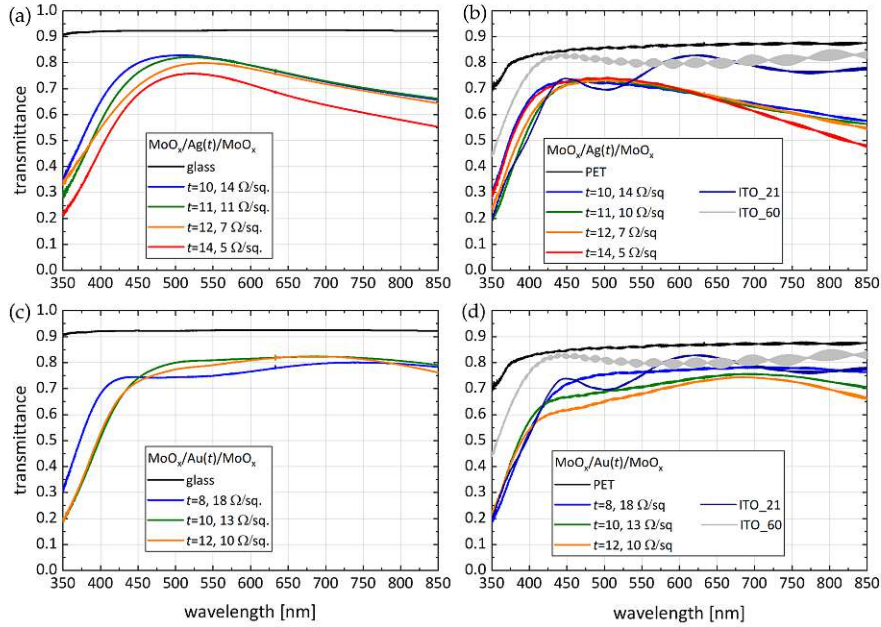


**Figure 2.7:** Average visible transmittance (in solid black squares) and figure of merit (in open blue squares) versus metal thickness for (a) electrodes with Ag on glass, (b) electrodes with Ag on PET, (c) electrodes with Au on glass, and (d) electrodes with Au on PET. (b) and (d) also include dashed blue lines showing the figure of merit for the two commercial PET/ITO electrodes (ITO\_60 and ITO\_21).

with increasing Ag thickness, as expected. Likewise, Figures 2.7 (c) and (d) show the spectra and sheet resistance values for the  $D_1(40 \text{ nm})/\text{Au}(t)/D_3(40 \text{ nm})$  electrodes, with  $t=8,10,12 \text{ nm}$  on glass and PET, respectively. Sheet resistance values range from  $18\text{-}10 \Omega/\text{sq}$ , again decreasing with increasing Au thickness.

Figures 2.7 (b) and (d) show spectra for two reference commercial ITO electrodes on PET, one with  $60 \Omega/\text{sq}$  (denoted as ITO\_60) and the other with  $21 \Omega/\text{sq}$  (denoted as ITO\_21) sheet resistance, for comparison. From the number of the interference fringes of the transmittance spectra it is clear that the ITO film with the lower sheet resistance is considerably thicker.

The average optical transmittance in the visible range  $400\text{-}700 \text{ nm}$ ,  $T_{av}$ , is calculated from the optical spectra and summarized in Figure 2.8, together with the Haacke figure of merit,  $\Phi = T_{av}^{10}/R_s$  [49]. The electrodes on glass with Ag(12) have lower figure of merit ( $\Phi = 0.0081 \Omega^{-1}$ ) than the highest performing evaporated electrodes in the literature with  $T_{av} = 0.78$ ,  $R_s = 7.22 \Omega/\text{sq}$  and  $\Phi = 0.0115 \Omega^{-1}$  [50]. On the other hand, the electrodes on PET with Ag(12), Ag(14) and Au(8) have higher  $\Phi$  value than both reference ITO electrodes (ITO\_60 and ITO\_21). These electrodes have also a higher  $\Phi$  value ( $0.0040, 0.0057$  and  $0.0021 \Omega^{-1}$ , respectively) than the best reported  $\text{MoO}_x/\text{Ag}/\text{MoO}_x$  evaporated electrodes on PET [28] with a  $\Phi = 0.0029 \Omega^{-1}$  ( $T_{av} = 0.72$  and  $R_s = 13 \Omega/\text{sq}$ ). It is therefore demonstrated that the sputtered DMD electrodes not only are deposited

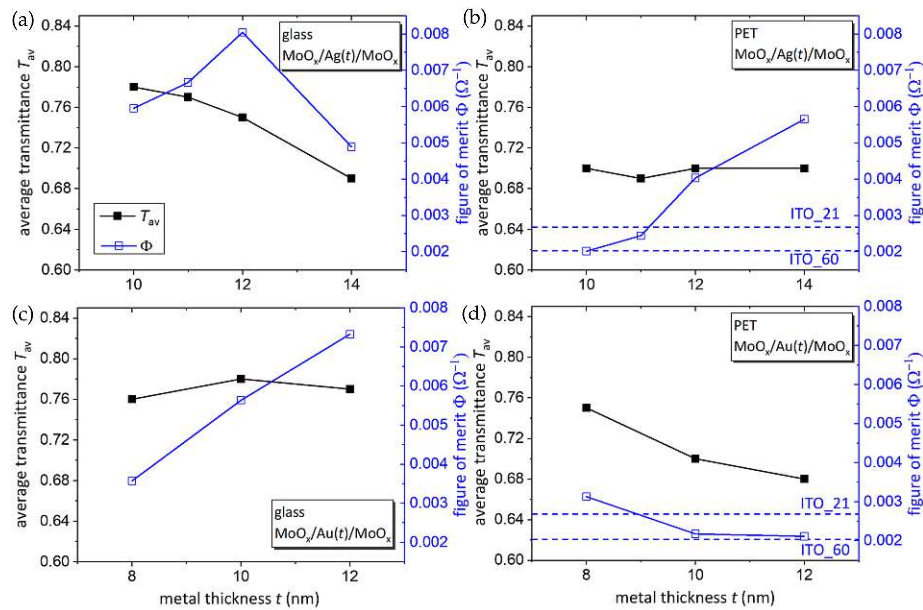


**Figure 2.8:** Average visible transmittance (in solid black squares) and figure of merit (in open blue squares) versus metal thickness for (a) electrodes with Ag on glass, (b) electrodes with Ag on PET, (c) electrodes with Au on glass, and (d) electrodes with Au on PET. (b) and (d) also include dashed blue lines showing the figure of merit for the two commercial PET/ITO electrodes (ITO\_60 and ITO\_21).

faster than the evaporated ones, but also show better performance, represented by the higher figure of merit.

### 2.2.2 Surface morphology, electronic structure and composition

$5 \times 5 \mu\text{m}^2$  AFM images of the  $\text{MoO}_x/\text{Ag}/\text{MoO}_x$  electrodes on glass and PET are presented in Figure 2.9. The electrodes on glass show low root mean square (RMS) roughness of  $2.0 \pm 0.2 \text{ nm}$  (2.9 (b)). For comparison, the bare glass substrate has an RMS roughness of  $1.5 \pm 0.1 \text{ nm}$  (2.9 (a)). The surface roughness is much larger for the electrode on PET, reaching an RMS value of  $20.4 \pm 1.5 \text{ nm}$  (2.9 (d)), with  $14.5 \pm 1.0 \text{ nm}$  the background roughness of the bare PET substrate (2.9 (c)). This shows that the electrode roughness is mostly determined by the background roughness of the substrate.

The XPS measurements of  $\text{MoO}_x/\text{metal}/\text{MoO}_x$  electrodes on glass and PET are shown in Figure 2.10. The position of the Mo  $3d$  peaks in Figure 2.10 (a) indicate that mainly stoichiometric  $\text{MoO}_3$ , i.e. oxidation state  $\text{Mo}^{6+}$ , is found on the surface. Figure 2.10 (c) focuses on the Ag  $3d$  region, where a significant amount of Ag (Ag/Mo ratio of 2.7 at.%) is found on the electrode's surface when PET is used as substrate. Interestingly, for the same electrode on glass, much less Ag (Ag/Mo ratio of 0.5 at.%) is detected on the surface while the DMD electrodes with Au show only molybdenum and oxygen on the surface (Figure 2.10 (d)). This observation is attributed to the generally high migration

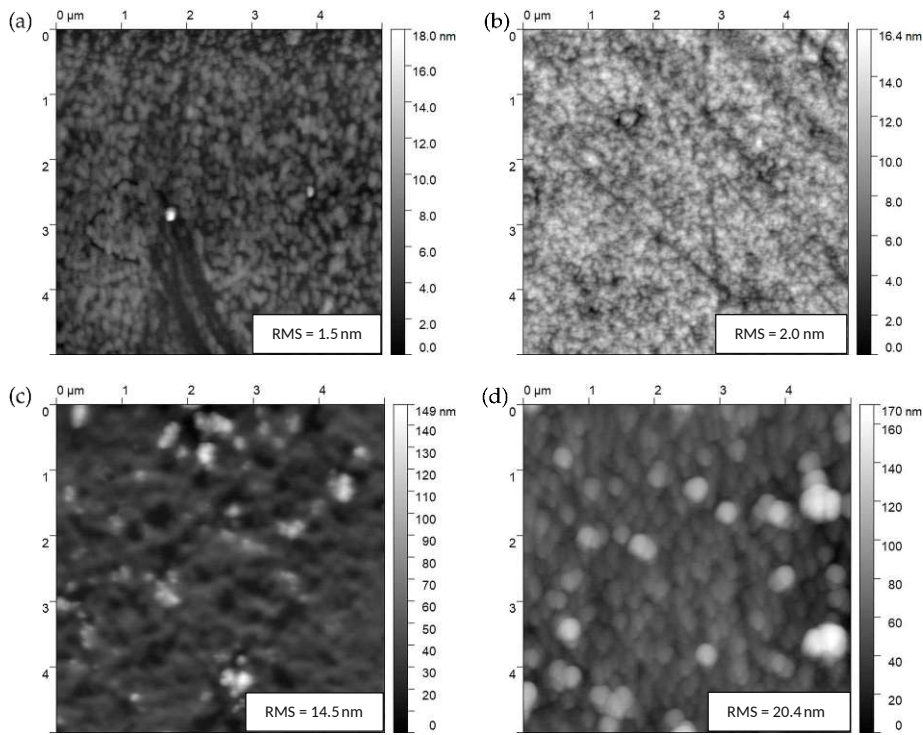


**Figure 2.9:** AFM images of (a) bare glass, (b) MoO<sub>3</sub>/Ag/MoO<sub>3</sub> electrodes on glass, (c) bare PET, and (d) MoO<sub>3</sub>/Ag/MoO<sub>3</sub> electrodes on PET.

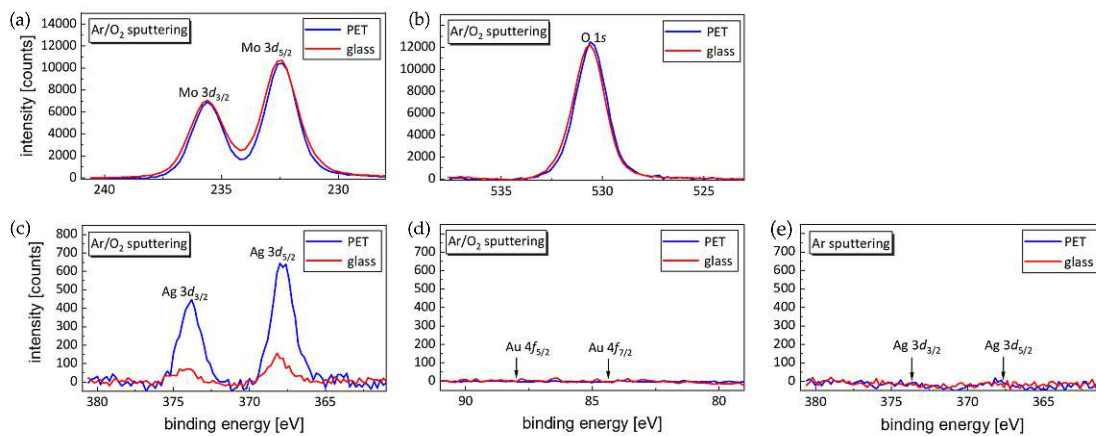


**Figure 2.10:** XPS spectra of (a) Mo 3*d*, (b) O 1*s*, (c) Ag 3*d*, (d) Au 4*f* peaks of MoO<sub>3</sub>/metal/MoO<sub>3</sub> electrodes on glass and PET as described in 2.2. (e) XPS spectrum in the Ag 3*d* region, where the whole top MoO<sub>x</sub> layer is sputtered non-reactively.



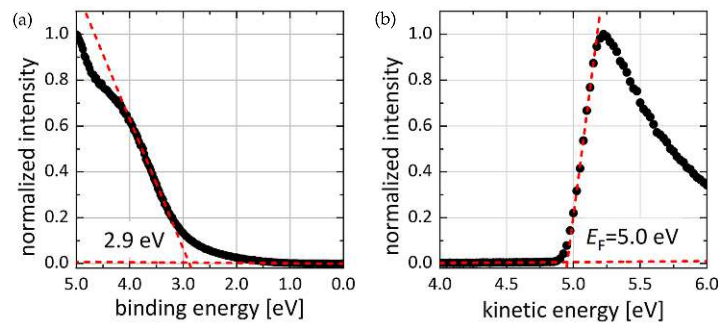


**Figure 2.11:** UPS measurements of  $\text{MoO}_x/\text{metal}/\text{MoO}_x$  electrodes in (a) the valence band (VB) and the (b) secondary electron cut-off (SECO) region.

potential of Ag, also reported by others [51]. As the Ag migration predominantly takes place at the grain boundaries, the effect is more pronounced for electrodes on PET due to the increased surface roughness compared to glass. More specifically, Ag ions are generated through photoexcitation or energy transfer during sputtering and are then drawn towards the surface by negatively charged oxygen species from the reactive plasma during the deposition of the top  $\text{MoO}_3$  layer. Indeed, when the whole top  $\text{MoO}_x$  layer is sputtered non-reactively, there is no Ag detected on the electrode's surface, irrespective of the substrate (Figure 2.10 (e)). However, humidity can also cause electrochemical reactions within the grain boundaries that produce Ag ions which then diffuse to the surface [52]. So, when exposing the electrodes to ambient conditions, the Ag migration is fostered and Ag can be found on the surface of all aged electrodes.

Figure 2.11 shows the UPS measurements of the  $\text{MoO}_x/\text{metal}/\text{MoO}_x$  electrodes. It is noted at this point, that there is no difference in the results whether Ag or Au is used as metal layer. The valence band maximum is found 2.9 eV below the Fermi level (at 0 eV in binding energy scale). From the secondary electron cut-off (SECO), displayed in kinetic energy scale, the work function can be directly extracted, yielding 5.0 eV. These values agree with what has been reported in the literature for  $\text{MoO}_x$  films (with  $x \sim 3$ ) which were exposed to ambient air before the measurement [53, 54]. This is important to note, as literature values for the work function of  $\text{MoO}_x$  range from below 5 eV to almost 7 eV depending on the water adsorption and hydroxylation on the surface as well as film stoichiometry and crystallisation [42, 41].

### 2.2.3 Mechanical, thermal and chemical stability

The mechanical stability of the DMD electrodes upon tensile stress is tested using a motorized tension/compression test stand at a speed of 1 m/min. The sample is contacted with Ag paste and Cu adhesive tape and the electrical resistance of the electrode was

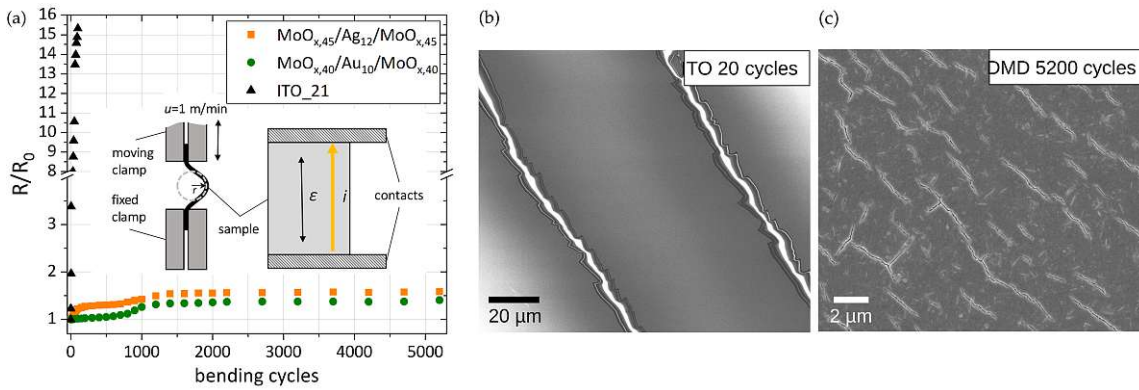


**Figure 2.12:** (a) Evolution of the relative resistance of  $\text{MoO}_x/\text{metal}/\text{MoO}_x$  electrodes on PET as a function of bending cycles under tensile stress in comparison to commercial PET/ITO. (b) SEM image of the ITO layer after 20 bending cycles and (c) SEM image of the DMD electrode ( $\text{MoO}_x/\text{Ag}/\text{MoO}_x$ ) after 5200 cycles.

measured along the strain direction from one edge to the opposite edge of the sample in the relaxed (unstrained) state (see in the inset of Figure 2.12 (a)). A bending radius of  $r = 5$  mm is applied, yielding a strain of  $\epsilon = d/(2r)$ , where  $d$  is the substrate thickness [55]. For the 175  $\mu\text{m}$  thick PET substrate, this gives a strain of  $\epsilon = 1.75\%$ . Figure 2.12 (a) shows the relative increase in resistance of the DMD electrodes in comparison to a commercial PET/ITO electrode. While the ITO undergoes catastrophic failure after a few bending cycles, the relative resistance of the DMD electrodes increases only to  $\sim 1.5$  times the initial value after more than 5000 bending cycles. The high mechanical stability of the DMD electrodes is attributed to the ductility of the metal layer which maintains the conductivity even when the dielectric layer develops cracks. Moreover, the cracks in the  $\text{MoO}_3$  layer (Figure 2.12 (c)) are restricted in length, being in the range of 2 to 10  $\mu\text{m}$ . In contrast to that, the ITO layer develops large cracks across the whole sample (Figure 2.12 (b)), which soon impede the current flow.

The thermal stability of glass/ $\text{MoO}_3$ /metal/ $\text{MoO}_3$  electrodes was tested by annealing experiments on a hotplate in ambient air as well as inside an  $\text{N}_2$ -filled glovebox. Using Ag as metal layer, a different piece from the DMD stack is used for each annealing temperature, ranging from 150 to 300  $^\circ\text{C}$ . Each sample was ramped from room temperature to the target temperature, where it remained for 30 min and then ramped back down to room temperature. Figure 2.13 displays the evolution of the average visible transmittance and the sheet resistance as a function of the annealing temperature for both cases. Annealing in air leads to an increase of average transmittance until 250  $^\circ\text{C}$ , followed by a significant drop at 300  $^\circ\text{C}$ . At 250  $^\circ\text{C}$ , the sheet resistance increases from 6 to 11  $\Omega/\text{sq}$  and reaches up to 200  $\Omega/\text{sq}$  at 300  $^\circ\text{C}$ . These changes indicate firstly the removal of oxygen vacancies by oxidation of the  $\text{MoO}_x$  layer until the Ag layer begins to oxidize at temperatures above 250  $^\circ\text{C}$ , which reduces the electrodes transparency and conductivity. In  $\text{N}_2$  atmosphere on

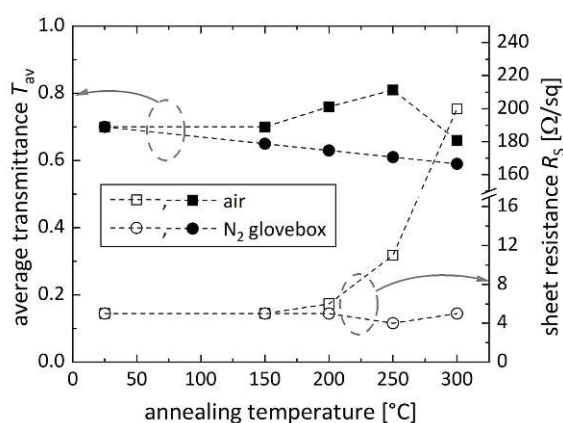


**Figure 2.13:** Average visible transmittance and sheet resistance of glass/MoO<sub>40</sub>/Ag<sub>14</sub>/MoO<sub>10/30</sub> electrodes as a function of annealing temperature after 30 min on a hotplate in ambient and N<sub>2</sub> (glove box) conditions.

the other hand, a gradual decrease of the average transmittance is observed, while the sheet resistance practically remains constant. In this case, the oxidation of Ag is prevented but leads to reduced transparency due to the reduction of the MoO<sub>x</sub>.

Finally, the chemical stability against common solvents used in perovskite and organic solar cells and LEDs was tested. The DMD electrodes do not show any signs of electrical or optical degradation after spin coating with DMF (dimethylformamide), DMSO (dimethyl sulfoxide), chlorobenzene, chloroform and toluene (in the form of toluene-based PEDOT:PSS formulation Clevis HTL Solar). However, it was observed that spin-coating of water-based PEDOT:PSS (Clevis PH1000) leads to complete dissolution of the DMD electrodes. In fact, it is found that any contact with water leads to an immediate dissolution of the sputtered MoO<sub>3</sub>. This effect is discussed in detail in Chapter 4.

### 2.3 SUMMARY

The chapter reported the properties of sputtered MoO<sub>x</sub> ( $x \leq 3$ ) thin films. High sputter rates, up to 90 nm/min, could be achieved for a sub-oxidic MoO<sub>2.7</sub> target under DC magnetron sputter conditions. Transparent MoO<sub>x</sub> layers are obtained when reactive sputtering (with 6.6% O<sub>2</sub>) is used. In the case of non-reactive sputtering, the layers have increased optical absorption in the whole visible wavelength regime. The indirect band gap of the amorphous MoO<sub>x</sub> layers is  $\sim 2.9$  eV. Transparent electrodes are designed in the form of MoO<sub>x</sub>/(Ag or Au)/MoO<sub>x</sub> stacks, yielding high optical transmittance and low sheet resistance. To avoid the oxidation of Ag during the deposition, a protective MoO<sub>x</sub> slayer, sputtered without oxygen, was introduced. On PET, the electrodes achieve a higher figure-of-merit than similar evaporated electrodes or commercial PET/ITO electrodes. In addition, they have a dramatically higher stability upon bending, compared to ITO.

From XPS/UPS measurements a work function of 5 eV is extracted for the air-exposed  $\text{MoO}_x$ -based electrodes. Interestingly, Ag is found to diffuse to the electrode surface, especially in the case of electrodes on PET, when  $\text{MoO}_x$  is deposited by reactive sputtering. The diffusion of Ag is driven by negatively charged oxygen species and enhanced by the roughness of the PET substrate.

---

## MOLYBDENUM TITANIUM OXIDE – MTO

---

*The majority of the results presented in this chapter have been published in:*

*Goetz, S. et al. Transparent electrodes based on molybdenum–titanium–oxide with increased water stability for use as hole-transport/hole-injection components. Journal of Materials Science 57, 8752–8766 (2022). [56], reproduced under the corresponding copyright agreement (8.2).*

Due to the high work function ( $> 5$  eV),  $\text{MoO}_3$  is widely used as hole-extraction/ hole-injection layer between the photon absorber/ emitter layer and the electrode, thus enhancing the device efficiencies of solar cells and OLEDs [14, 40, 57, 58, 59]. In the previous chapter,  $\text{MoO}_3$  is employed in dielectric/metal/dielectric (DMD) structures which could simultaneously serve as hole-transport/hole-injection layer and transparent electrode.

However, it was observed that poorly textured or amorphous  $\text{MoO}_3$  layers are extremely instable when exposed to ambient humidity and liquid water. Moreover, water exposure has strong influence on important material properties, such as the electron energy levels [60, 61, 62], due to surface hydration or hydroxylation. Over long exposure periods, humid air leads to the gradual degradation of thin  $\text{MoO}_3$  layers. Further, the contact with liquid water leads to the complete and rapid dissolution of the amorphous  $\text{MoO}_3$  layer, making processing with water-based solutions impossible (2.2.3). One possibility to stabilize the  $\text{MoO}_3$  in water is by crystallisation of the layers, since crystalline layers are less prone to hydrolysis and subsequent dissolution [63, 64, 65]. However, crystalline layers are mostly achieved by annealing at high temperatures ( $300^\circ\text{C}$  and higher), which is not compatible with flexible substrates like polyethylene terephthalate (PET). These substrates are widely used in industrial manufacturing (also for roll-to-roll production) and low-cost flexible devices, but are instable at temperatures higher than  $\sim 120^\circ\text{C}$ .

In the current chapter the aim is to increase the water stability of sputtered, amorphous  $\text{MoO}_3$  layers without applying high temperatures, but by alloying with another refractory metal oxide to reduce hydrolysis and dissolution, while maintaining the essential electronic properties (i.e. wide band gap and high work function) of  $\text{MoO}_3$ . To this end, titanium oxide is introduced to form a mixed molybdenum-titanium-oxide compound material (MTO).  $\text{TiO}_2$  is known to be stable in water and in a wide pH range of aqueous solutions [66]. Additionally,  $\text{TiO}_2$  is also composed of octahedral  $\text{TiO}_6$  building blocks,

analogous to the building blocks of  $\text{MoO}_3$  [40], which gives both oxides a d-band dominated electronic band structure [12].

So far, composites of molybdenum and titanium oxide are reported in the form of crystalline nanomaterials, for different applications. In the field of water electrolysis, Kim et al. [67] reported on oxide composites as support for Ir catalyst for the oxygen evolution reaction, using varying Mo content (0-36 at% Mo) to enhance the electrical conductivity of  $\text{TiO}_2$ . Similarly, Chen et al. [68] studied Mo-doped  $\text{TiO}_2$  nanoparticles to support Pt catalysts for the hydrogen evolution reaction and improve the performance, as well as the durability of the catalyst. In both studies, the added Mo yields stronger interaction with the metal catalyst and, thus, reduces corrosion.  $\text{TiO}_2$ - $\text{MoO}_3$  composites have been also investigated in the field of photoactive components and photovoltaic devices. Khan et al. [69] presented  $\text{TiO}_2$ - $\text{MoO}_3$  nanocomposites (with max. 9%  $\text{MoO}_3$ ) prepared by laser ablation in water to adapt the properties of  $\text{TiO}_2$  for more efficient photodegradation processes for photocatalysis and for photovoltaic devices, through the lowering of the band gap and the reduction of carrier recombination. Khlyustova et al. [70] also reported on  $\text{MoO}_x$ -decorated  $\text{TiO}_x$  and  $\text{TiO}_x$ -decorated  $\text{MoO}_x$  materials synthesized by underwater plasma discharges and their beneficial influence on the photocurrent when used as electron transport layers in dye-sensitized solar cells. Liu et al. [71] elaborated on the photocatalytic activity of the composite heterostructures, synthesized from precursor suspensions, while Li et al. [72] observed promising photochromic properties of hydrothermally-synthesized  $\text{TiO}_2$ - $\text{MoO}_3$  core-shell nanomaterials.

In contrast to the aforementioned reports, the present work introduces for the first time compact, amorphous thin layers, deposited by sputtering from a mixed molybdenum-titanium-oxide compound target. The sub-oxidic composition of the sputter target allows fast deposition in direct current (DC) magnetron mode, achieving high sputtering rates that are relevant for industrial applications. The sputtered MTO layers are investigated in terms of their optical and electronic properties and, most interestingly, show significantly increased water stability as compared to amorphous  $\text{MoO}_3$  layers, while maintaining the favourable energy band characteristics of  $\text{MoO}_3$ . This enables the exploitation of MTO as hole-transport/hole-injection layer, especially in devices where processing with water-based solutions is required. Furthermore, the paper introduces the use of MTO layers for the design and realization of transparent dielectric/metal/dielectric (DMD) electrodes on glass and PET substrates.

### 3.1 CHARACTERIZATION OF MTO THIN FILMS

#### 3.1.1 DC magnetron sputtering of MTO

The sputter target (10.16 cm in diameter) was made by mixing  $\text{MoO}_2$  and  $\text{TiO}_2$  powders with a Mo:Ti ratio of 1:1 and a resulting oxygen content of 71 at.%. Similarly to  $\text{MoO}_x$  before, the target is designed with sufficiently high electrical conductivity to allow sputtering in DC mode. This generally permits higher deposition rates as compared to typical RF sputtering from oxide targets. Again a sputter power of 164 W (corresponding to a power density of  $2 \text{ W/cm}^2$ ) is chosen, yielding significant deposition rates without compromising the durability of the target due to excessive heating. More efficient target cooling would, however, allow for higher power densities yielding even higher deposition rates.

Analogously to  $\text{MoO}_3$ , highest deposition rates (20 nm/min) are achieved without adding oxygen to the process gas, yielding, however, optically absorbing films with dark grey appearance (see Figure 3.1 (a)). Adding oxygen to the sputter process results in transparent layers but leads to a reduction of the deposition rate with increasing  $\text{O}_2$  content. The minimal amount of oxygen that can be realised with the given sputtering system (6.6%  $\text{O}_2$ ) is sufficient to achieve highly transparent layers and still yields a deposition rate of 17 nm/min. Further addition of oxygen does not increase the transmittance of 50 nm thick layers but reduces the deposition rate significantly (not shown).

Figure 3.2 (a) shows the transmittance and reflectance spectra of reactively and non-reactively sputtered 50 nm thick MTO films. While the reactively sputtered film has high transmittance over the whole visible range, the non-reactively sample shows drastically increased absorption due to the lack of oxygen. Interestingly, it is found that reducing the sputtering power (to 21 W) leads to higher transmittance even without addition of

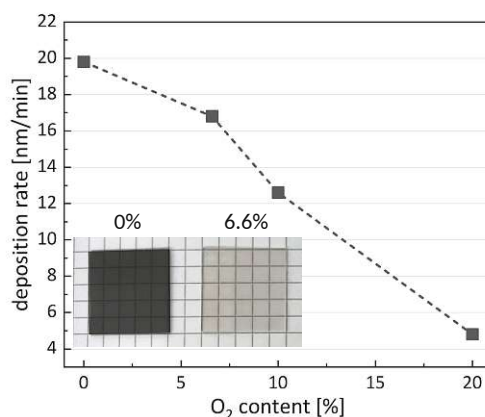


**Figure 3.1:** Sputter deposition rates as a function of oxygen content. The inset shows a photograph of 50 nm thick films sputtered with 0 and 6.6%  $\text{O}_2$ .

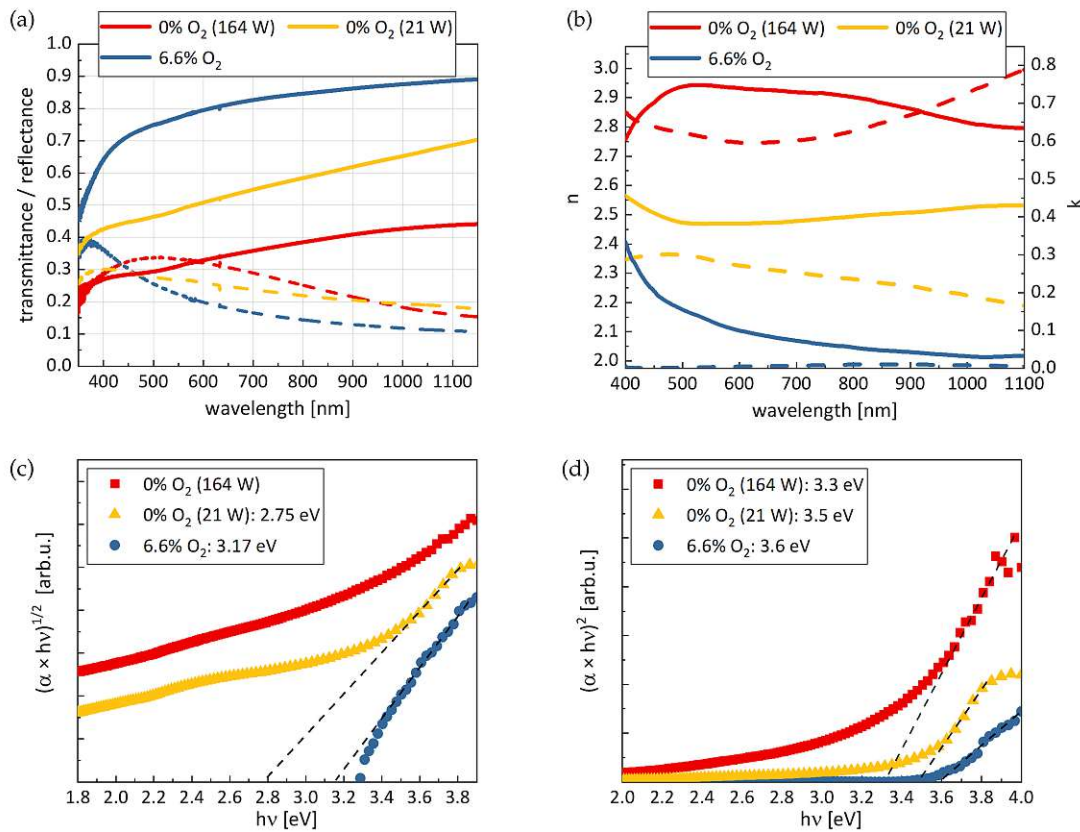


**Figure 3.2:** (a) Transmittance (solid lines) and reflectance (dashed lines) spectra of 40 nm thick MTO films sputtered on glass with different oxygen partial pressures and different sputtering power, (b) corresponding refractive indices (real part  $n$  presented as solid lines and imaginary part  $k$  presented as dashed lines) calculated from the transmittance and reflectance spectra, (c),(d) Tauc plots of indirect and direct transitions, respectively.

oxygen to the process gas which suggests a higher oxygen content in the film. These characteristics are also reflected in the refractive index (shown in Figure 3.2 (b)) which is calculated from the optical spectra using a TMM algorithm 8.1.3. While the film sputtered without oxygen at high power yields a strongly increased extinction coefficient,  $k$ , over the whole visible range, it is reduced for non-reactively sputtered films at low power until it vanishes for the reactively sputtered layer. The real part of the refractive index of the 6.6% O<sub>2</sub> sample lies just within the reported literature values for MoO<sub>3</sub> and TiO<sub>2</sub> thin films [73, 74, 75, 76].

Similarly, the extracted optical band gap (Figure 3.2 (c)) for the reactively sputtered films yields 3.2 eV which is in between the literature values for amorphous MoO<sub>3</sub> and TiO<sub>2</sub> [34, 77], assuming indirect transitions. However, also a direct optical transition is observed at 3.6 eV, i.e. 0.4 eV above the fundamental absorption edge (Figure 3.2 (d)). For reduced oxygen content, as in the 0% O<sub>2</sub> sample sputtered at low power, the indirect band gap value decreases to 2.8 eV. For the 0% O<sub>2</sub> film sputtered at 164 W the absorption coefficient



$\alpha$  does not show a clear absorption edge making it impossible to extract the band gap from the Tauc plot. The lack of oxygen leads to a partial occupation of the Mo  $4d$  states, giving rise to delocalised electrons and, thus, enhancing metallic absorption. This can even result in the disappearance of the band gap, as reported for  $\text{MoO}_2$  [38, 78]. However, direct transitions are observed for both non-reactively sputtered samples at 3.5 eV (21 W) and 3.3 eV (164 W), respectively.

Furthermore, the electrical resistivity is obtained from linear current-voltage curves after sputtering Au contacts onto 100 nm thick MTO films for an in-line 4-wire resistivity set-up. The 0%  $\text{O}_2$  film (sputtered at 164 W) yielded a resistivity of  $0.7 \Omega\cdot\text{cm}$ , while the transparent, reactively sputtered sample was found completely insulating, with resistances in the  $\text{G}\Omega$ -range.

### 3.1.2 Crystal structure and annealing effects

*The following section presents additional data which has not been published elsewhere.*

According to XRD measurements, the sputtered layers are amorphous without additional heat treatment (see Figure 3.3 (a)). Irrespective of the oxygen content or the layer thickness, there are no peaks in the diffractogram other than the background from the glass substrate. To investigate the compositional distribution of the mixed Mo-Ti oxide, EDX elemental mapping is performed for a 300 nm thick, reactively sputtered MTO film. The result is shown in 3.3 (b), where a homogeneous distribution of Mo and Ti is observed even under high magnification, which leads to the assumption of a nanocomposite material with a strong mixture of  $\text{MoO}_x$  and  $\text{TiO}_x$  phases.

The onset of crystallisation starts at temperatures around  $400^\circ\text{C}$ . 100 nm thick samples are heated on a hotplate in air for 1 and 2 hours, respectively, and the resulting XRD patterns are shown in Figure 3.4 (a). The inset shows SEM images, where only a partial

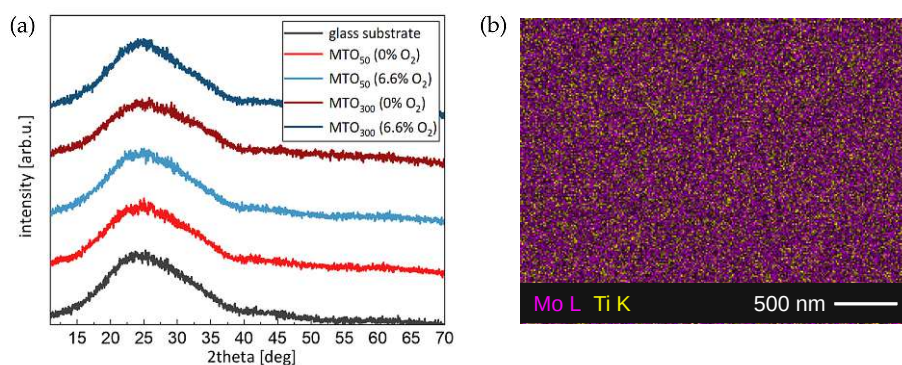


**Figure 3.3:** (a) XRD characterization of 50 nm thick MTO layers on glass substrates, (b) EDX elemental mapping of a 300 nm thick 6.6%  $\text{O}_2$  MTO film with Mo in purple and Ti in yellow.

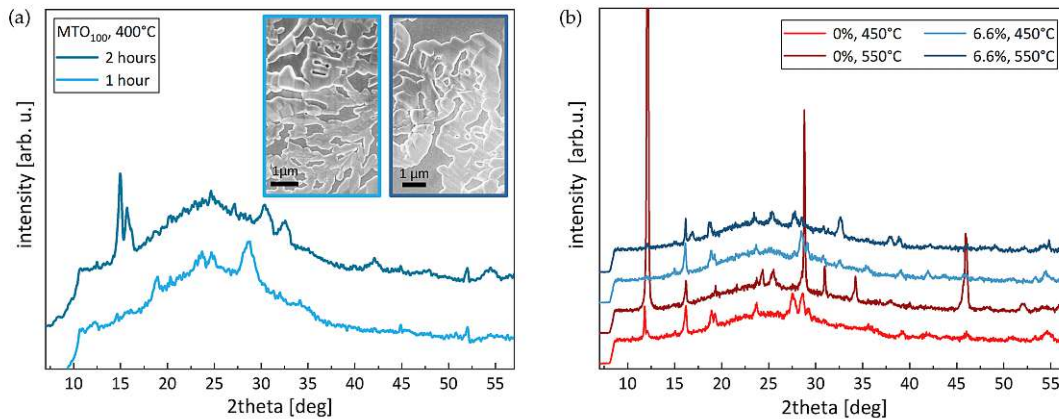


**Figure 3.4:** (a) XRD pattern of 100 nm thick MTO (6.6% O<sub>2</sub>) annealed at 400°C for 1 and 2 hours, the inset shows the respective SEM images (b) XRD graphs of 300 nm thick MTO (0 and 6.6% O<sub>2</sub>) annealed at 450°C and 550°C.

crystallisation of the film is observed. However, the increased annealing time resulted in very different reflection patterns and both are difficult to assign to a distinct MoO<sub>x</sub> or TiO<sub>x</sub> phase. To promote more complete and thorough crystallisation, further annealing was performed with 300 nm thick MTO films (0 and 6.6% O<sub>2</sub>) in a muffle furnace at temperatures of 450°C and 550°C for 4 hours. Although the reflections become more pronounced under these conditions (see Figure 3.4 (b)), it is still not possible to explicitly assign a corresponding MoO<sub>x</sub> or TiO<sub>x</sub> crystal phase. The occurrence and the position of the peaks vary with different annealing temperature and oxygen content in the film.

Complementary SEM/EDX measurements (Figure 3.5) show that the crystallisation is still inhomogeneous with crystallites protruding from an amorphous, sometimes porous background. The elemental mapping gives rise to a phase separation, where a higher amount of Mo is found in the region of the crystallites. Interestingly, also an increased amount of Na is detected in these regions, while Ti is still homogeneously or even inversely distributed. Following the EDX elemental mapping, it is assumed that Na diffuses from the glass substrate to the MTO film and forms a Sodium Molybdenum Oxide, as described for pure MoO<sub>x</sub> in 2.1.2. Again, the Na<sub>6</sub>(Mo<sub>10</sub>O<sub>33</sub>) phase agrees best with the measured reflections. However, the variations in the peak positions and intensity distribution may be a sign of texture, i.e. preferred orientations, or of the presence of a second phase, e.g. one with less Na or even orthorhombic MoO<sub>3</sub>. This can also be seen in Figure 3.5 for the 6.6%, 550°C sample, where two different crystals are observed: elongated, rectangular crystals (further on the top of the image) mainly consisting of Mo and more undefined, wavy structures with increased Na content.

In any case, the crystallinity and crystal orientation sensitively depends on both, the initial sample properties as well as on the annealing conditions, giving rise to diverse

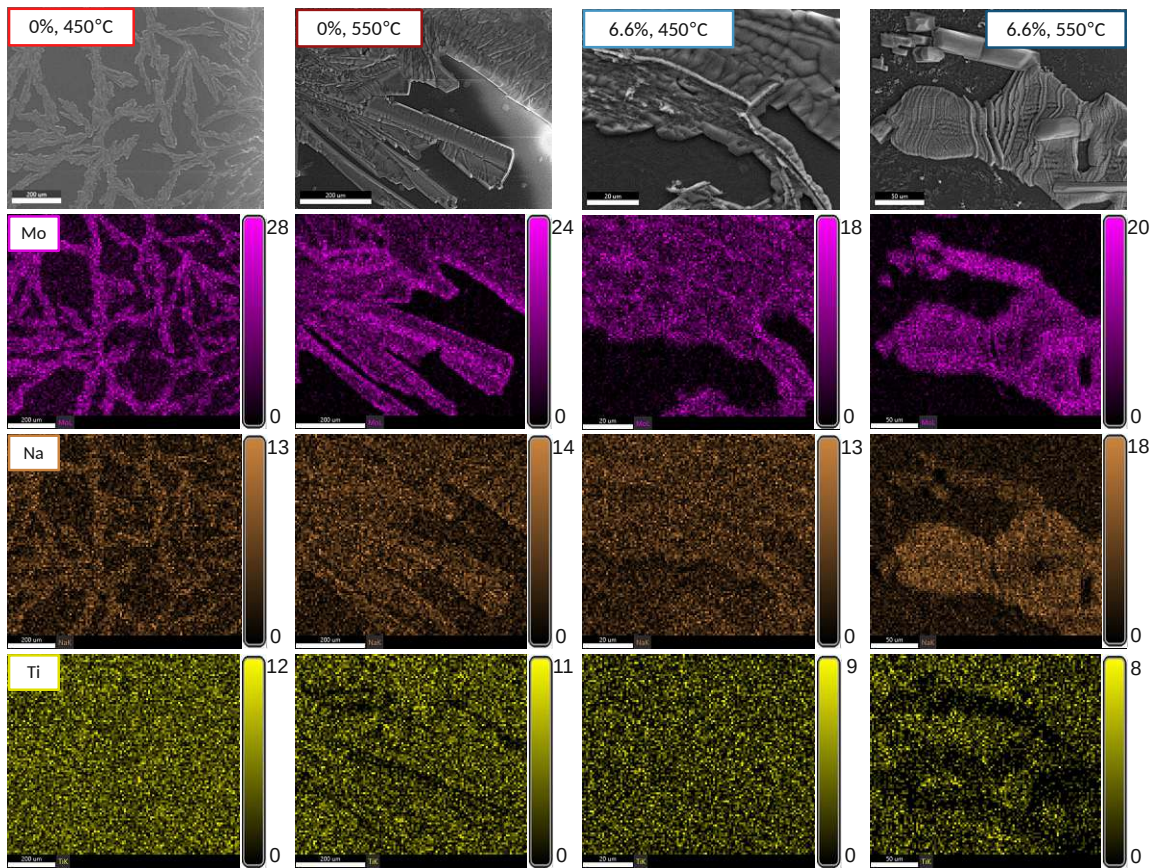


**Figure 3.5:** EDX elemental mapping for 300 nm thick MTO films with different initial oxygen content, annealed at 450°C and 550°C. The colour scale bars indicate the weight percent.

XRD patterns. Another variable contributing to the ambiguities in assigning reference patterns may originate from the presence of Ti atoms possibly leading to lattice distortions.

## 3.2 TRANSPARENT ELECTRODES BASED ON MTO

### 3.2.1 DMD electrode architecture

For transparent electrodes in a MTO/metal/MTO architecture, Ag is the preferred choice as metal layer, having the lowest optical losses in the visible regime. However, as described for the  $\text{MoO}_x$ -based electrodes (2.2), the thin Ag layer is oxidized when sputtering the top MTO layer with oxygen in the process gas. Therefore, an additional protective layer of MTO (sputtered without oxygen) is introduced on top of Ag (see Figure 3.6 (a)). To reduce optical losses, the protective layer MTO-2 is sputtered at low power (21 W), which was shown to yield more transparent layers (3.1).

The optimal thicknesses of the top and bottom MTO layers (MTO-3, MTO-1) are determined by TMM calculations (8.1.3) fixing 14 nm for the Ag layer and 10 nm for the

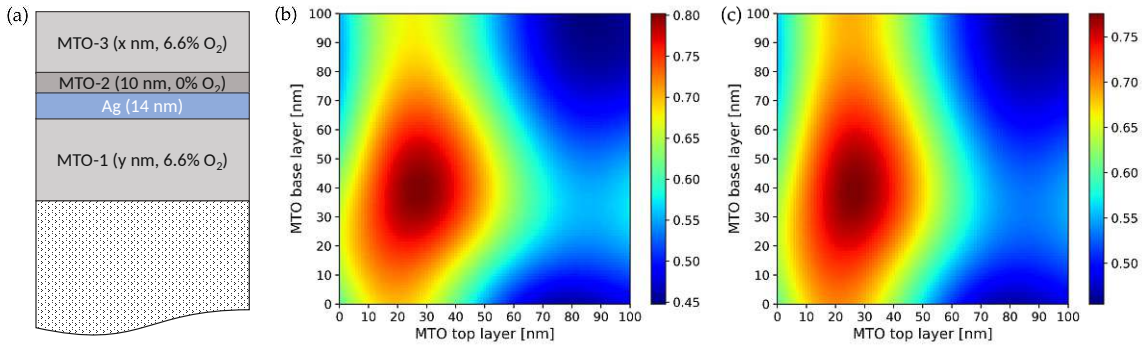


**Figure 3.6:** (a) Schematic representation of the DMD electrode design with Ag as metal layer, where y is the thickness of the base and x the thickness of the top MTO layer. (b),(c) TMM simulation results of the presented structure on glass and PET, respectively.

MTO-2 interlayer. The result is shown in Figure 3.6 (b) and (c) for glass and PET substrate, respectively. In both cases, there is a broad window (in dark red) that maximizes the average transmittance  $T_{av}$  (between 400-700 nm). On glass the simulated maximum is  $T_{av} = 0.8$  for a 39 nm thick bottom layer (MTO-1) and a 27 nm thick top layer (MTO-3) and on PET the maximal value  $T_{av}$  was found at 0.77 for the same thicknesses.

The experiment shows the highest average visible transmittance for MTO<sub>40</sub>/Ag<sub>14</sub>/MTO<sub>10/30</sub> (Figure 3.7), where the subscripts denote the layer thickness in nm and the top layer is

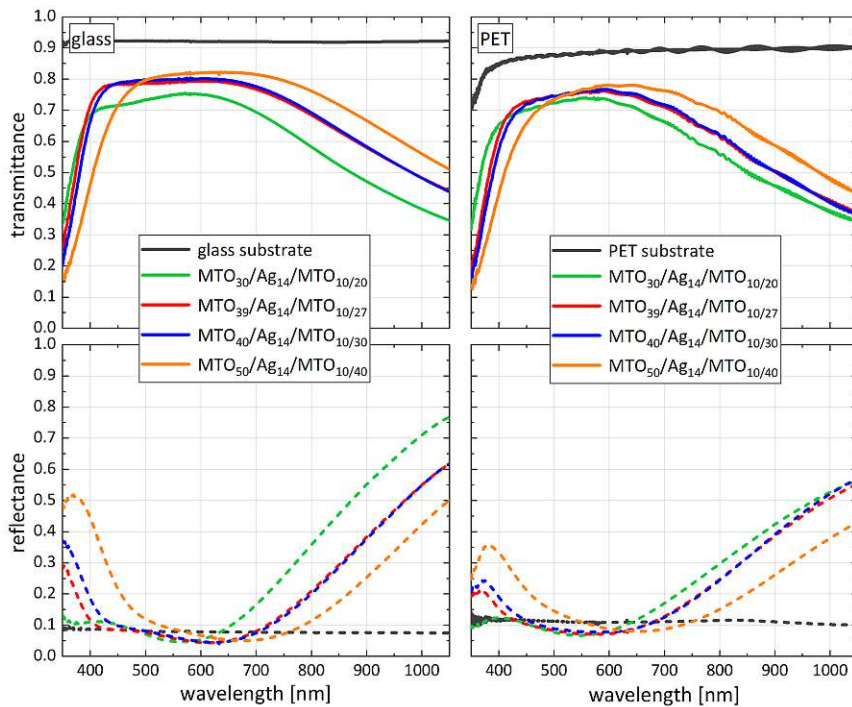


**Figure 3.7:** Transmittance (solid lines) and reflectance (dashed lines) spectra of MTO/Ag/MTO electrodes with varying dielectric thicknesses on glass (left) and PET (right).

deposited according to the recipe described above, including 10 nm of the protective, non-reactively sputtered MTO-2 layer. This electrode yields  $T_{av} = 0.79$  on glass and  $T_{av} = 0.73$  on PET. The sheet resistance  $R_s$  is mainly determined by the Ag layer and is found to be  $R_s = 5.7 \pm 0.2 \Omega/\text{sq}$  on glass and  $R_s = 4.7 \pm 0.1 \Omega/\text{sq}$  on PET. Using Haacke's figure of merit [49] for transparent electrodes  $\Phi = T_{av}^{10}/R_s$ , this electrode yields  $\Phi = 0.017 \Omega^{-1}$  on glass and  $\Phi = 0.009 \Omega^{-1}$  on PET. For comparison, commercially available ITO electrodes on glass and PET yield values below  $\Phi = 0.019 \Omega^{-1}$  and  $\Phi = 0.003 \Omega^{-1}$ , respectively. Furthermore, it is demonstrated how the wavelength window for high transmittance (and minimal reflectance due to destructive interference) can be tuned to specific applications and device requirements by varying the dielectric thickness.

The electrodes are also tested with Au as metal layer using the same MTO thickness of 40 nm. However, no interlayer is needed in this configuration as Au does not oxidize, hence the whole top MTO layer can be sputtered reactively. For the same reason, the Au thickness is reduced to 10 nm lowering optical losses. The resulting transmittance and reflectance spectra of the electrode on glass and PET are shown in Figure 3.8 (b). One can see a reduction of the transmittance around 500 nm, where Au has its characteristic d-band absorptions [79], leading to an average visible transmittance of  $T_{av} = 0.74$  on glass and  $T_{av} = 0.71$  on PET. With sheet resistance of  $R_s = 12.5 \pm 1.0 \Omega/\text{sq}$  on both, glass and PET, the Haacke figure of merit yields  $\Phi = 0.004 \Omega^{-1}$  on glass and  $\Phi = 0.003 \Omega^{-1}$  on PET.

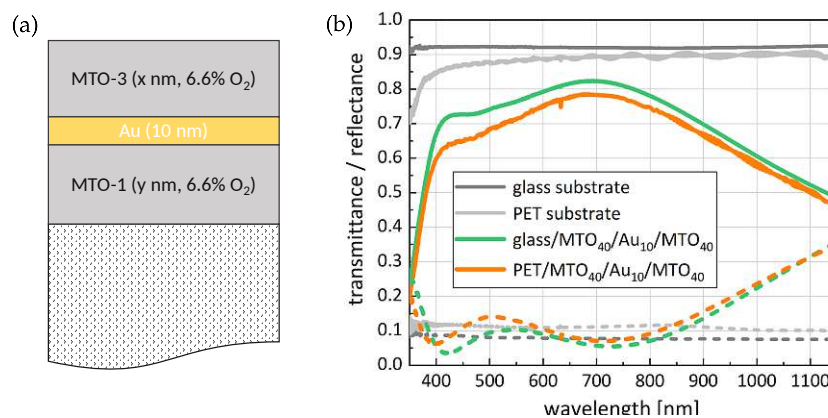
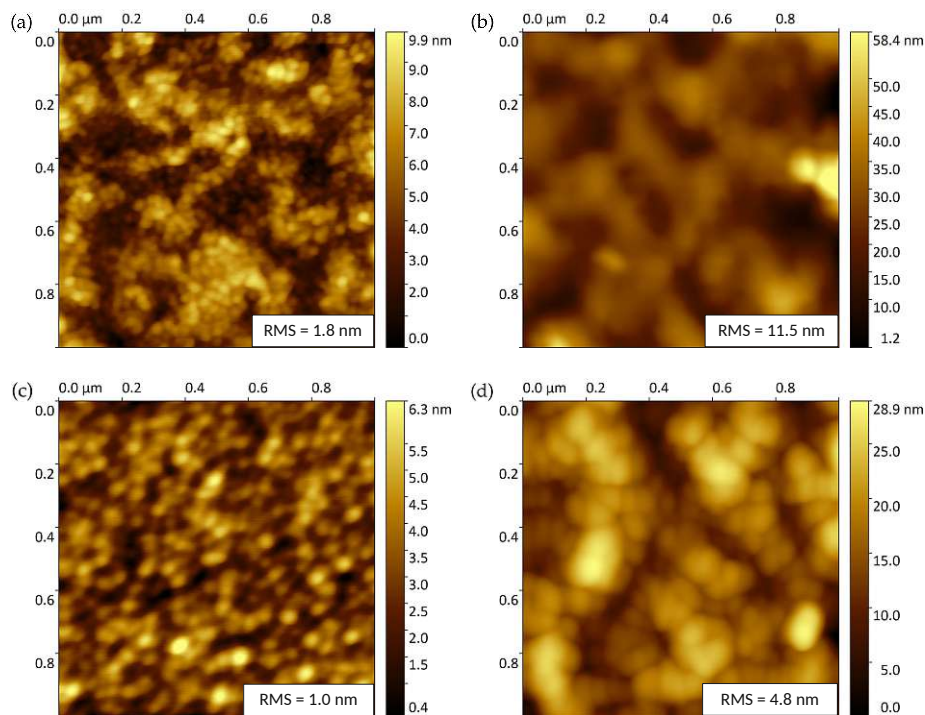


**Figure 3.8:** (a) Schematic representation of the DMD electrode design with Au as metal layer, where  $y$  is the thickness of the base and  $x$  the thickness of the top MTO layer. (b) Transmittance (solid lines) and reflectance (dashed lines) spectra of MTO<sub>40</sub>/Au<sub>10</sub>/MTO<sub>40</sub> electrodes on glass and PET.

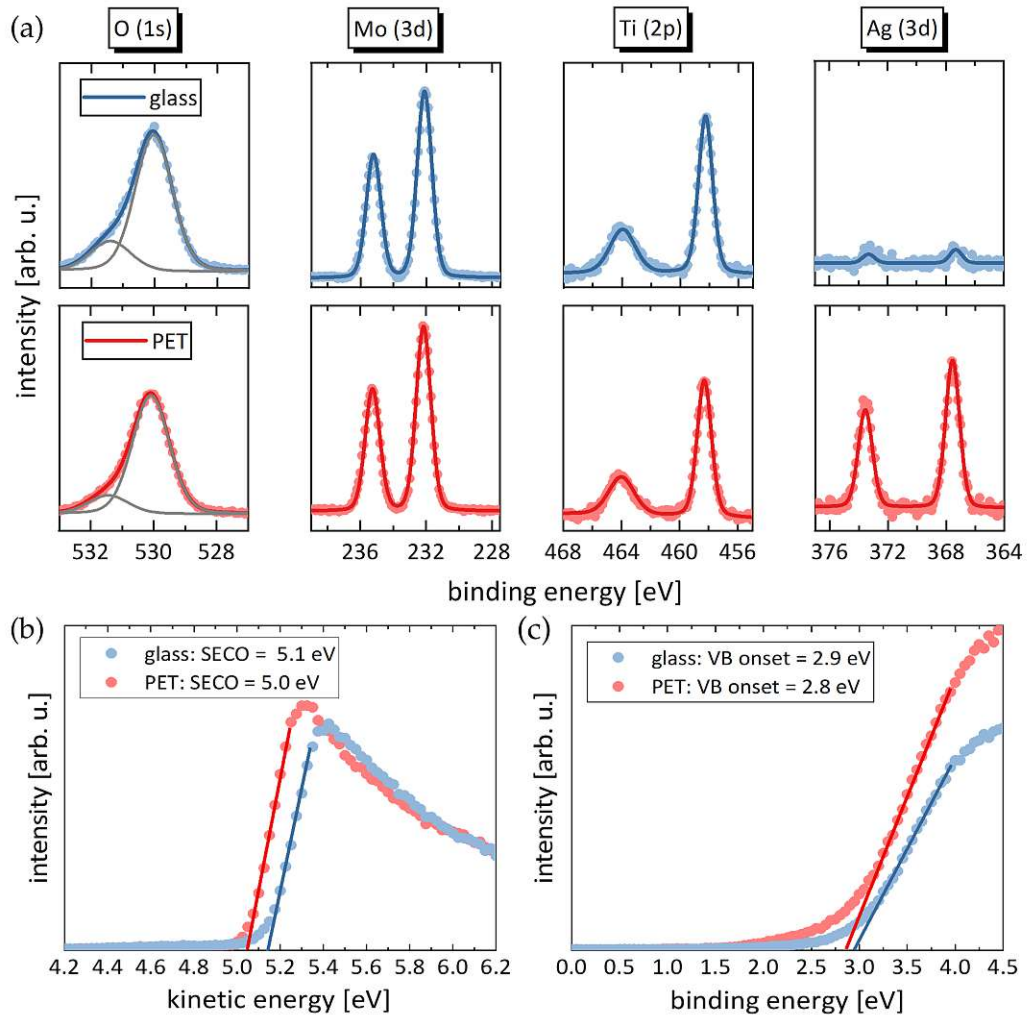
### 3.2.2 Surface morphology, electronic structure and composition

Figure 3.9 displays the  $1 \times 1 \mu\text{m}^2$  AFM images of the DMD on glass and PET, as well as the corresponding bare substrate. The morphology of the electrodes is mostly governed by the underlying substrate. The extracted root mean square value (RMS) for the glass substrate (3.9 (a)) is  $1.8 \pm 0.1 \text{ nm}$  and  $11.5 \pm 4 \text{ nm}$  for the PET substrate (3.9 (b)). The RMS values of the DMD electrodes are even reduced, yielding  $\text{RMS} = 1.0 \pm 0.1 \text{ nm}$  for glass/MTO<sub>40</sub>/Ag<sub>14</sub>/MTO<sub>10/30</sub> (3.9 (c)) and  $\text{RMS} = 4.8 \pm 2 \text{ nm}$  for PET/MTO<sub>40</sub>/Ag<sub>14</sub>/MTO<sub>10/30</sub> (3.9 (d)).

XPS and UPS measurements of the DMD electrodes on glass and PET are performed to determine the electronic structure and composition of MTO. Figure 3.10 (a) shows the XPS results, focused on the O 1s, Mo 3d, Ti 2p and Ag 3d core level regions with scattered dots representing the experimental data and solid lines for the fitted Gaussian/Lorentzian mixed functions. The position and line shape of the Mo and Ti peaks (at 232.1 and 458.3 eV, respectively) indicate that mainly Mo<sup>6+</sup> and Ti<sup>4+</sup> oxidation states are found at the surface. The oxygen spectra are slightly asymmetric and have been deconvoluted in two peaks: the main peak at 530 eV is associated with the oxygen bond to Mo<sup>6+</sup> and Ti<sup>4+</sup>, while the second peak at 531.5 eV is associated with additional oxygen and non-stoichiometric components. The Ti/(Mo + Ti) ratio is extracted from the area underneath the peaks, yielding approx. 35% on both samples.



**Figure 3.9:** AFM images of (a) bare glass, (b) bare PET, (c) MTO/Ag/MTO electrodes on glass, and (d) MTO/Ag/MTO electrodes on PET.



**Figure 3.10:** (a) XPS spectra of MTO<sub>40</sub>/Ag<sub>14</sub>/MTO<sub>10/30</sub> electrodes on glass (blue) and PET (red), (b) UPS measurement in the secondary electron cut-off (SECO) region and (c) in the valence band (VB) region.

The oxygen content was found to be approx. 72% ( $O/(Mo + Ti + O)$ ), irrespective of the deposition conditions. In fact, samples with a non-reactively sputtered top layer (MTO<sub>40</sub>/Ag<sub>14</sub>/MTO<sub>40</sub><sup>Ar</sup>) showed the same oxidation states and atomic ratios on the surface as the reactively sputtered samples. Depth profiling by sequential Ar sputtering has been performed to study the stoichiometry away from the oxidized surface. However, this did not yield reliable results due to preferential sputtering during the Ar bombardment, leading to oxygen loss in all studied cases [80, 81].

Therefore, complementary EDX measurements (Figure 3.11) are performed on 300 nm-thick MTO films on glass to investigate the elemental composition of reactively and non-reactively sputtered MTO films. Although the oxygen contained in the glass substrate contributes to the EDX signal and, thus, distorts the elemental quantification, the oxygen

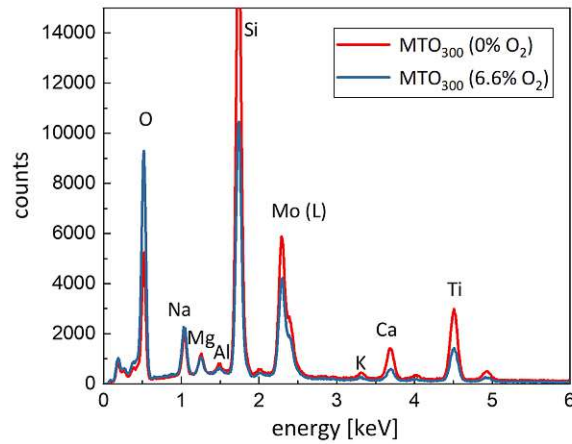


**Figure 3.11:** EDX spectra of reactively and non-reactively sputtered MTO<sub>300</sub> on glass.

content in the non-reactively sputtered film is significantly reduced ( $53 \pm 6$  at.%) compared to the reactively sputtered film ( $68 \pm 7$  at.%). Interestingly, the Ti content also differs depending on the deposition conditions, namely  $\text{Ti}/(\text{Mo} + \text{Ti}) = 49\%$  in the non-reactively sputtered sample and  $\text{Ti}/(\text{Mo} + \text{Ti}) = 40\%$  in the reactively sputtered sample.

Furthermore, the results of UPS measurements on the MTO<sub>40</sub>/Ag<sub>14</sub>/MTO<sub>10/30</sub> electrodes are displayed in Figure 3.10 (b) and (c). From the secondary electron cut-off (SECO), shown in kinetic energy scale, the work function can be extracted, yielding 5.1 eV on glass and 5.0 eV on PET. The onset of the valence band (displayed in binding energy scale for convenience) is found at 2.8 eV (glass) and 2.9 eV (PET) below the Fermi level (at 0 eV in binding energy scale). Interestingly, these values are very similar to what was obtained for MoO<sub>3</sub> films (2.2.2), although TiO<sub>2</sub> generally has a lower work function. Indeed, when mixing two materials with similar density of states but different individual work functions  $\Phi_a$  and  $\Phi_b$ , the work function of the composite material,  $\Phi_m$ , can be assumed as a weighted average of the component's work functions:  $\Phi_m = x\Phi_a + (1 - x)\Phi_b$ , where  $x$  is the amount of component a in the composite [82]. While the work function of TiO<sub>2</sub> usually lies around  $\sim 4.5$  eV [83], the reported work function values for MoO<sub>3</sub> vary between 4.7 to 6.9 eV [41, 39]. This wide range in the observed work function depends on the material's exposure to water. In fact, the reduction of the work function after exposure to ambient atmosphere has been reported for several metal oxides due to the formation of surface dipoles through adsorption of water and subsequent hydroxylation [42]. This effect is especially pronounced in MoO<sub>3</sub> because of its high affinity to hydrolyse (see 4). In contrast to that, the surface hydroxylation and the resulting changes in the work function of TiO<sub>2</sub> are negligible [42]. Thus, for the work function of MTO it is assumed that the expected reduction of the work function due to the mixing of MoO<sub>3</sub> and TiO<sub>2</sub> is



compensated by the overall smaller affinity of the composite material to react with the ambient humidity (see 4).

Figure 3.10 (a) also displays the energy region for the Ag 3*d* levels. Analogous to the MoO<sub>3</sub>/Ag/MoO<sub>3</sub> electrodes (2.2.2), Ag is also found on the surface of the MTO-DMD under certain conditions. While on glass, no distinct Ag peaks are detected, a significant amount of Ag is observed on the surface of the electrode on PET. Again, no metal is detected on the surface by the XPS when Au is used or when the top MTO layer is sputtered without oxygen. However, after exposure to ambient conditions for some weeks or months, small Ag grains are also visible for non-reactively sputtered top layers and for the electrodes on glass since the humidity causes further production of Ag ions through electrochemical reactions in water channels within the grain boundaries and, thus, fosters further Ag diffusion. Indeed, it was found that even after the removal of the Ag from the electrode's surface, the same amount of Ag is again detected on the surface after subsequent exposure to ambient atmosphere. This has been measured using an ICP-MS setup coupled to a flow-cell 8.1.2. To this end, the surface of a MTO<sub>40</sub>/Ag<sub>14</sub>/MTO<sub>10/30</sub> electrode on PET is exposed to a constant flow of DI-water, which is then analysed by the ICP-MS. It should be noted at this point that this is a qualitative measurement and Mo/Ti dissolution will be studied in detail later (see Chapter 4).

During the first run shown in Figure 3.12 (a), one can see a significant amount of Ag dissolving from the surface at the beginning of the measurement. The Ag dissolution rate then decays to practically zero, suggesting the complete removal of Ag from the electrode's surface. After approx. 4 weeks of exposure to ambient conditions, the same sample is re-measured in the ICP-MS (on the same spot). As shown in Figure 3.12 (b), the same amount of Ag is again dissolved from the surface as in the first run, indicating that Ag atoms/ions have migrated to the surface while the sample was stored in air.

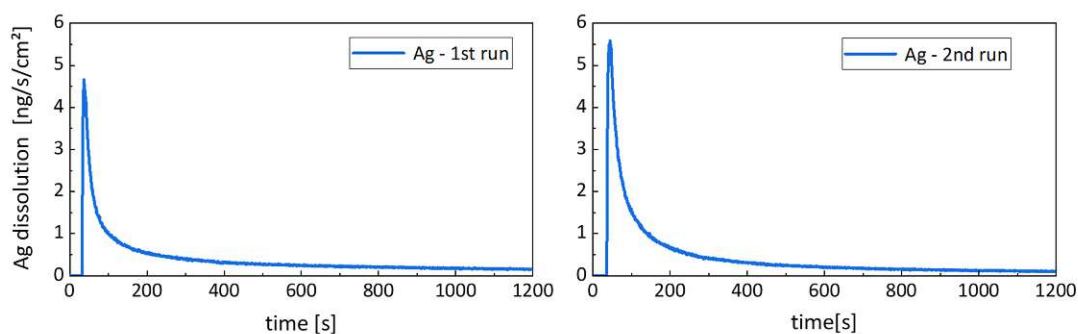


**Figure 3.12:** ICP-MS measurements of Ag dissolution from MTO<sub>40</sub>/Ag<sub>14</sub>/ MTO<sub>10/30</sub> electrodes on PET.

### 3.2.3 Mechanical and chemical stability

The mechanical stability MTO<sub>40</sub>/Ag<sub>14</sub>/MTO<sub>10/30</sub> electrodes on PET is tested analogously to MoO<sub>3</sub>-based DMDs in section 2.2.3. With a bending radius of 5 mm, compressive and tensile stress is applied for 2000 cycles and the resistance is measured in the unstrained state along the strain direction. The relative increase of resistance as a function of bending cycles is shown in Figure 3.13 for both cases. Exertion of compressive stress leads to a relative increase of only  $\sim 1.2$  after 2000 bending cycles. Under tensile stress, the DMD shows a stronger increase in resistance after 700 cycles up to a factor of  $\sim 3.3$  after 2000 cycles. However, after releasing the sample from the test stand, a relaxation effect is observed, resulting in a reduction of the electrode's resistance. After a few days in the relaxed state, the relative resistance increase after bending under tensile stress was found below 2.2. The SEM image reveals small cracks in the dielectric after bending, similar to the MoO<sub>3</sub>-based DMDs, but the Ag layer is still intact, preventing electrical failure of the electrode (as compared to common conductive oxides like ITO shown in section 2.2.3).

To test their chemical stability, the MTO<sub>40</sub>/Ag<sub>14</sub>/MTO<sub>10/30</sub> electrodes are spin-coated with two different formulations of PEDOT:PSS, a toluene-based dispersion (Clevious HTL Solar 3) and a water-based dispersion (Clevious PH1000). Contrary to MoO<sub>3</sub>-based DMDs, both PEDOT:PSS formulations can be used without visible degradation of the MTO-DMDs and they maintain their sheet resistance. Cross-sectional SEM images in Figure 3.14 confirm that the DMD stays intact even when water-based PEDOT:PSS (PH1000) is applied, suggesting an increased water stability of MTO. Indeed, when exposing an

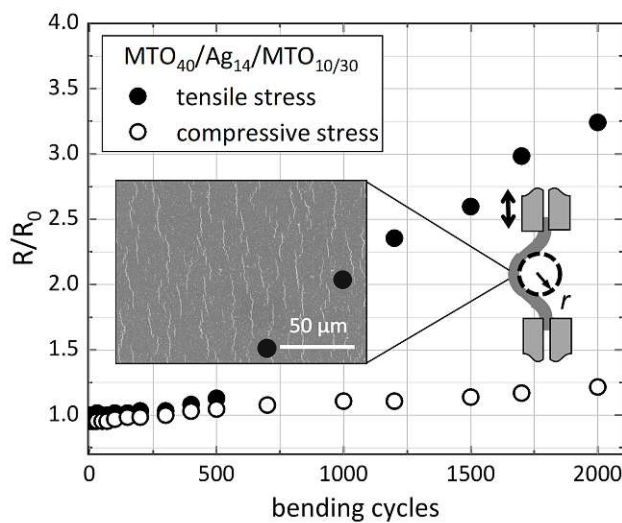


**Figure 3.13:** Evolution of the relative resistance of PET/MTO<sub>40</sub>/Ag<sub>14</sub>/MTO<sub>10/30</sub> electrodes as a function of bending cycles. The inset shows a SEM image of the DMD surface after 2000 cycles upon tensile stress.

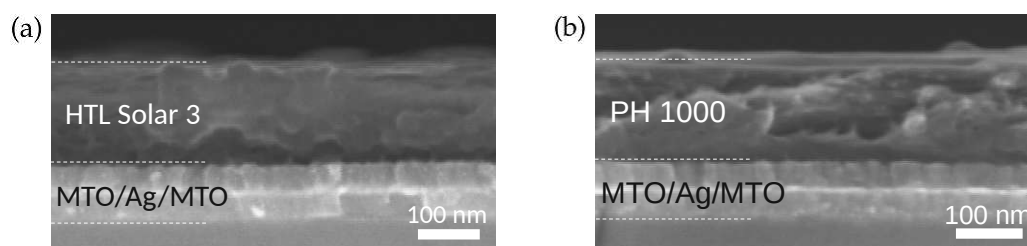


**Figure 3.14:** SEM cross-sectional image of glass/MTO<sub>40</sub>/Ag<sub>14</sub>/MTO<sub>10/30</sub> coated with (a) toluene-based HTL Solar 3 formulation of PEDOT:PSS and (b) water-based PH1000 PEDOT:PSS.

MTO layer to water, no immediate dissolution is observed, making processing with water-based solutions possible. However, a detailed study of the water stability of MTO in comparison to MoO<sub>3</sub> is presented in Chapter 4.

### 3.3 SUMMARY

The present chapter reported on the sputter deposition of mixed molybdenum titanium oxide layers from a specially designed sputter target in DC magnetron mode. With 6.6% oxygen in the process gas transparent oxide layers and high deposition rates up to 17 nm/min could be achieved. The optical and electronic properties of the MTO layers, having an indirect optical band gap of 3.2 eV and a work function of  $\sim 5$  eV, were found similar to undoped MoO<sub>3</sub>. In analogy of the previous chapter, MTO was used for the design of MTO/(Ag or Au)/MTO transparent electrodes on glass and PET substrates. With Ag as metal layer, the electrodes have an average visible transmittance above 70% and low sheet resistance of  $\sim 5 \Omega/\text{sq}$ . Together with their significantly higher mechanical stability, the MTO-based electrodes on PET outperform the commercial ITO.



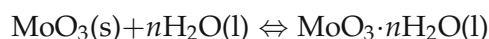
---

## WATER STABILITY OF MOLYBDENUM OXIDE AND MTO

---

In the previous chapters the stability of sputtered molybdenum oxide layers in water was mentioned briefly. In fact, the observation that MoO<sub>3</sub>-based electrodes quickly dissolve when in contact with water has motivated the use of MTO, which allowed the processing with water-based solutions.

For the chemical stability of MoO<sub>3</sub>, it is important to mention that hydrates of MoO<sub>3</sub> (molybdic acids) are common and represented by the formula MoO<sub>3</sub>·*n*H<sub>2</sub>O (e.g. the dihydrate MoO<sub>3</sub>·2H<sub>2</sub>O, monohydrate MoO<sub>3</sub>·H<sub>2</sub>O, or hemi-hydrate MoO<sub>3</sub>·1/2H<sub>2</sub>O). The hydration occurs either by substitution of an oxygen atom in the octahedron by a coordinated water molecule, or by the insertion of water within the layers of the stratified crystal structure [84]. The presence of water can lead to the dissolution of MoO<sub>3</sub> through the formation of such hydrates, according to the reaction[85, 86]:



Nevertheless, the (possible) dissolution of MoO<sub>x</sub> thin films in water has not been discussed widely in literature and can lead to seemingly contradictory results. This originates in the fact that the dissolution of MoO<sub>x</sub> depends very sensitively on various material properties such as the oxidation state, (surface) defects and the crystal structure.

For instance, Rietwyk et al. [42] investigated the effect of air exposure on the work function of several metal oxides and found a universal reduction of the work function due to water adsorption. This effect is particularly pronounced in MoO<sub>x</sub> and significant changes in the energy levels after air exposure have also been reported by others [34, 62, 61]. When water interacts with a surface, it adsorbs and, depending on the material and surface properties (such as stoichiometry, surface structure, coordination and defect concentration), it can dissociate into reactive H<sup>+</sup> and OH<sup>-</sup> species, a process known as hydrolysis. Sian and Reddy [63] studied the effect of the film stoichiometry and microstructure on the hydrolysis behaviour of MoO<sub>x</sub> using Fourier Transform Infrared Spectroscopy (FTIR). They found that structurally disordered, but stoichiometric films are especially prone to hydrolysis, while crystalline or highly non-stoichiometric films show no or strongly reduced water adsorption and hydrolysis. More recent experiments and calculations have revealed the role of oxygen vacancies on leveraging the energy barrier for water

adsorption on a  $\text{MoO}_3$  surface [64]. Another study by Head et al. [65] confirms that water adsorption is suppressed on defect-free  $\text{MoO}_3$  surfaces due to the stability of the terminal oxygen. Only when oxygen vacancies are introduced can water adsorb to unsaturated Mo sites, enabling its dissociation. However, an excess of oxygen vacancies, as in highly non-stoichiometric  $\text{MoO}_x$ , leads to metallic Mo-Mo bonds and a partial occupation of the Mo  $4d$  orbital (which is empty in stoichiometric  $\text{MoO}_3$ ), which hampers the dissociation of water as the charge transfer from the  $\text{OH}^-$  to the  $4d$  orbital is hindered [63, 78, 38].

The objective of the studies presented in the following chapter was to investigate the effect of the aforementioned material properties on the  $\text{MoO}_x$  stability in water and compare it with the mixed MTO.

#### 4.1 DISSOLUTION EXPERIMENTS

*The results in this section have been published in:*

Goetz, S. et al. *Fast sputter deposition of  $\text{MoO}_x$ /metal/ $\text{MoO}_x$  transparent electrodes on glass and PET substrates. Journal of Materials Science 56, 9047–9064 (2021). [33]*

*and in*

Goetz, S. et al. *Transparent electrodes based on molybdenum–titanium–oxide with increased water stability for use as hole-transport/hole-injection components. Journal of Materials Science 57, 8752–8766 (2022). [56]*

While the dissolution of a quickly dissolving film is easy to observe empirically, the temporal and elemental quantification of the dissolution process needs more experimental effort. To this end, a special flow-cell setup connected to an inductively-coupled mass spectrometer (ICP-MS) has been deployed to compare the dissolution of different molybdenum oxide samples. Upon flow of DI water through the cell and over the sample surface, the element-resolved dissolution rate of the film was measured as a function of time (for more details see 8.1.2).

##### 4.1.1 *The stability of $\text{MoO}_x$ in liquid water*

It was empirically observed that the stability of the amorphous  $\text{MoO}_x$  layers in water depends on their stoichiometry. Prolonged exposure of reactively-sputtered, highly transparent films as well as the  $\text{MoO}_x$ -based DMD electrodes in ambient conditions of humidity leads to their slow degradation, with the samples assuming a bluish tint that suggests formation of reduced species. Visual changes become visible after few days of

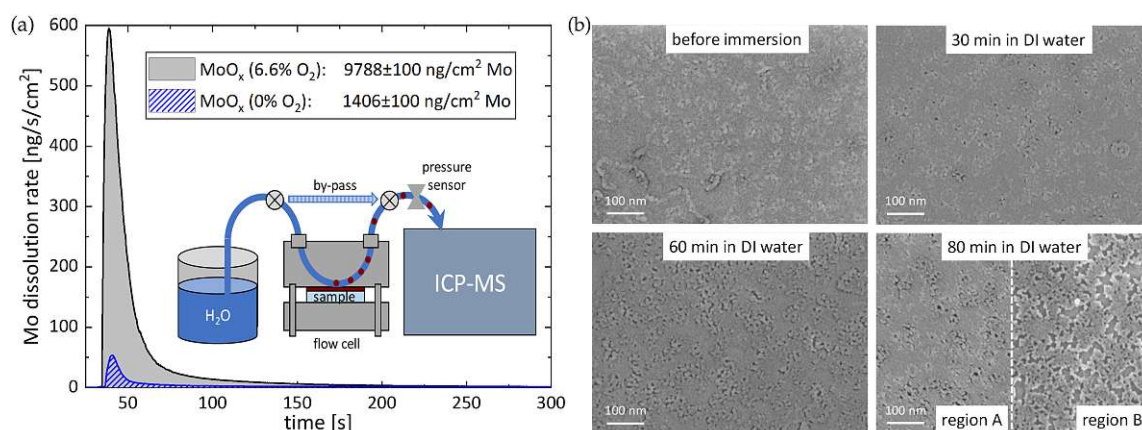


**Figure 4.1:** (a) ICP-MS experiments for two  $\text{MoO}_x$  layers, one sputtered with oxygen and the other without. (b) SEM images of the  $\text{MoO}_x$  layer sputtered without oxygen, after being immersed in DI water for increasing duration. For the largest duration (80 min) two regions from the same film, A and B, are depicted at different degrees of film degradation.

ambient humidity exposure. The immersion of these films into DI or tap water leads to their fast and complete disintegration. On the other hand, optically absorbing  $\text{MoO}_x$  films, sputtered without oxygen in the plasma, show much higher stability in ambient conditions of humidity or when immersed in water.

To support these empirical observations, 40 nm-thick  $\text{MoO}_x$  films were deposited on glass, with and without oxygen in the plasma. The coated glass samples were mounted to a flow cell, coupled with a downstream ICP-MS analysis, as shown in the inset of Figure 4.1. The film sputtered in 6.6%  $\text{O}_2$  was completely dissolved within  $\sim 2$  minutes. The total amount of dissolved Mo is  $\sim 10000$  ng/cm<sup>2</sup>, which roughly corresponds to the Mo quantity contained in the total film thickness (40 nm), if we assume the density of the film to be close to the one of  $\text{MoO}_3$ , i.e. 4.7 g/cm<sup>3</sup> [87]. On the contrary, the dissolution of the non-reactively sputtered film (also 40 nm in thickness), is significantly reduced (Figure 4.1 (a)). The ICP-MS measurements yield that only the oxidized superficial layer ( $\sim 5$  nm, with stoichiometry close to  $\text{MoO}_3$ ) is readily dissolved, while the subsequent dissolution of the oxygen-deficient underlying layer is dramatically reduced. SEM observations of these (non-reactively sputtered) films, after long immersion periods in DI water, showed that slow degradation does take place, with pinholes in the films increasing in number and size with the duration of immersion (Figure 4.1 (b)). In some areas of the film (region B in Figure 4.1 (b)) these pinholes eventually grouped to form larger pits. A certain degree of spatial inhomogeneity in the films' stoichiometry or distribution of defects on the surface may account for the existence of such regions in the film, where the water-triggered degradation is more pronounced compared to other regions (such as region A in Figure 4.1 (b)). These observations are consistent with the findings of Sian and Reddy [63], who studied  $\text{MoO}_x$  films of different microstructures and stoichiometries exposed to ambient air humidity, by infrared spectroscopy. They reported that amorphous, nearly

stoichiometric  $\text{MoO}_x$  films (with  $x \approx 3$ ) contain the largest amount of hydrolyzed Mo-OH bonds. In comparison, highly non-stoichiometric amorphous films contain the smallest amount. These bonds arise from dissociative adsorption of water species (to  $\text{H}^+$  and  $\text{OH}^-$ ) on the metal oxide surface, and the subsequent hydroxylation of the Mo-O bonds. This is explained by the acid-base mechanism, where the electron lone pairs of  $\text{OH}^-$  (arising from  $\text{H}_2\text{O}$  dissociation) must be transferred to the  $4d$  vacant orbitals of Mo. In non-stoichiometric films,  $4d$  orbitals are partially filled, impeding the electron transfer, i.e. the growth of hydrolyzed bonds is slowed down [63]. Interestingly, highly stoichiometric but polycrystalline films did not show hydrolyzed bonds. In the present study, this could not be verified, since all the investigated films were amorphous. It shows, however, that a disordered, defect-rich surface catalyzes dissociation in water.

#### 4.1.2 Comparing the stability of MTO and $\text{MoO}_x$

Opposite to what was observed for  $\text{MoO}_x$ , long-term exposure to ambient conditions and even direct contact with water does not produce any changes on MTO films or MTO-based DMD electrodes that are visible by eye. In order to quantify the stability of MTO in water, 40 nm thick single layers were investigated using the ICP-MS setup. Figure 4.2 (a) presents the dissolution rate of Mo from a reactively sputtered MTO layer as a function of time in comparison to the dissolution of  $\text{MoO}_x$  (as shown in Figure 4.1). While the  $\text{MoO}_x$  ( $x \approx 3$ ) layer is completely dissolved within the 10 minutes of the experiment (again assuming a density of  $4.7 \text{ g/cm}^3$ , the 40 nm of  $\text{MoO}_x$  contain approx.  $10000 \text{ ng/cm}^2$  of Mo), the amount of Mo dissolved from the MTO layer is reduced by a factor of 20 to roughly  $500 \text{ ng/cm}^2$ . In a rough estimation, assuming the same density and a Mo:Ti

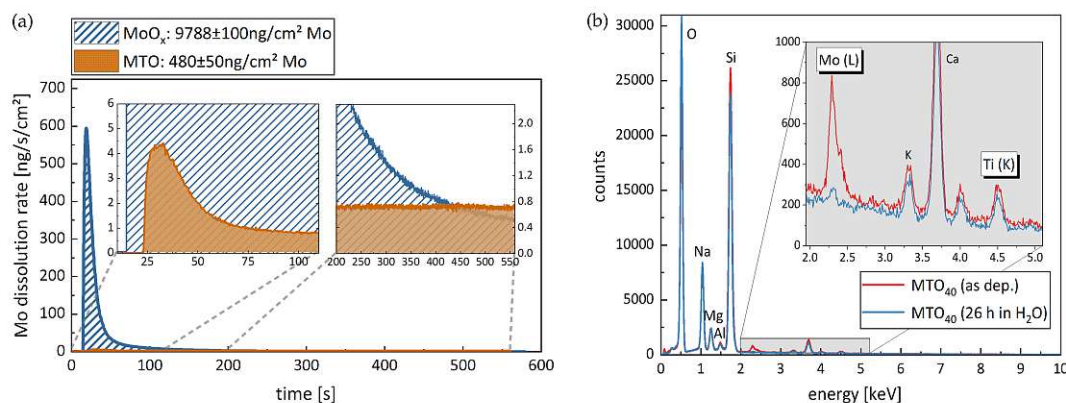


**Figure 4.2:** (a) Dissolution rate of Mo from 40 nm thick  $\text{MoO}_x$  and MTO layer as a function of time. The insets show zoom-ins at different times and the legend includes the total amount of dissolved Mo within 10 minutes. (b) EDX spectra of 40 nm thick MTO layer before and after 26 hours of immersion in DI water.



ratio of 60:40, the total amount of dissolved MTO corresponds to approximately 2 nm that are dissolved within the 10 minutes of measurement. It should be noted at this point, that the total amount of dissolved Ti was only 2 ng/cm<sup>2</sup> and is therefore neglected. As shown in the right inset of Figure 4.2 (a), the Mo dissolution rate remains constant for MTO, after a peak-dissolution at the beginning (left inset). This implies that even though the MTO is more stable than MoO<sub>x</sub>, Mo keeps dissolving from the MTO layer as long as water flows over the sample. And since the Ti dissolution is smaller than expected from the elemental ratio, a certain Ti passivation is expected, which further slows down the Mo dissolution but cannot completely prevent it. In fact, immersion of a 40 nm thick MTO layer in DI-water for 26 hours yields a Mo-depleted and Ti-rich residual layer, according to EDX measurements (Figure 4.2 (b)). As responsible mechanism for the observed significant reduction of the MTO dissolution in water, the following is proposed. An oxide's resistance to dissolution is strongly related to its affinity to hydrolyse, i.e. to dissociate H<sub>2</sub>O molecules on the surface and form hydroxyl bonds. When the hydrolysis process is viewed from the perspective of acid-base reactions between the metal cations (Lewis acids) and the OH<sup>-</sup> (Lewis base from the dissociation of H<sub>2</sub>O on the oxide surface), the surface acidity is reduced with the decrease of the formal charge/oxidation state of the cations [88]. The presence of Ti (in the form of Ti<sup>+4</sup> ions) decreases the average cation formal charge of the material and thus, decreases the tendency to hydrolyse.

#### 4.2 HUMIDITY-DRIVEN DEGRADATION

*This section is based on a manuscript with the title "Humidity-driven degradation of sputtered molybdenum oxide and molybdenum-titanium-oxide thin films" submitted to the Journal of Materials Chemistry C.*

To investigate the reaction with water, i.e. the hydrolysis, in more detail and in a more quantifiable manner, the degradation of the films is monitored in controlled humidity conditions over extended time periods of up to 30 days, leading to changes of the films' composition, crystallinity and surface topography, depending on the relative humidity level. The relative humidity (RH) was fixed using saturated salt solutions, which create controlled air humidity levels above the solution inside a closed container. To this end, approx. 30 g of magnesium nitrate hexahydrate (Mg(NO<sub>3</sub>)<sub>2</sub> · 6H<sub>2</sub>O from Sigma Aldrich) were dissolved in 20 mL DI-water, yielding 54% RH. Accordingly, 9 g of sodium chloride (NaNO<sub>3</sub> from Sigma Aldrich), 18 g of ammonium sulphate ((NH<sub>4</sub>)<sub>2</sub>SO<sub>4</sub> from Sigma Aldrich), 10 g of potassium chloride (KCl from Sigma Aldrich) and 4 g of potassium sulphate (K<sub>2</sub>SO<sub>4</sub> from Sigma Aldrich) were dissolved in 20 mL DI-water to create 78%, 81%, 84% and 97% RH, respectively.

The impact of humidity on sputtered MTO films is investigated by infrared (IR) spec-

troscopy and compared to  $\text{MoO}_3$ . To eliminate any absorption contributions from the glass substrate, a 150 nm-thick Au layer was introduced between the substrate and the  $\text{MoO}_x$  and MTO films, yielding a distinct baseline for further absorption peak analysis. It should be clarified at this point that in the following discussion the valleys in the reflectance spectra are referred to as 'peaks', as they correspond directly to the absorption peaks considering that the transmittance is zero. It is noted at this point, that the  $\text{MoO}_x$  films for this Chapter were sputtered from a different target, namely a  $\text{MoO}_{2.9}$  target. However, the sputtering conditions were the same as reported in Chapter 2 and the resulting layers showed the same properties as the layers sputtered from the  $\text{MoO}_{2.7}$ .

There are three IR absorption bands which have been associated with the hydrolysis of  $\text{MoO}_3$  [63]. The stretching mode of  $\text{H}_2\text{O}$  lies between  $3400\text{--}3500\text{ cm}^{-1}$  (peak 1), which is related to adsorbed water molecules on the surface. The peaks at  $3200\text{--}3250\text{ cm}^{-1}$  (peak 2) and  $3020\text{--}3040\text{ cm}^{-1}$  (peak 3) are associated with the formation of hydrolysed bonds. These are formed through the dissociation of  $\text{H}_2\text{O}$  on the surface, leading to  $\text{H}^+$  and  $\text{OH}^-$  species, which then bind to O and Mo atoms for peak 2 and peak 3, respectively. To study the hydrolysis behaviour and the related degradation of  $\text{MoO}_3$  and MTO, films are exposed to controlled humid conditions with 54%, 81% and 97% RH at room temperature ( $22\text{--}24^\circ\text{C}$ ) over a time period of 30 days.

The time evolution of IR reflectance spectra of 300 nm-thick  $\text{MoO}_3$  and MTO films (sputtered with oxygen) in 54% RH is shown in Figure 4.3 (a) and (b), respectively. There is already a broad peak in the as-deposited  $\text{MoO}_3$  samples, measured directly after taking them out of the vacuum, which is associated with adsorbed water molecules (peak 1). This means that as soon as  $\text{MoO}_3$  is in contact with ambient humidity, water is adsorbed on the surface. To estimate the peak height, a straight line between the data points at  $2600$  and  $3800\text{ cm}^{-1}$  is used as baseline and the difference between the baseline and the spectrum at the peak position is then defined as the peak intensity. The peak intensity

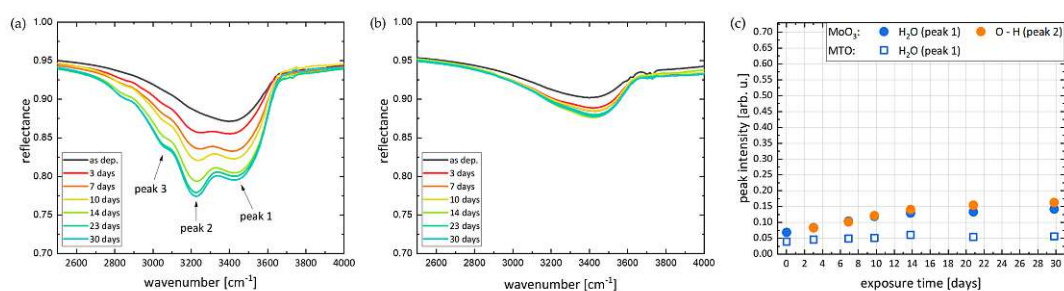


**Figure 4.3:** (a), (b) Time evolution of reflectance spectra of 300 nm thick  $\text{MoO}_3$  and MTO films, respectively, exposed to 54% RH. (c) Corresponding peak intensities extracted from the reflectance spectra.

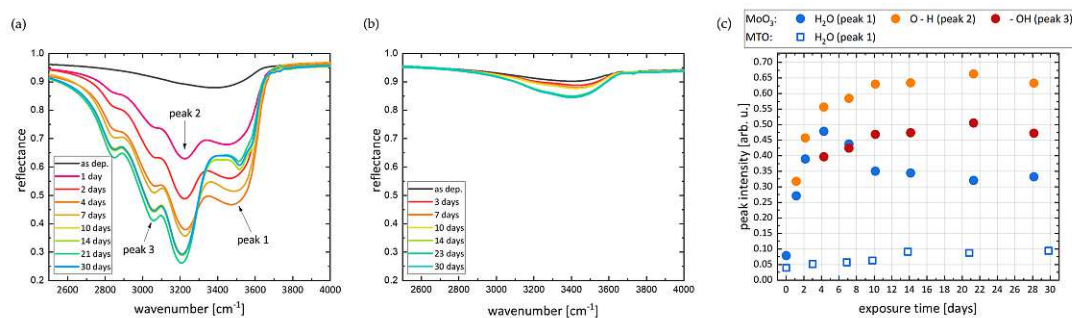


**Figure 4.4:** (a), (b) Time evolution of reflectance spectra of 300 nm thick MoO<sub>3</sub> and MTO films, respectively, exposed to 81% RH. (c) Corresponding peak intensities extracted from the reflectance spectra.

as a function of the exposure time is shown in Figure 4.3 (c) for MoO<sub>3</sub> and MTO films, respectively. This shows that in MoO<sub>3</sub>, peak 1 grows with the exposure time, indicating a continuous water uptake. Additionally, a new peak around 3240 cm<sup>-1</sup> arises with increasing exposure time, which corresponds to the O-H bond (peak 2) originating from the hydrolysis process. After one week, peak 2 becomes higher than peak 1, suggesting that the adsorbed water is continuously dissociated, and forms hydrolysed bonds. At this point, also a shoulder at the position of the Mo-OH bond (peak 3) starts to form. With H<sup>+</sup> being lighter, it can penetrate the film more easily than OH<sup>-</sup>, leading to a faster growth of peak 2 [63]. For MTO, the water adsorption is reduced compared to MoO<sub>3</sub>, as the intensity of peak 1 is significantly smaller in the as-deposited sample and the growth rate of the peak is also reduced. Moreover, the hydrolysis is hampered and no additional peaks are observed, apart from a very weak shoulder of peak 2.

In the next step, the hydrolysis is further accelerated by exposing the 300 nm thick MoO<sub>3</sub> and MTO films to a higher RH of 81%. The corresponding IR spectra and peak intensities are shown in Figure 4.4. For MoO<sub>3</sub>, similar changes of the IR spectrum are observed in 81% RH as in 54%, but with much higher rate and intensity. Already after 4 days of exposure, the water peak reaches a maximum and strong absorptions from the hydrolysed bonds are visible. After 7 days, some of the adsorbed water is consumed to form further Mo-OH and Mo-O-H bonds. As the hydrolysis proceeds, the intensity of peak 2 and peak 3 increases, while peak 1 is reduced until all available sites are saturated, and no further changes are observed. It is noted at this point that the shape of peak 1 changes drastically as soon as saturation is reached. This is attributed to a crystallisation process, which will be discussed in more detail in the following. Also, it is worth noting that another peak around 2850 cm<sup>-1</sup> is continuously growing, which has not been assigned in the literature. However, since this peak is growing at the same rate and with the same shape as peak 2 and peak 3, it could be attributed to overtone bands of OH absorptions. In contrast to MoO<sub>3</sub>, the changes in the spectra of the MTO film are significantly smaller, indicating a

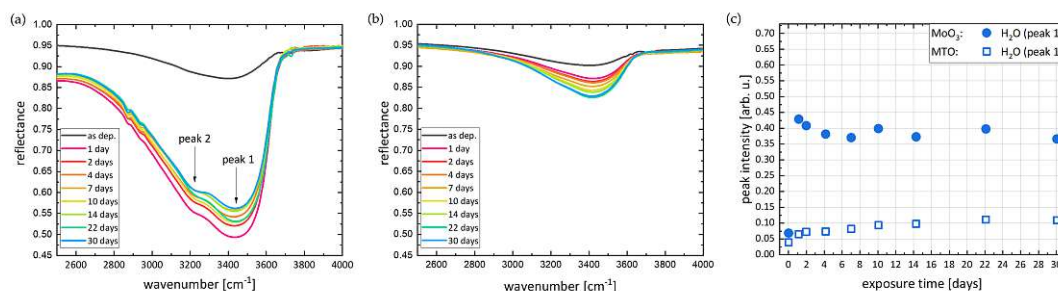


**Figure 4.5:** (a), (b) Time evolution of reflectance spectra of 300 nm thick MoO<sub>3</sub> and MTO films, respectively, exposed to 97% RH. (c) Corresponding peak intensities extracted from the reflectance spectra.

strongly reduced reaction. The H<sub>2</sub>O peak grows significantly slower, reaching saturation after 14 days of exposure at 21% of the maximal water uptake in MoO<sub>3</sub>. Furthermore, the formation of hydrolysed bonds is negligible in MTO as only a very weak shoulder of peak 2 is observed in the IR spectra.

Finally, the same samples are exposed to 97% RH and the evolution of the IR spectra is shown in Figure 4.5. Again, the IR spectrum of MoO<sub>3</sub> changes significantly as soon as the sample is exposed to humidity. Peak 1 reaches a maximum intensity of 0.43 within 1 day and remains constant for prolonged exposure. Interestingly, only a small amount of the adsorbed water is consumed to form Mo-O-H bonds in this high humidity: peak 2 only appears as a weak shoulder and peak 3 is completely absent. It is assumed that the immediate saturation of available sites with H<sub>2</sub>O due to the high vapor pressure leaves no active sites for subsequent hydrolysis, thus suppressing the formation of hydroxylated bonds. Similarly, there is no hydrolysis in the MTO film. However, the amount of adsorbed water slowly increases with time until saturation is reached at a peak intensity of approx. 0.11, which accounts for only 25% of the maximal H<sub>2</sub>O peak height in MoO<sub>3</sub>. This confirms the reduced reaction rate for MTO compared to MoO<sub>3</sub>.

As described in the previous Chapter 4.1.2, the increased water stability of MTO is mainly attributed to the incorporated Ti atoms. The tendency of a material to hydrolyse and consequently to dissolve is reduced with the decrease of the average oxidation state [88].

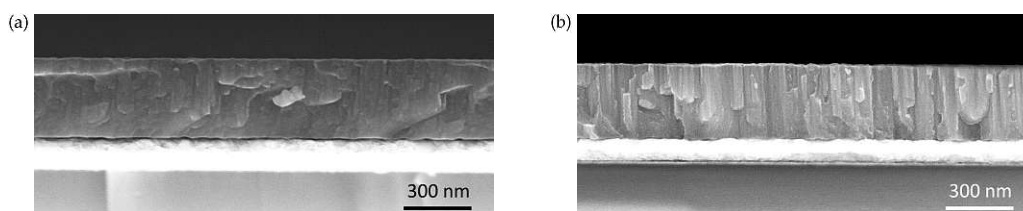


**Figure 4.6:** SEM cross-section images of as-deposited (a) MoO<sub>3</sub> and (b) MTO film on glass/Au.

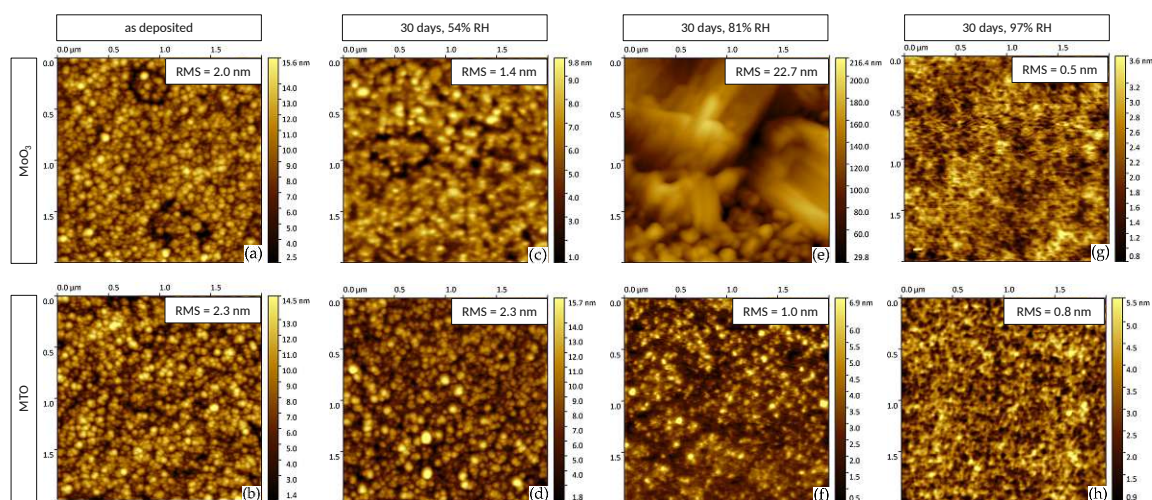


**Figure 4.7:** AFM topography images of MoO<sub>3</sub> (top) and MTO (bottom) films on Au-coated glass substrates at different degradation stages: (a), (b) as-deposited, (c), (d) after 30 days in 54% RH, (e), (f) after 30 days in 81% RH and (g), (h) after 30 days in 97% RH. The root mean square (RMS) roughness is shown for each case.

Since Ti is present in the form of Ti<sup>+4</sup> cations, the average oxidation state in MTO is reduced compared to pure MoO<sub>3</sub> with Mo<sup>+6</sup>, making MTO less prone to water adsorption and hydrolysis. In fact, the presence of TiO<sub>2</sub> does not only hamper the H<sub>2</sub>O on the Ti sites but seems to also reduce the water uptake for the whole MTO layer, as the peak height reduction is bigger than the Ti content in the film with 35–40%. This may also be related to moderate changes in the film morphology. Indeed, when comparing the SEM cross section images of MoO<sub>3</sub> and MTO films (Figure 4.6), one can distinguish a more columnar growth of the MTO layer compared to MoO<sub>3</sub>.

Even though both materials are amorphous according to XRD measurements (2.1.2, 3.1.2), nanocrystalline, columnar structures appear in MTO. While MoO<sub>3</sub> exhibits a typical amorphous network where water penetrates easily, the reduced structural disorder of MTO may additionally decrease water ingress to the bulk. Since it is known, that (poly-)crystalline MoO<sub>3</sub> has much lower affinity to hydrolyse [65], the degree of structural disorder is considered as influential factor here. Although the nanocrystalline structure provides grain boundaries, where water can penetrate the MTO film, the grains themselves are assumed to be more structured and thus, more resistant to water ingress than the completely amorphous MoO<sub>3</sub> layer. However, these structural differences are rather small and do not significantly affect macroscopic features such as the film density.

The humidity-driven changes in the discussed films are also observed in 2 × 2 μm<sup>2</sup> AFM images shown in Figure 4.7. The as-deposited samples present a compact and dense grain structure with a root-mean-square (RMS) roughness of 2.0 nm for MoO<sub>3</sub> and 2.3 nm for MTO. The surface topography is mostly dominated by the underlying glass/Au substrate with RMS = 1.1 nm. After the degradation in 54% RH for 30 days, the MTO surface

morphology and the corresponding RMS value do not show any detectable changes. The surface of  $\text{MoO}_3$ , however, appears smoothed and with blurred grain contours, giving rise to a reduced RMS roughness of 1.4 nm. To rule out that the smoothing is caused by tip-related artefacts, reference (non-degraded) samples were measured under the same conditions and no such effect has been observed. The smoothing is thus attributed to the adsorbed water on the surface. After exposure to 97% RH, the AFM images show a transformed surface with a rather porous structure. Again, the effect is more pronounced for  $\text{MoO}_3$  than for MTO, but both samples have drastically reduced RMS roughness of 0.5 and 0.8 nm, respectively. Exposure to 81% RH yields significant changes in the surface topography in  $\text{MoO}_3$ . While the MTO surface is mainly smoothed, with reduced grain sizes and RMS roughness of 1.0 nm, the  $\text{MoO}_3$  layer is completely transformed, with the formation of crystallites, which cause the dramatic increase of the RMS roughness to 22.7 nm. In fact, the AFM image reveals the presence of two different kinds of crystals: small pyramid-shaped grains (at the bottom of the image), along with large accumulations of needle-like crystals (at the top). XRD measurements, shown in Figure 4.8, confirm the layer's crystallisation. The as-deposited film is amorphous, having no additional peaks other than the ones stemming from the Au substrate. Already after 10 days of humidity exposure, distinct peaks appear at low diffraction angles, which increase in intensity after 30 days. However, the exact identification of the crystal phase was not possible from these measurements due to the overlap of several possible crystal phases. Nevertheless, some hypotheses can be made based on complementary EDX measurements (Table 4.1). These show an increase of N in the degraded films (from approx. 4.5 to 9 at.%), which may be related to the ammonium contained in the salt solution that could evaporate and react with the  $\text{MoO}_3$  film to form a hydrated ammonium molybdate phase. Another possibility is the diffusion of Na from the glass substrate into the  $\text{MoO}_3$  film to form a sodium molybdate compound. Such a Na accumulation has been observed for other

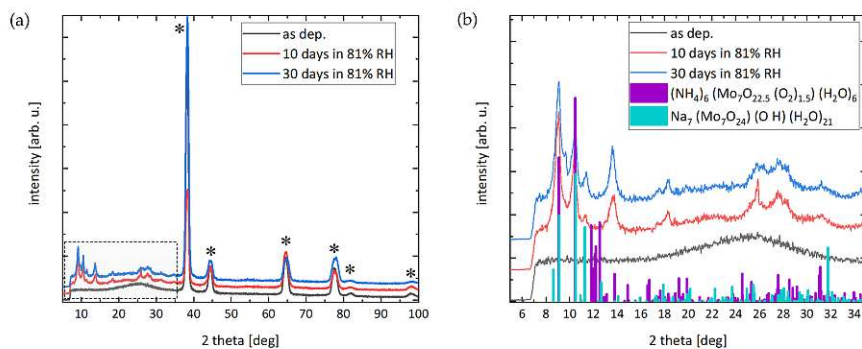


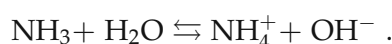
**Figure 4.8:** (a) X-ray diffractogram of  $\text{MoO}_3$  before and after the degradation in 81% RH. The peaks marked with an asterisk (\*) correspond to Au. (b) Zoom-in of (a) including the reference reflections of possible crystal phases.

sample	N	O	Na	Mg	Al	Si	S	K	Ca	Mo	Au
as-dep.	4.567	65.267	2.317	1.533	1.100	5.767	0.5333	0.450	0.883	9.767	8.300
30 days	9.267	65.700	0.800	0.433	0.233	7.167	1.533	0.200	0.767	7.700	6.267

**Table 4.1:** Elemental quantification of EDX measurements on 300 nm thick MoO<sub>3</sub> before and after 30 days in 81% RH. The values are the average of measurements of several different spots on the sample, given in at.% and include the contributions from the underlying soda-lime glass substrate.

MoO<sub>3</sub> samples deposited on glass when exposed to humidity and cannot be excluded according to the XRD results. In fact, the presence of both or even multiple phases is possible, and the distribution of the respective phases and orientations appears to be very sensitive and complex.

To verify the reaction mechanism, MoO<sub>3</sub> is additionally exposed to other salt solutions in the vicinity of 80% RH, namely at 78% and 84% RH. The resulting IR spectra are shown in Figure 4.9 and compared to the spectra of an ammonia-containing 81% RH reference sample. In 78% RH, significant hydrolysis is observed, with an increased reaction rate compared to 54% RH. However, the peak intensities after 30 days are still much smaller (by a factor of 1/2 for the O-H peak (peak 2)) than for the 81% RH, which cannot only be explained by the slightly lower humidity value. Instead, it is assumed that the ammonia indeed reacts with the MoO<sub>3</sub> film and enhances the hydrolysis process acting as catalyst for the water dissociation. It is hypothesised that NH<sub>3</sub> species evaporate from the salt solution and associate on the MoO<sub>3</sub> surface, where they contribute to the water dissociation according to



This contributes additional hydrolysed bonds in MoO<sub>3</sub>, resulting in dramatically increased peak intensities and finally leading to the crystallisation of the layer. At higher humidity (84% RH), the IR spectrum changes again, yielding similar spectra as in 97% RH, where

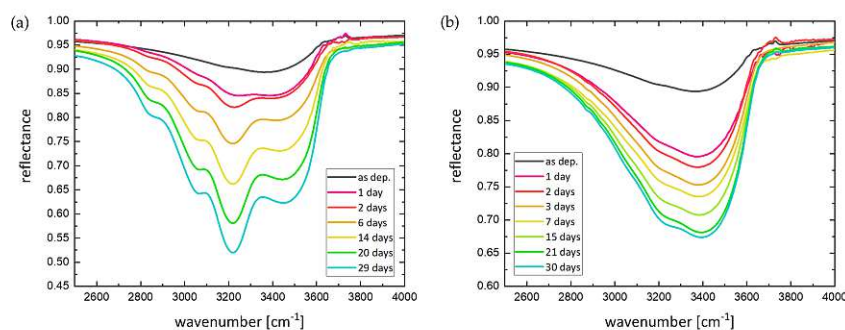


**Figure 4.9:** Time evolution of IR reflectance spectra of 300 nm thick MoO<sub>3</sub> films in (a) 78% RH and (b) 84% relative humidity.

an immediate saturation of active sites with H<sub>2</sub>O was observed. However, the reaction rate and the peak intensities are decreased in 84% RH, such that saturation is only reached after 21 days. In both cases (78% and 84%) no crystallisation is observed within the considered time period, which confirms that increased reaction in 81% RH is caused by NH<sub>4</sub>. The observed reaction mechanism is consistent over the different solutions and is thus attributed to the humidity. At first, the observed hydrolysis rate increases with increasing RH, leading to similar patterns in the IR spectra but with increasing peak intensities. Then, as the RH reaches a certain level, the adsorption rate of H<sub>2</sub>O becomes too high and the active sites for hydrolysis are blocked, resulting in a dominant H<sub>2</sub>O peak with a weaker shoulder at the position of the Mo-O-H bonds. We would like to highlight at this point that the MTO is much more stable even under intensified conditions when NH<sub>3</sub> is present. Hence, the additional Ti prevents not only the hydrolysis but also stabilizes the material against other chemical reactions and crystallisation.

For comparison, oxygen-deficient MoO<sub>3-x</sub> (with  $x < 1$ ) and MTO films, which are sputtered in pure Ar atmosphere, were exposed to 97% RH. When sputtering without oxygen, both materials, MoO<sub>x</sub> and MTO, have increased optical absorption and higher electrical conductivity, i.e. an increased amount of metallic bonds. While there is no change in the oxygen-deficient MTO spectra, the spectra of MoO<sub>3-x</sub> are similar to the oxygen rich MoO<sub>3</sub> films (in Figure 4.5), but the water adsorption proceeds with a lower rate (see Figure 4.10), since the intensity of peak 1 gradually increases with time reaching saturation only after 3 weeks. As the adsorption rate is decreased, there are more reactive sites for hydrolysis. Hence, the Mo-O-H bond (peak2) appears a bit more pronounced than for the MoO<sub>3</sub> sample.

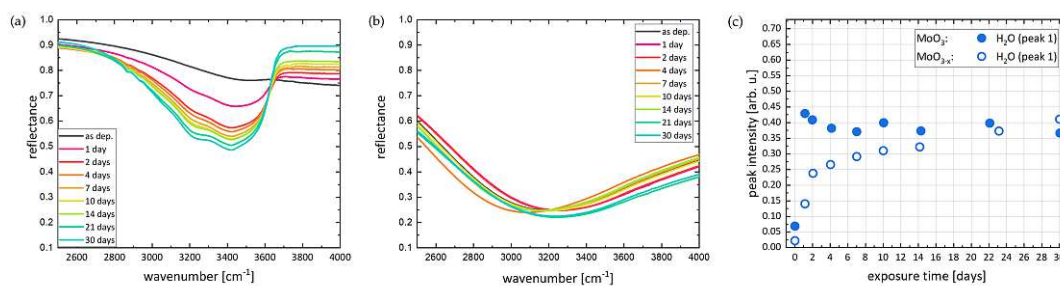


**Figure 4.10:** Time evolution of IR reflectance spectra of 300 nm thick, oxygen-deficient (a) MoO<sub>3-x</sub> and (b) MTO (0% O<sub>2</sub>) films in 97% RH. (c) Corresponding peak intensities of MoO<sub>3-x</sub> films as a function of exposure time to 97% RH in comparison to MoO<sub>3</sub>



### 4.3 SUMMARY

Dissolution experiments using a flow-cell set-up coupled to an ICP-MS showed that reactively sputtered  $\text{MoO}_3$  films are readily dissolved in water, while sub-stoichiometric, non-reactively sputtered films are more resistant to water dissolution. Moreover, it was demonstrated that the Mo dissolution from an MTO layer is reduced by a factor of 20, even for the reactively sputtered MTO. The stabilizing mechanism is attributed to the reduction of the average oxidation state of the material by the presence of  $\text{Ti}^{+4}$  compared to pure  $\text{MoO}_3$  with  $\text{Mo}^{+6}$ .

Using infrared spectroscopy, the reaction processes of  $\text{MoO}_3$  with water, i.e. water adsorption, dissociation and formation of Mo-O-H and Mo-OH bonds, were observed in controlled humidity conditions and compared to MTO. While the water ingress in  $\text{MoO}_3$  films leads to hydrolysis and detrimental changes in surface topography, the MTO layers show around 75% reduced water adsorption and, subsequently, almost no hydrolysis is observed. The reaction rates of  $\text{MoO}_3$  with  $\text{H}_2\text{O}$  increase with increasing relative humidity level, firstly enhancing the formation of hydrolysed bonds until water adsorption is dominant above 84% RH. In fact,  $\text{MoO}_3$  is not only instable against water, but also reacts easily with Na and ammonia, leading to crystallisation and phase transformation of the film by exposure to humidity in the presence of the respective compounds.



---

## NIOBIUM-DOPED TITANIUM OXIDE – TNO

---

*The following chapter is based on the article:*

*Goetz, S. et al. Low-Temperature-Processed Transparent Electrodes Based on Compact and Mesoporous Titanium Oxide Layers for Flexible Perovskite Solar Cells. ACS Applied Energy Materials. (2021). Reprinted with permission from <https://doi.org/10.1021/acsaem.1c01129> [89], according to the copyright agreement in 8.2. Copyright 2021 American Chemical Society.*

In this chapter, sputter-deposited, niobium-doped TiO<sub>2</sub> (TNO) is investigated for the design of flexible transparent DMD electrodes. In fact, TNO has been proposed as transparent conductive oxide to replace ITO [90, 91] with Nb<sup>5+</sup> acting as n-type dopant in TiO<sub>2</sub> to enhance electrical conductivity [92, 93, 94]. Here, the use of an oxide sputter target doped with Nb offers the necessary electrical conductivity to permit sputter deposition in DC magnetron mode, without obligatory use of reactive plasma. Under these conditions, the sputter rate is significantly enhanced compared to conventional RF mode or reactive sputtering, facilitating high-throughput, industrial-scale fabrication.

The combination with ultrathin Ag and Au layers yields flexible DMD electrodes on polyethylene terephthalate (PET) substrate with visible transmittance above 0.70 and sheet resistance below 10 Ω/sq. The idea is that the DMD electrode based on TiO<sub>2</sub> could simultaneously act as transparent electrode and electron transport layer (ETL). There are several reports on TiO<sub>x</sub>/Ag/TiO<sub>x</sub> multilayer stacks used as transparent electrodes in flexible solar cells. For example, Jung et al. [95] report on flexible PSCs on nanopaper using a TiO<sub>x</sub>/Ag/TiO<sub>x</sub> electrode. Similarly, Li et al. [96] employed the same DMD structure for ultra-flexible PSCs on cellophane. However, in these works, additional ETLs of ZnO and CPTA (C60 pyrrolidine tris-acid) were employed.

In contrast to that, the present chapter shows that the developed DMD electrodes can be ideally combined with a low-temperature and solution-processed mesoporous TiO<sub>2</sub> layer to act as electron transport layer for subsequent implementation in perovskite solar cells.

## 5.1 CHARACTERIZATION OF TNO THIN FILMS

## 5.1.1 DC magnetron sputtering of TNO

Reactive sputtering, i.e. deposition of a metal oxide layer from a metal target in the presence of oxygen, is known to have decreasing deposition rates for increasing supply of reactive species, as well as complex reaction processes, causing different compound stoichiometries [16]. However, industrial applications require high deposition rates (at least several nm/min), good reproducibility and low processing temperatures ( $\leq 100^\circ\text{C}$ ) to enable high throughput fabrication of thin oxide layers, especially on flexible substrates. To this end, a doped titanium oxide target is used in this work to sputter oxide layers in a pure Ar atmosphere. Doping with Nb increases the electrical conductivity of the target, thus, enabling sputtering in DC mode, which also contributes to higher deposition rates in comparison to RF sputtering. The TNO films were sputtered from a 10.16 cm diameter titanium oxide target doped with 5 at.% Nb (from Plansee, AT), at a process pressure of 5  $\mu\text{bar}$  and varying sputter power. With increasing sputter power,  $P$ , from 42 to 243 W, a linear increase of the deposition rate,  $r$ , is observed (Figure 5.1), following the relation:  $r = (0.069 \pm 0.001)P$ . The deposition rate at a sputter power of 42 W (0.52 W/cm<sup>2</sup> power density) is 2.9 nm/min and reaches a value of 16.8 nm/min at 243 W (3 W/cm<sup>2</sup>).

So far, TNO was deposited using either RF sputter mode [97, 98] or reactive DC sputtering [99, 100] from a metallic target, generally leading to smaller deposition rates. As a comparison, for reactive sputtering from a Ti target, deposition rates of 0.8 nm/min for a DC power density of 4.8 W/cm<sup>2</sup> [31], up to 3.6 nm/min for a DC power density of 4.4 W/cm<sup>2</sup> [96] are reported. Similarly, a deposition rate of 2 nm/min is reported for a DC

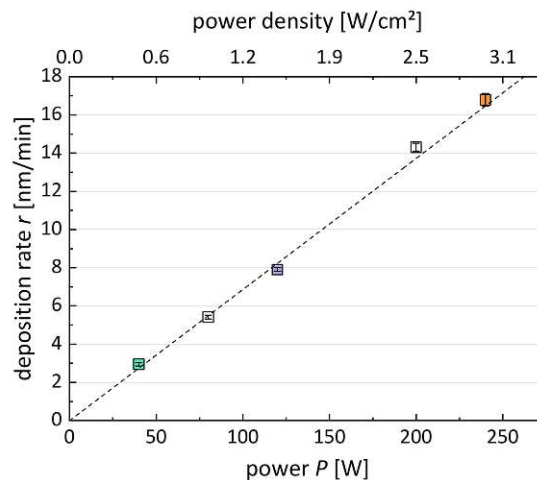


**Figure 5.1:** Deposition rate  $r$  versus power  $P$  and the corresponding power density for the sputtered TNO films.

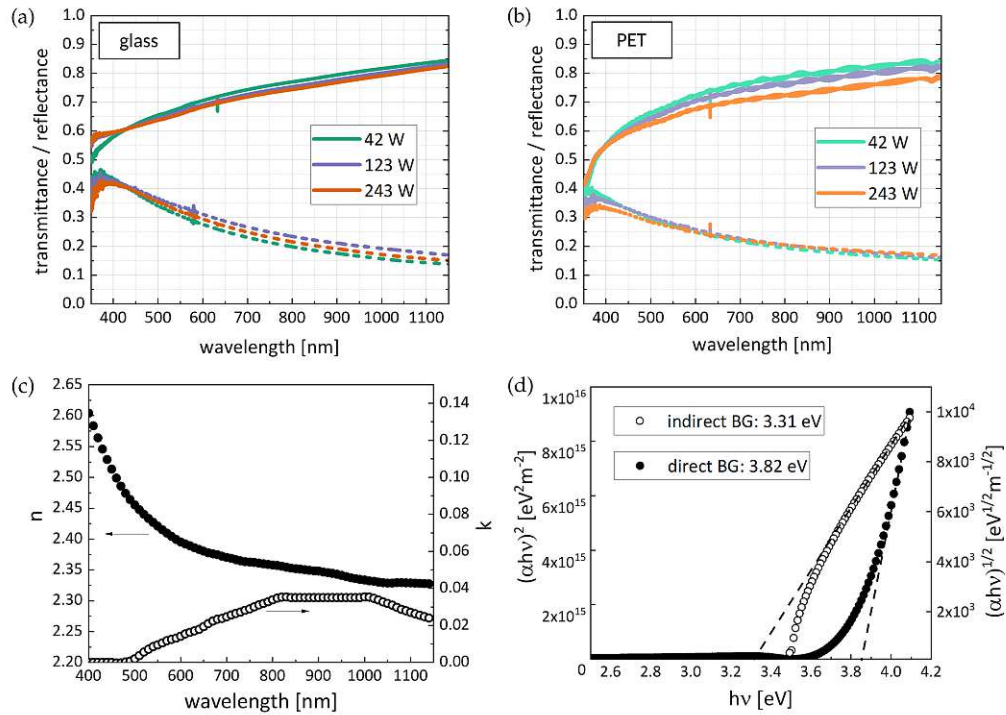


**Figure 5.2:** Transmittance and reflectance spectra of TNO layers on (a) glass and (b) PET, sputtered in Ar atmosphere and at different DC power. (c) Real ( $n$ ) and imaginary part ( $k$ ) of the TNO refractive index. (d) Tauc plots used for the extraction of the direct (left axis) and indirect (right axis) band gap BG.

power density of  $2.3 \text{ W/cm}^2$ , when using reactive sputtering from a metallic, Nb-doped (3.2 at.%) Ti target [94]. As shown in Figure 5.2 (a) and (b), non-reactive sputtering gives transparent films in the applied sputter power range, on both glass and PET substrates. The following experiments are all conducted at 123 W to prevent any damage to the sputter target due to excessive heating and still have a considerable deposition rate of  $7.9 \text{ nm/min}$ . The transmittance values of the 40 nm thick films deposited on glass and PET (solid lines) are similar, suggesting similar growth of the films on both substrates. The dashed lines in Figures 5.2 (a) and (b) present the reflectance spectra. The spectra of the sample deposited at 123 W on glass are used to extract the complex refractive index (Figure 5.2 (c)). The real part of the refractive index,  $n$ , shows high values, as expected for  $\text{TiO}_2$  and agree with results for Nb-doped  $\text{TiO}_2$  in the literature [101, 102]. The small values of the imaginary part  $k$  (the extinction coefficient) confirm low absorption within the film. Additionally, the optical band gap energy (Figure 5.2 (d)) is extracted from the transmittance and reflectance spectra of the films on glass using the Tauc method (8.1.4). The Tauc plot for direct transitions (left axis, using  $n = 2$  in the exponent of the ordinate  $(\alpha \cdot hv)^n$ ), yields a band gap energy of 3.82 eV. The plot for indirect transitions (right axis,  $n = 1/2$ ), yields a smaller band gap energy of 3.31 eV. The error in the band gap extraction is estimated at 0.05 eV, stemming from the uncertainty in the linear regime considered for

the fitting. However, for amorphous materials, as it is the case for the presented layers (shown later), one usually considers an indirect band gap [103], which also agrees well with the values for Nb-doped  $\text{TiO}_2$  around 3.3 eV reported in the literature [91, 104].

### 5.1.2 Crystal structure and annealing effects

The following section presents additional data which has not been published elsewhere.

As mentioned before, the as-sputtered TNO layers are amorphous, yielding no XRD signals other than from the glass substrate (see Figure 5.3 (a)). In order to crystallize the films, high temperatures of 400°C or larger are required. To this end, 100 nm thick films are sintered in a small muffle furnace at 400°C, 500°C and 600°C. After ramping the temperature up with a rate of 2°C/min, the final temperature was held for 1 hour before letting cool down slowly. The resulting XRD patterns in Figure 5.3 (a) show the formation of a  $\text{TiO}_2$  Anatase (COD: 9008213) phase, independent of the temperature, with a pronounced (011) reflection.

Figure 5.3 (c) includes the SEM images after annealing, where domain boundaries become visible. Interestingly, the domains of the 400°C-sample show a variation in the contrast which suggests either differences in the electrical conductivity or different crystallite orientations. The same is visible, but reduced for the 500°C-sample and vanishes when annealed at 600°C. However, there is no evidence for preferred crystal orientation

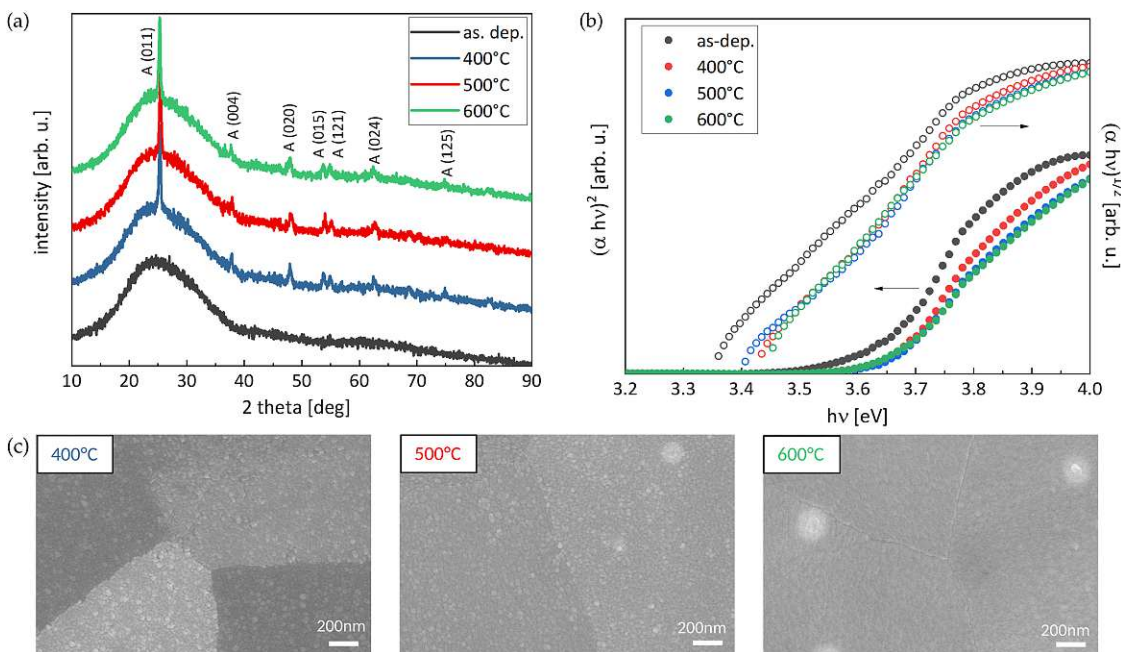


**Figure 5.3:** (a) XRD pattern of 100 nm thick TNO layers on glass annealed at 400°C, 500°C and 600°C. (b) Tauc plots for indirect optical transitions and (c) SEM images of the respective samples.

in the XRD data, where all samples show the same pattern. When measured with the multimeter, the resistivity of all annealed films was above the detection threshold. As the annealing is performed in air, without controlled gas flow, it is likely that oxygen vacancies are removed. This agrees with the fact that the films are still not electrically conductive and they become more transparent. The latter is confirmed in the Tauc plot in Figure 5.3 (b), where the indirect band gap (BG) increases after annealing from 3.3 eV to 3.4 eV. The Tauc plots for direct transitions is also included in Figure 5.3 (b), but shows less distinct linear behaviour than the one for the indirect band gap. However, for the annealed samples, a linear fit is possible, yielding direct band gap values around 3.6 eV. In accordance with the band gap, the average visible transmittance increases continuously from 77.5% to 81.1% in the annealed samples.

Generally, for the oxide to become conductive, reducing conditions are required to increase the oxygen deficiency and to activate the  $\text{Nb}^{5+}$  dopant [94, 97].

## 5.2 TRANSPARENT ELECTRODES BASED ON TNO

### 5.2.1 DMD architecture

Despite the Nb doping, the sputtered TNO layers have a high resistivity of  $\sim 90 \Omega \cdot \text{cm}$  (measured for a 500 nm thick layer, without annealing). However, due to the high refractive index, TNO can act as suitable dielectric layer in DMD (dielectric/metal/dielectric) transparent electrodes to achieve high transmittance values. For what concerns the choice of metal, Ag provides the lowest optical losses in the visible, followed by Au and Cu [79], while it also features the highest electrical conductivity and moderate cost. On the other hand, Ag (and Cu) is chemically highly reactive, which can be a disadvantage when it

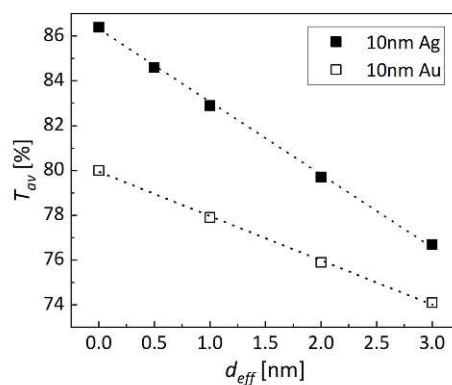


**Figure 5.4:** Calculated maximal average transmittance ( $T_{av}$ ) as a function of the effective medium thickness ( $d_{eff}$ ) for TNO/metal/TNO stacks with 10 nm Ag and Au.

comes to implementation in devices. In this respect, Au is known to be chemically inert, but of course, with high cost. Further experiments were concentrated on both Ag and Au metals, in consideration of their respective, aforementioned advantages.

To determine the layer thicknesses for the DMD that maximize the average transmittance  $T_{av}$  in the visible range (400-700 nm), TMM simulations are performed. While the Ag or Au thickness is fixed to 10 nm (where the metal layer is still transparent but well above the percolation threshold), the thickness of the two TNO layers is varied between 0 and 100 nm. The substrates are assumed infinitely thick and the substrate/air interface is added subsequently in the calculations. For the DMD on glass and PET, a 1 nm- and 2 nm-thick effective medium layer ( $d_{eff}$ ), respectively, is introduced on each side of the metal layer to account for interface roughness [105]. The respective  $d_{eff}$  values were the ones yielding best agreement between simulated and experimental spectra. In general, the thickness of this effective medium layer  $d_{eff}$  has a critical influence on the average transmittance values, as shown in Figure 5.4, with the maximum  $T_{av}$  decreasing with  $d_{eff}$ .

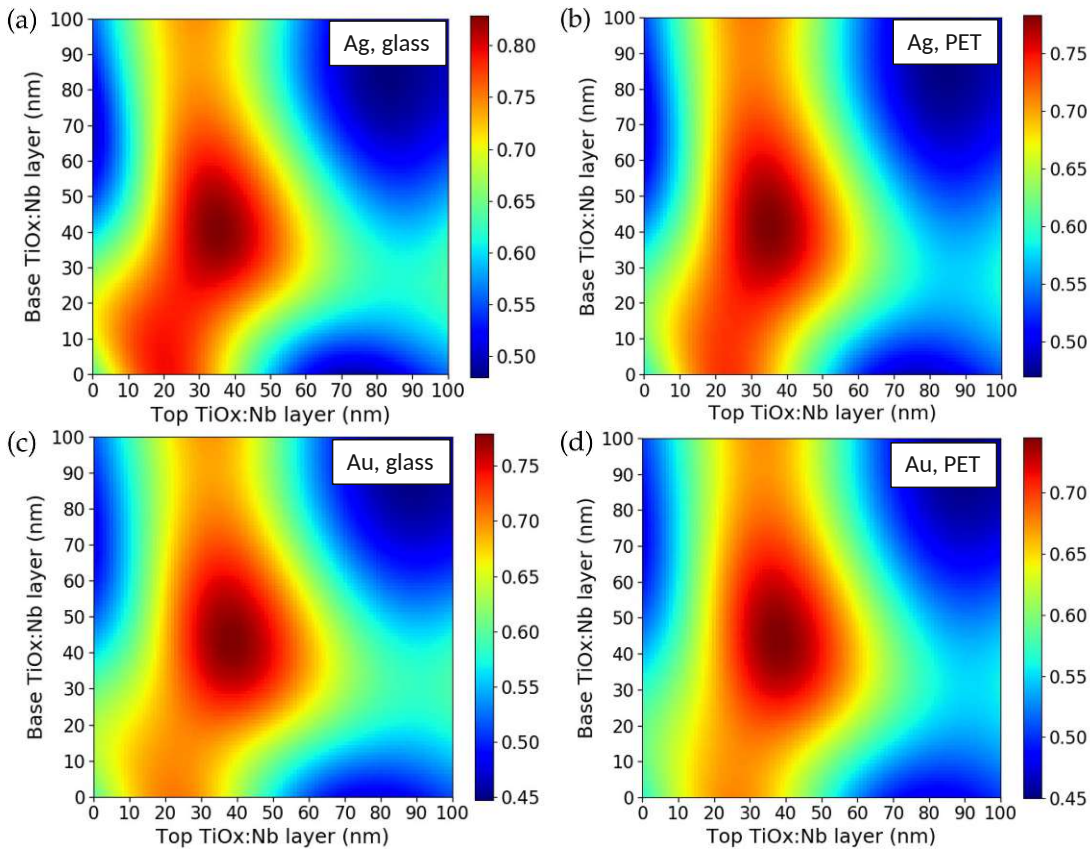


**Figure 5.5:** TMM calculations of the average transmittance in the visible range (400-700 nm) of DMD stacks with varying TNO (dielectric) thickness for (a) glass/TNO<sub>y</sub>/Ag<sub>10</sub>/TNO<sub>x</sub>, (b) PET/TNO<sub>y</sub>/Ag<sub>10</sub>/TNO<sub>x</sub>, (c) glass/TNO<sub>y</sub>/Au<sub>10</sub>/TNO<sub>x</sub> and (d) PET/TNO<sub>y</sub>/Au<sub>10</sub>/TNO<sub>x</sub>.



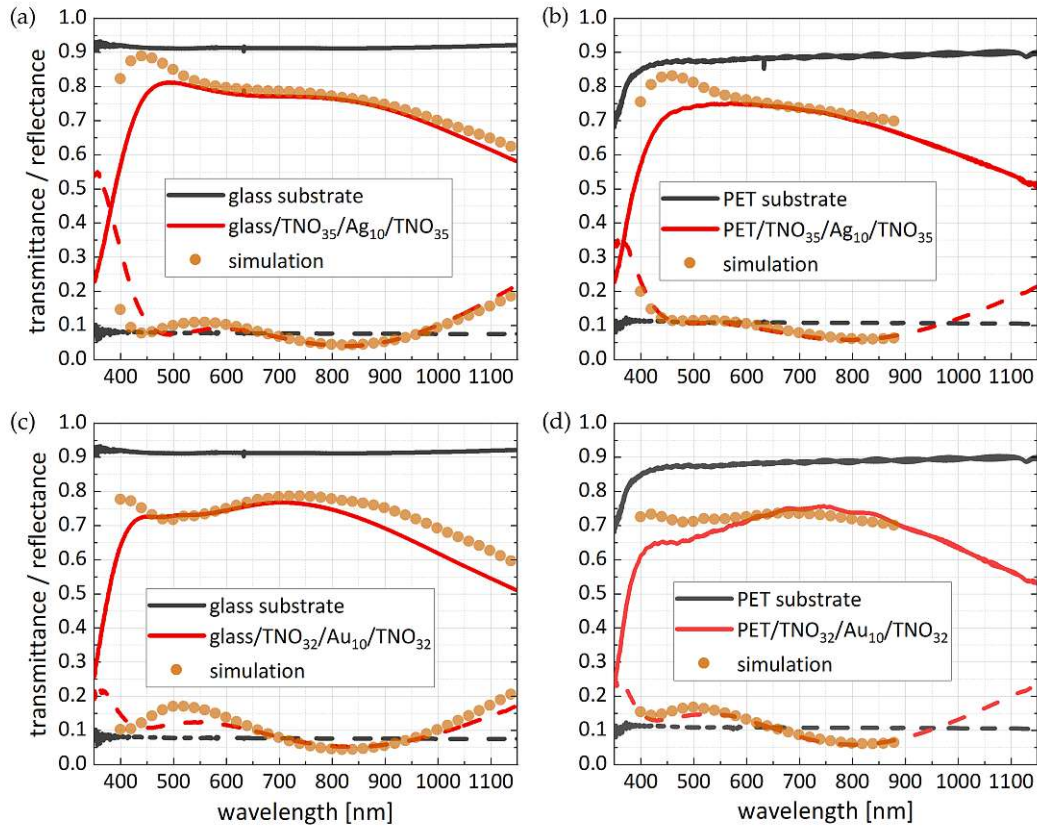


**Figure 5.6:** Transmittance (solid lines) and reflectance (dashed lines) spectra of the DMD electrodes in comparison to the spectra of the corresponding substrate and the TMM simulation of the respective layers (dots).

For Ag-based DMDs, the maximum  $T_{av}$  is 0.83 and 0.78 for glass and PET, respectively, achieved for a 41 nm base and 35 nm top TNO layer (Figure 5.5). For the Au-based DMDs, the maximum  $T_{av}$  is 0.78 and 0.75 for glass and PET, respectively, for a 44 nm base and 38 nm top TNO layer. One has to take into consideration that the dielectric layer thicknesses that maximize  $T_{av}$  also depend on the layers in the final device. All factors considered, the simulations show that for the introduced DMDs there exists a wide window of dielectric thickness values (around 40 nm) offering high optical transmittance. Figures 5.6 show the measured transmittance (solid lines) and reflectance (dashed lines) spectra of the sputtered electrodes in comparison with the bare glass and PET substrate. The sputter power for the TNO films in the DMD stack was also 123 W. After a screening of the electrode performance around the simulated maximum  $T_{av}$ , the optimal dielectric thicknesses were experimentally determined at 35 and 32 nm for both TNO layers, for Ag- and Au-based electrodes, respectively, giving rise to symmetric DMD stacks. The resulting spectrum of  $\text{TNO}_{35}/\text{Ag}_{10}/\text{TNO}_{35}$  features a plateau with high transmittance in the visible, yielding  $T_{av} = 0.77$  on glass and 0.73 on PET, with sheet resistance,  $R_s$ , of  $7.3 \pm 1.0$  and  $7.6 \pm 0.7 \Omega/\text{sq}$  on glass and PET, respectively. For comparison, the simulated

sample	$T_{av}$	$T_{max}$	$R_s$ [ $\Omega$ /sq]	$\Phi \cdot 10^{-3}$ [ $\Omega^{-1}$ ]
glass/TNO <sub>35</sub> /Ag <sub>10</sub> /TNO <sub>35</sub>	0.77	0.81	$7.3 \pm 1.0$	$10.1 \pm 1.3$
PET/TNO <sub>35</sub> /Ag <sub>10</sub> /TNO <sub>35</sub>	0.73	0.75	$7.6 \pm 0.7$	$5.6 \pm 0.5$
glass/TNO <sub>32</sub> /Au <sub>10</sub> /TNO <sub>32</sub>	0.74	0.77	$8.9 \pm 1.2$	$5.5 \pm 0.7$
PET/TNO <sub>32</sub> /Au <sub>10</sub> /TNO <sub>32</sub>	0.69	0.74	$9.2 \pm 0.6$	$2.7 \pm 0.2$

**Table 5.1:** Summary of the optical and electrical performance of DMD electrodes, including Haacke’s figure of merit ( $\Phi$ ).

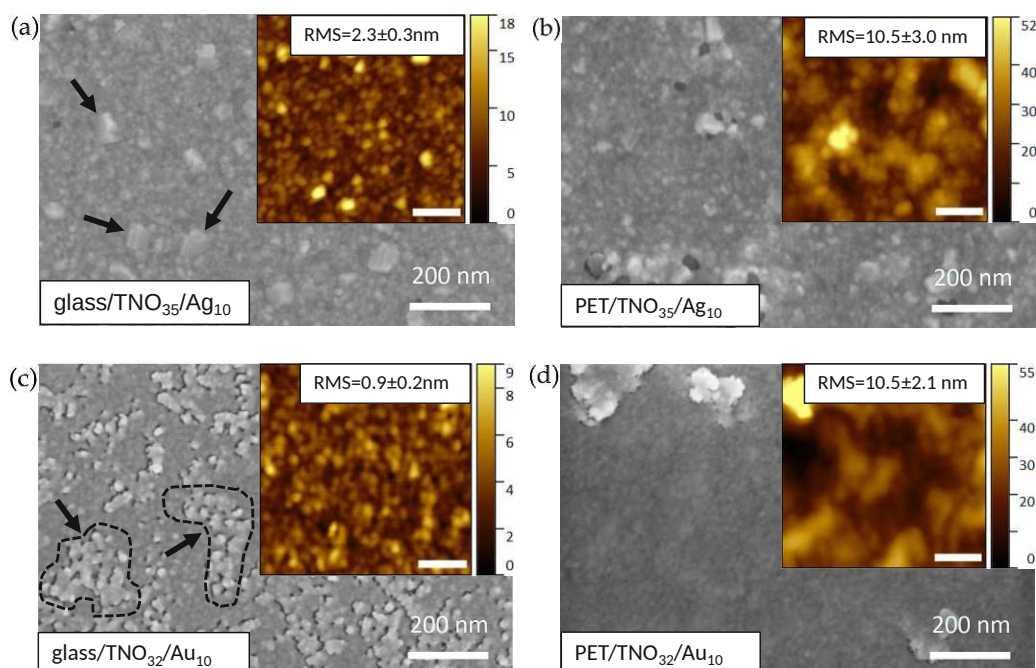
transmittance and reflectance are calculated for the same architecture and added to the graphs. For the TNO<sub>32</sub>/Au<sub>10</sub>/TNO<sub>32</sub> electrodes,  $T_{av} = 0.74$  on glass and 0.69 on PET, respectively, while the sheet resistance is  $8.9 \pm 1.2$  and  $9.2 \pm 0.6 \Omega$ /sq on glass and PET, respectively. Again, the calculated transmittance and reflectance spectra are added to the graphs in Figure 5.6 for comparison. For all electrodes, there is increased absorption in the experimental spectra with respect to the calculated ones, especially at low wavelengths, which leads to reduced values for the average transmittance.

Table 5.1 summarizes the figures for the discussed DMD stacks, including Haacke’s figure of merit [49], which is often used to quantify and compare the performance of transparent electrodes. The figure of merit ( $\Phi$ ) is defined by  $\Phi = T_{av}^{10}/R_s$ . It shows a high value of  $0.01 \Omega^{-1}$  for TNO<sub>35</sub>/Ag<sub>10</sub>/TNO<sub>35</sub> on glass and  $0.0056 \Omega^{-1}$  on PET. With Au, the figure of merit is reduced ( $0.0055 \Omega^{-1}$  and  $0.0027 \Omega^{-1}$  on glass and PET, respectively), but is still in the same range as commercially available ITO on PET (below  $0.003 \Omega^{-1}$ ). It deserves mentioning that an increase of the deposition power for the TNO layer (top and bottom) to 203 W did not change the sheet resistance nor the transmittance of the DMD electrode, which suggests that the metal morphology is not affected by the sputter power of the dielectric in this regime.

The fact that the electrodes with Au have lower figure of merit than the ones with Ag is a known issue which stems from the intrinsic electronic properties of Au. Contrary to Ag, Au and Cu show an increased density of occupied d-states at lower binding energies, leading to stronger absorption of photons in the blue end of the visible spectrum and hence to lower transmittance values in this regime, as compared to Ag [79].

### 5.2.2 Surface morphology, electronic structure and composition

To better understand the optical properties of the electrodes, the metal growth on the base TNO layer was investigated (Figure 5.7 (a)-(d)). Both metals, Ag and Au, show continuous film growth on TNO in the SEM images, only featuring very occasional, small holes. For glass/TNO<sub>32</sub>/Au<sub>10</sub>, groups of grains, delimited by higher contrast regions (such as those marked with arrows in Figure 5.7 (c)) are visible on the surface. Such formations have



**Figure 5.7:** SEM images of (a) glass/TNO<sub>35</sub>/Ag<sub>10</sub>, (b) PET/TNO<sub>35</sub>/Ag<sub>10</sub>, (c) glass/TNO<sub>32</sub>/Au<sub>10</sub> and (d) PET/TNO<sub>32</sub>/Au<sub>10</sub> surfaces. The insets show the corresponding AFM image, including the RMS values. All scale bars are 200 nm.

been also observed for other smooth layers deposited on glass and are thus attributed to the glass substrate. Contrarily, the Ag films show metal clusters on the surface, which drastically modify the underlying substrate-morphology. The root-mean-square (RMS) roughness of the metal layers was extracted from the  $1 \times 1 \mu\text{m}^2$  AFM images shown in the insets of Figure 5.7 (a)-(d). The smoothest film is found for TNO/Au on glass, having an RMS value of 0.9 nm, while the plain glass has RMS of 1.4 nm. The observed roughness is more than doubled for TNO/Ag deposited on glass. On PET, both metal layers exhibit comparable RMS values of 10.5 nm, which is due to the high roughness of the PET foil itself (9.2 nm).

To exclude light scattering as a cause for reduced transmittance, the total transmittance (direct plus diffuse) was measured using an integration sphere. It was found that no diffuse transmittance due to surface roughness is present, since the two curves for direct and total transmittance (Figure 5.8) practically coincide. It may be possible, that localized surface plasmons are excited in the metal grains and holes, leading to discrepancies between the simulated and measured spectra. Also, small deviations in the refractive index can cause such discrepancy.

Figure 5.9 shows  $1 \times 1 \mu\text{m}^2$  AFM images of the DMD electrodes with Ag (top) and Au (bottom) on glass (left) and PET (right), respectively. The lowest RMS roughness with 0.4 nm is found on glass using Au as metallic layer. When using Ag, the RMS increases to 2.5 nm due to the higher roughness of the Ag layer. The RMS is significantly larger for the electrodes on PET, due to the larger substrate roughness. In all cases, it is shown

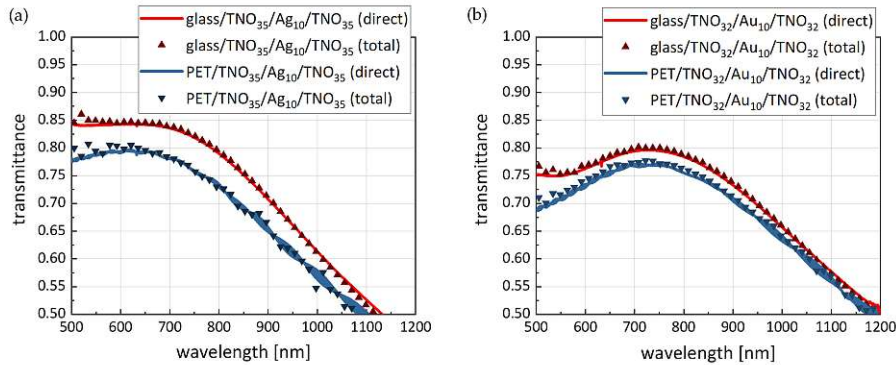


**Figure 5.8:** Transmittance spectra measured using an integration sphere (total transmittance, displayed as triangles) compared to the respective direct transmittance of the discussed DMDs with (a) Ag and (b) Au.

that after the deposition of the top TNO layer, the RMS roughness is decreased, which demonstrates the levelling effect of the sputtered amorphous layer.

The electronic properties of the TNO layers are investigated by XPS and UPS measurements of DMD electrodes. Figure 5.10 (a) shows the XPS spectra for the Ti  $2p$ , Nb  $3d$  and O  $1s$  orbitals. The spectra are fitted with a Gaussian Lorentzian line shape and a Shirley background is used. The position of the Ti  $2p^{3/2}$  and Ti  $2p^{1/2}$  peaks were found at 458.8 eV and 464.5 eV, respectively, which is interpreted as  $Ti^{4+}$  states. The spectrum

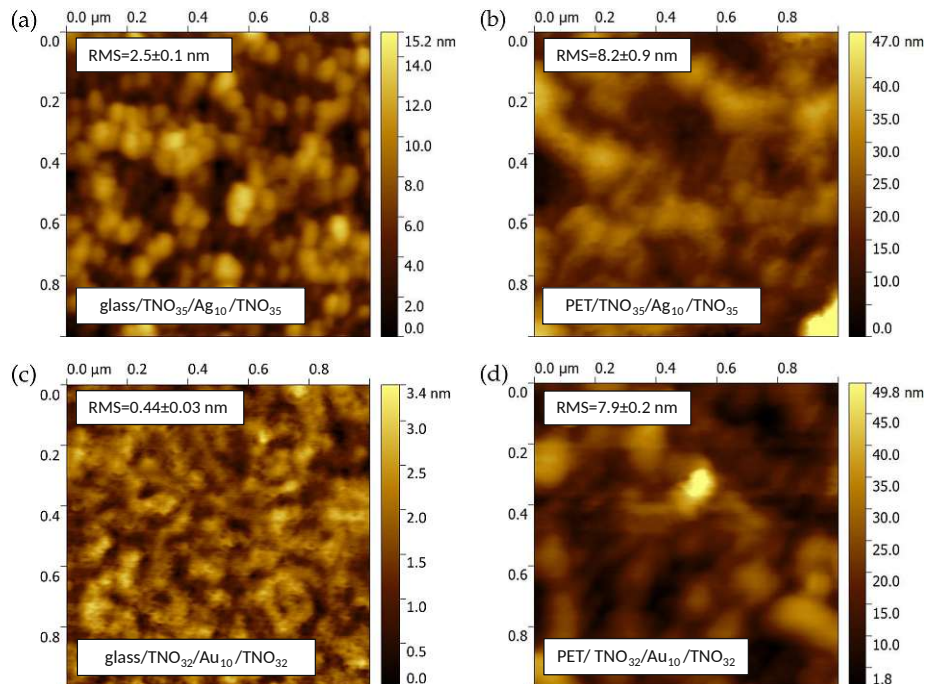


**Figure 5.9:** AFM images of the presented DMD electrodes on glass (left) and PET (right), including the RMS values.

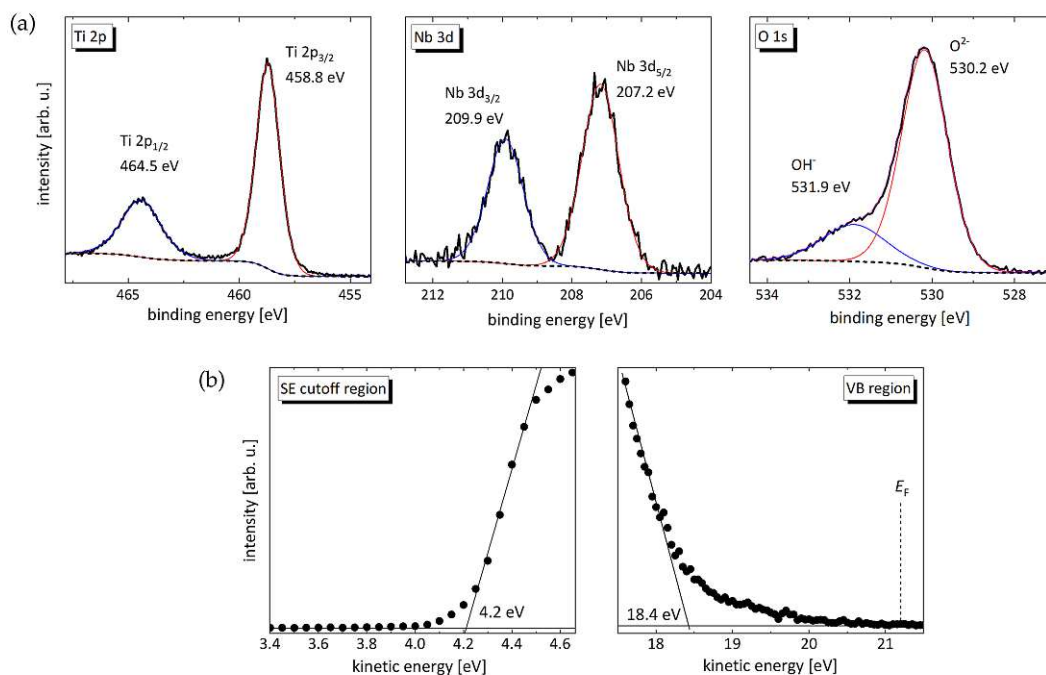


**Figure 5.10:** (a) XPS spectra of Ti 2*p* (left), Nb 3*d* (middle) and O 1*s* (right) regions with binding energy scale. (b) UPS spectrum at the secondary electron cut-off region (left) and valence band region (right); Fermi level is indicated at 0 eV on binding energy scale.

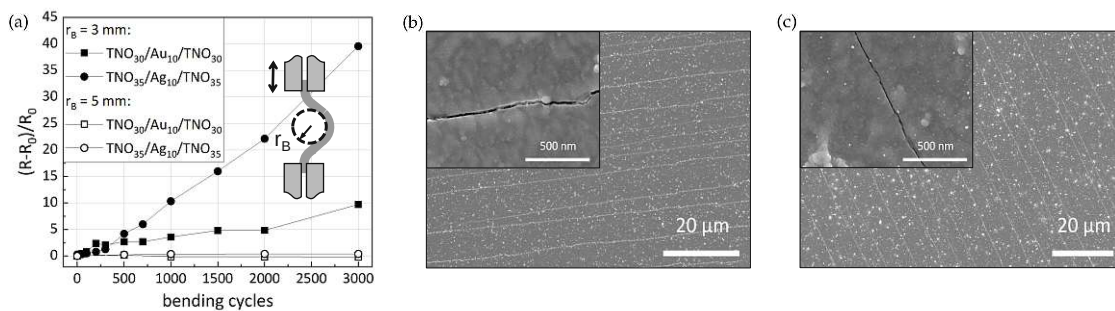
can be fitted consistently with two peaks separated by 5.7 eV, in accordance with the spin-orbit splitting. Also, the peak area ratio of Ti 2*p*<sup>3/2</sup> to Ti 2*p*<sup>1/2</sup> of 2.1 is close to the theoretical value 2:1. This indicates, that there are no oxidation states other than Ti<sup>4+</sup> present at the sample's surface. Analogous, the position of the Nb peaks at 207.2 eV (Nb 3*d*<sup>5/2</sup>) and 209.9 eV (Nb 3*d*<sup>3/2</sup>) imply Nb<sup>5+</sup> states at the sample's surface. The O 1*s* region shows a peak at 530.2 eV, which can be assigned to oxygen bound to a metal and one at 531.9 eV. The last-mentioned peak is probably a result of the contamination by exposure to air, where potentially OH<sup>-</sup> groups are formed at the surface. In case of oxygen, only the peak at 530.2 eV was taken into account for composition calculation. The relative sensitivity factor (RSF) is 2.93 for O 1*s* and 7.81 and 8.21 for the doublets of Ti 2*p* and Nb 3*d*, respectively. Hence, from the peak areas and the RSFs, a Nb/Ti ratio of 9.4% was calculated, yielding a ratio of roughly 3% Nb and 32% Ti in the whole film.

Figure 5.10 (b) shows the UPS results, where the secondary electron cut-off region (SE, left side) and the valence band region (VB, right side) are presented on binding energy scale. Note that the intensity scale is not the same for both regions. The intensity of the SE is by a factor of 20 higher than in the valence band maximum (VBM) region. The secondary electron cut-off edge is found at  $E_{SE-cut-off} = 17.0$  eV (i.e. the work function  $\phi$  is 4.2 eV) and the VBM lies at  $E_{VBM} = 2.8$  eV below the Fermi level  $E_F$ . Further, the ionization energy  $E_{ion}$  can be calculated by subtracting the full spectrum width ( $E_{SE-cut-off} - E_{VBM} = 14.2$  eV) from the incident photon energy (21.2 eV), yielding  $E_{ion} = 7$  eV. This agrees well with the

values above and, thus, charging effects can be excluded. The UPS results correspond to the energy bands of the single TNO layer, as the top TNO is thick enough to exclude contributions of the metal layer. When compared with undoped  $\text{TiO}_2$ , the work function of amorphous TNO is at the lower end of what is reported for undoped  $\text{TiO}_2$  layers exposed to water, namely 4.2 – 5 eV (depending on the texture and oxidation state) [83]. Similarly, the values for  $E_{VBM}$  under the above conditions range from 2.9 eV to 3.4 eV [83], compared to the 2.8 eV extracted for the amorphous TNO layer.

### 5.2.3 Mechanical stability

To quantify the mechanical stability of the electrodes on PET, bending tests are performed, as shown in Figure 5.11 (a). The samples are fixed between two clamps, such that the bending radius  $r_B$  is 3 mm, as sketched in the inset. When the upper clamp is moving, tensile strain  $\epsilon$  is exerted on the thin films, which can be estimated by  $\epsilon = d / (2r_B)$  [55]. Since the thickness  $d$  of the substrate is 175  $\mu\text{m}$ , the estimation yields a strain of 2.9%. Under these conditions, the  $\text{TNO}_{35}/\text{Ag}_{10}/\text{TNO}_{35}$  stack shows a 40-fold increase of the initial resistance, while the relative resistance of  $\text{TNO}_{30}/\text{Au}_{10}/\text{TNO}_{30}$  increases only by a factor of 10 after 3000 bending cycles. The difference is not immediately clear, as both samples exhibit continuous cracks in the SEM images (Figure 5.11 (b), (c)) which extend at least for several hundred  $\mu\text{m}$ . The higher ductility of Au may be responsible for the significantly larger resistance increase for  $\text{TNO}_{35}/\text{Ag}_{10}/\text{TNO}_{35}$  for >500 bending cycles. Oppositely to ITO, where broad cracks dramatically increase the relative resistance within few bending cycles [33], the current flow in the DMDs is not fully hampered, as the cracks remain narrow and the ductile metal layer partly stays intact throughout the crack. A strong relaxation effect of the resistance was observed after un-clamping the sample from the bending test-stand, with the resistance decreasing to less than half of its initial value in the course of some minutes. This is attributed to the pronounced deformation



**Figure 5.11:** (a) Resistance relative to the initial value  $R_0$  as a function of the number of bending cycles. (b), (c) SEM images of the  $\text{TNO}_{30}/\text{Au}_{10}/\text{TNO}_{30}$  and  $\text{TNO}_{35}/\text{Ag}_{10}/\text{TNO}_{35}$  surfaces, respectively, after 3000 bending cycles at  $r_B = 3 \text{ mm}$ .

of the PET substrates due to the small bending radius. When removed from the clamps, the substrate partially relaxes over time and relieves strain from the DMD. The residual resistance increase is associated with the plastic deformation of the substrate, which exerts constant strain on the film. As soon as the sample is fully straightened, i.e. forced back to its initial shape, the resistance drops to a relative resistance increase of a factor of approx. 5 in the case of Au and a factor of approx. 10 in the case of Ag. It is expected that the use of a thinner, more elastic substrate would lead to a smaller increase of the resistance, as reported by Li et al.[96]. Similarly, when exerting a larger bending radius of  $r_B = 5$  mm, the substrate does not experience remaining deformation and the observed increase of relative resistance was negligible ( $< 1$ ) (Figure 5.11 (a)). Furthermore, after 3000 cycles at a bending radius of 5 mm, the DMDs show only very fine cracks, which are barely visible in the SEM images.

### 5.3 MESOPOROUS TITANIUM OXIDE

The use of a mesoporous  $\text{TiO}_2$  (mp- $\text{TiO}_2$ ) scaffold layer is a common electron extraction layer in perovskite solar cells to promote perovskite crystallization, charge extraction and device stability [106, 107, 108]. The drawback of the mp- $\text{TiO}_2$  layer is the often required high-temperature sintering step (above  $400^\circ\text{C}$ ), necessary for layer crystallization and uniformity, as well as for good adhesion properties and defect-free interfaces [109]. The requirement of high-temperatures has hampered the use of a mesoporous n-i-p architecture on flexible substrates. To overcome this issue, several alternative treatments have been suggested to replace the high temperature sintering step, ranging from UV/ozone [110, 111, 112] and plasma treatments [113], to photonic flash sintering [114, 115]. These procedures are often time-consuming and/or require additional, elaborate preparation steps. A few studies use binder-free  $\text{TiO}_2$  pastes, which allow a sinter-free process using only a drying step ( $\sim 150^\circ\text{C}$ ) to promote interparticle connectivity via dehydration reactions [116, 117, 118]. In any case, these scaffold layers are usually combined with an additional compact  $\text{TiO}_2$  layer, to reduce carrier recombination at the interface with the transparent electrode [108, 111]. In this section, the properties of the TNO-based DMDs combined with a low-temperature processed mp- $\text{TiO}_2$  layer are presented, where the compact  $\text{TiO}_2$  layer is already integrated in the transparent electrode. The mesoporous  $\text{TiO}_2$  layer was spin-coated on the sputtered electrodes using a commercial Ti-Nanoxide ink (HT-L/SC from Solaronix®). An approximately 180 nm-thick layer was obtained when spinning statically at 4000 rpm for 30 s, followed by drying on a hotplate, in ambient atmosphere, at  $100^\circ\text{C}$  for 30 min.

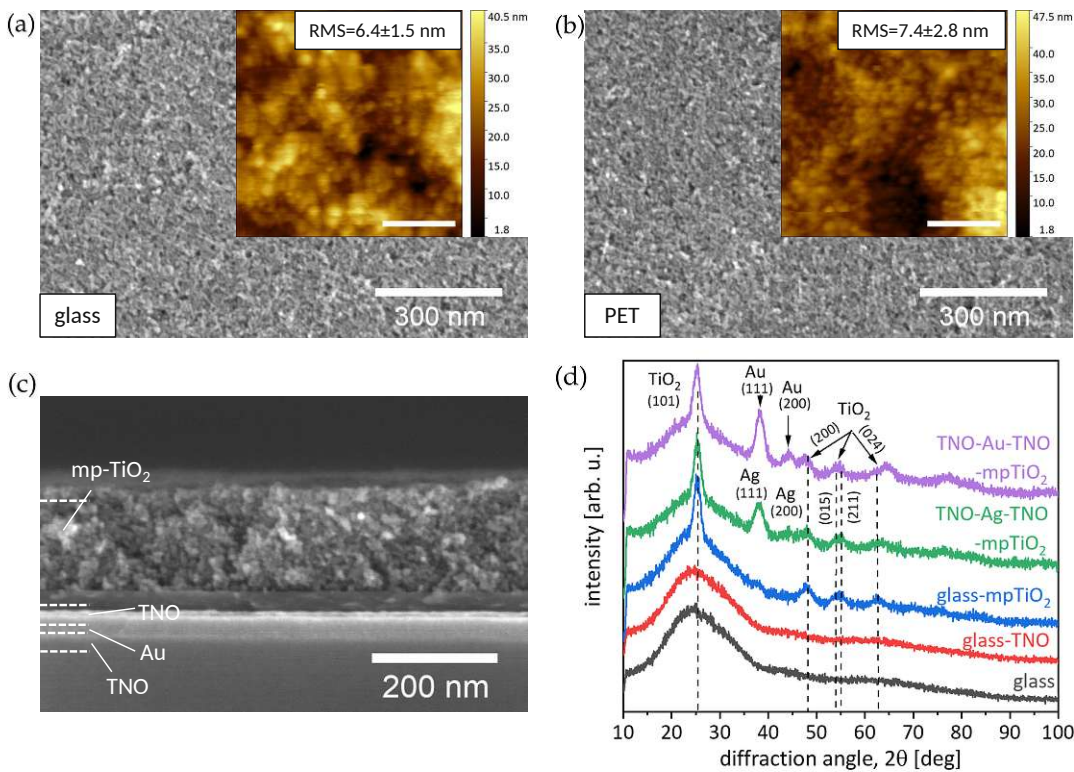


**Figure 5.12:** SEM and AFM images of the mp-TiO<sub>2</sub> surface deposited on the DMD on (a) glass and (b) PET and in (c) the corresponding SEM cross section image on glass. (d) XRD diffractogram of plain glass (black), TNO on glass (red), mp-TiO<sub>2</sub> on plain glass (blue) and on the DMD with Ag (green) and Au (purple).

The deposited mp-TiO<sub>2</sub> on the DMD is shown in Figure 5.12, where a porous surface is visible in the SEM images, irrespective of the underlying substrate. The insets of Figure 5.12 (a) and (b) present the corresponding  $1 \times 1 \mu\text{m}^2$  AFM images, yielding RMS roughness of 6.4 nm on glass and 7.4 nm on PET. The surface roughness is now governed by the pores and particles constituting the scaffold layer, rather than the substrate itself. This way, the long-range roughness of the PET surface is evened out by the mesoporous layer. In Figure 5.12 (c), a cross section SEM image of the DMD on glass with the mp-TiO<sub>2</sub> on top, is shown. The metal layer (in this case Au) is clearly distinguishable from the adjacent, compact TNO layers (that the upper TNO layer appears darker stems from a small distance difference due to the uneven cleavage of the sample). The mp-TiO<sub>2</sub> layer is shown to cover the substrate in a homogenous manner, yielding a thickness of  $175 \pm 15$  nm. An increased layer thickness was tested by repeating the deposition process, which resulted in a similarly homogeneous layer with double the thickness.

As the ink is composed of dispersed anatase nanoparticles, the XRD investigation (Figure 5.12 (d)) of the mp-TiO<sub>2</sub> layer deposited on glass (in blue) shows distinct peaks of a TiO<sub>2</sub> anatase (tetragonal) phase. The (101) peak at  $25.5^\circ$  is most pronounced but also peaks at higher diffraction angles can be assigned to nanocrystalline anatase (COD ID: 1526931)



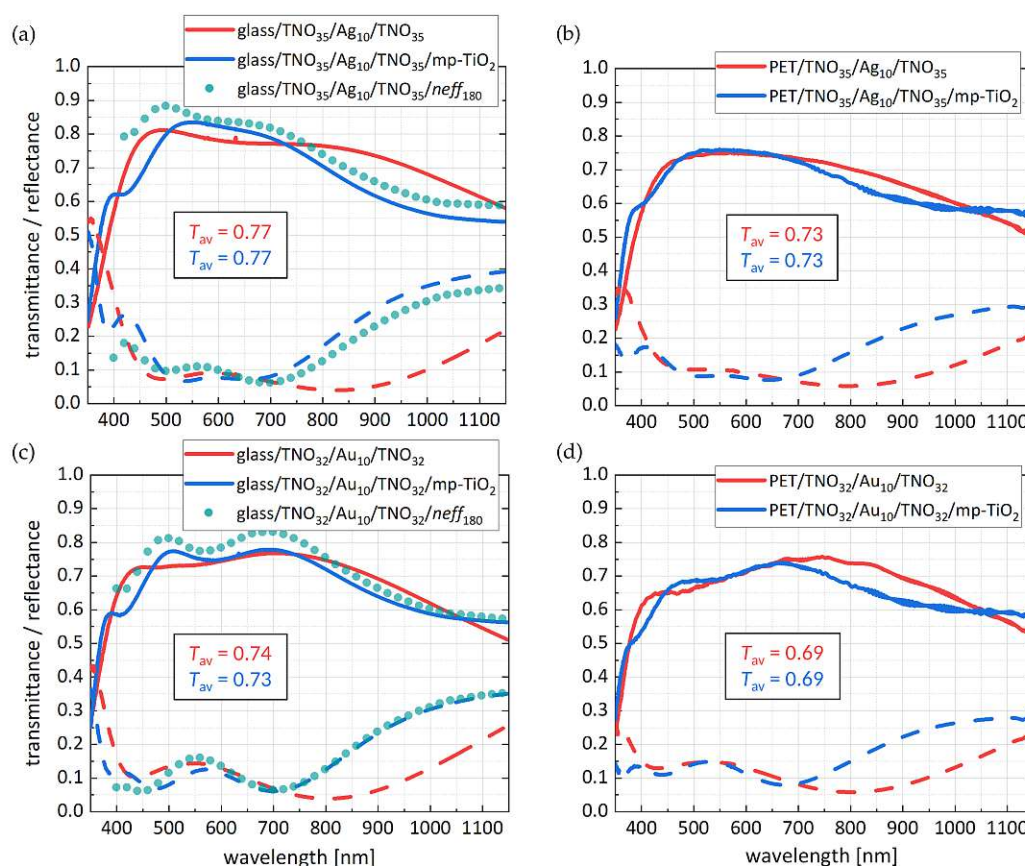


**Figure 5.13:** (a)-(d) Transmittance (solid lines) and reflectance (dashed lines) spectra of the DMD electrodes without (red) and with mp-TiO<sub>2</sub> (blue) layer. (a) and (c) include the simulated spectra for an effective medium  $n_{eff}$  on top of the DMDs.

[119]. Figure 5.12 (d) also includes the diffraction pattern of a single TNO layer on glass (in red), showing its amorphous character, as there is no difference to the plain glass substrate. Furthermore, the pattern of mp-TiO<sub>2</sub> deposited on the DMD electrodes (in green and purple) was added to the Figure, where the additional peak comes from the (111) phase of the corresponding metal (COD IDs: 9011607 (Ag), 9011613 (Au)) [120].

Transmittance and reflectance spectra of the DMDs, with and without the mp-TiO<sub>2</sub> layer, are displayed in Figure 5.13. The comparison shows that the mp-TiO<sub>2</sub> is a highly transparent material, which practically does not alter the average transmittance (values in the insets), nor the visible reflectance of the electrodes. The most significant change can be seen in the near infra-red above 800 nm, where the reflectance is significantly increased by the scaffold layer. In order to explain this effect, a simple model was composed to extract the optical properties, i.e. the refractive index of the mp-TiO<sub>2</sub>. Using the same TMM calculations (for more details see 8.1.3) as for the DMD spectra in Figures 5.5, the DMD stack with an additional material on top was simulated and compared to the experimental spectra. Since the mp-TiO<sub>2</sub> encloses air, a compact TiO<sub>2</sub> layer with high

refractive index is not representative. Therefore, a thick (180 nm) effective medium with an effective refractive index ( $n_{eff}$ ) is introduced (according to the Bruggeman effective medium approximation) [105].  $n_{eff}$  assumes values between 1.8 and 1.6, significantly reduced with respect to compact  $\text{TiO}_2$ . Comparing simulated and experimental spectra (Figure 5.13 (a) and (c)), a decent agreement is obtained.

#### 5.4 SUMMARY

This chapter reports on sputtered niobium-doped titanium oxide, which could be deposited from a conductive oxide target in DC magnetron mode. Transparent films are achieved even in inert Ar atmosphere, thus allowing for increased deposition rates up to 16.8 nm/min. Having a wide band gap of 3.3 eV and high refractive index above 2.3, the TNO is used in TNO/(Ag or Au)/TNO stacks as transparent electrodes on glass and PET. All DMDs feature transmittance above 0.7 and sheet resistance below  $10 \Omega/\text{sq}$ . Especially, the mechanical stability of the flexible electrodes on PET makes them a superior alternative to the common ITO on PET. It was shown, that the combination of these DMD electrodes with a mesoporous  $\text{TiO}_2$  layer could serve as efficient electron transport layer for flexible optoelectronic devices. To avoid thermal damage of the PET substrate, the process temperature of the mesoporous  $\text{TiO}_2$  was reduced to  $100^\circ\text{C}$ , resulting in a uniform scaffold oxide layer.

---

## DEVICES

---

To prove the applicability of the electrodes presented in the previous chapters, they are implemented in solar cells and OLEDs. In both cases, the idea was to simultaneously use the DMD stacks as transparent electrode and as charge carrier transport layer. The focus lies especially on the performance of the DMD electrodes on PET to produce flexible devices, where the ITO lacks mechanical stability.

However, it should be noted at this point, that all devices only act as proof of principle, where further optimization would be required to achieve high-efficiency devices, which is out of the scope of this thesis. The detailed materials and methods of the device fabrication are described in the Appendix (8.1).

### 6.1 PEROVSKITE SOLAR CELLS

Perovskite solar cells are one of the most studied photovoltaic technologies due to their ease of fabrication, promising efficiencies and compatibility with flexible substrates. "Perovskite" refers to the crystal structure of the absorber material in the solar cells. It is based on organic-inorganic hybrid material, typically methylammonium lead iodide ( $\text{CH}_3\text{NH}_3\text{PbI}_3$  or MAPbI) [121]. The iodine is often (partially) replaced by other halide atoms like Cl or Br. Recently, lead-free perovskites are investigated which are based on Sn, Ge, Sb or Bi. [122, 7]. Other formulations include formamidinium (FA) or are fully inorganic using Cs or Pb as cations [123].

In addition to the different materials, there are also several possible device architectures depending on the layer sequence: the planar n-i-p or p-i-n (inverted) configuration, or the mesoporous (or mesoscopic) structure, where oxide nanoparticles act as scaffold layer for the perovskite [1, 123]. An even broader variety is reported for the charge selective layers, including various organic and oxide materials. For flexible applications, the substrate and transparent electrode are critical bottlenecks for achieving high efficiency and flexibility [2].

6.1.1 *p-i-n structure using MTO*

To test the performance of the MTO/metal/MTO electrodes, they are implemented in prototype perovskite solar cells on both, glass and PET substrates. Since the idea was that the MTO can simultaneously act as hole-extraction layer, the devices are prepared in the inverted (*p-i-n*) structure with and without PEDOT:PSS as an additional hole transport layer. In this architecture, ZnO nanoparticles (ZNO-NPs) are used as an electron transport layer on top of the perovskite (see Figure 6.1 (a)) and Ag is evaporated through a shadow mask as back electrode. It should be noted at this point, that both electrode designs, using Ag and Au, were tested in our experiments. However, Ag-containing electrodes degraded quickly when the perovskite was deposited, with the electrode resistance increasing to several  $k\Omega$  approximately a day after the device fabrication. This effect has been reported before and is explained by the formation of silver-iodide species, depleting the conductive Ag layer [124, 125, 126]. Therefore, any working devices were only achieved when using Au as metal in the DMD electrode.

Figure 6.1 (b) shows the XRD pattern of the solar cells (excluding the back Ag electrode) with and without the PEDOT:PSS, indicating a well-crystallised perovskite (beta-methylammonium lead triiodide structure, COD ID: 4335638) in both cases. However, when looking at the current-voltage (*J-V*) curves in Figure 6.1 (c), one can see a significant improvement in performance when the additional PEDOT:PSS is used. Without PEDOT:PSS, the fill factor and the efficiency are very small with 30% and 0.5%, respectively. From the *J-V* characteristic a high series resistance and low shunt resistance is evident, yielding a small short circuit current ( $j_{SC}$ ) of  $4.9 \text{ mA/cm}^2$  and open-circuit voltage ( $V_{OC}$ ) of 400 mV. In contrast, the best-working devices on glass using PEDOT:PSS yield an efficiency of 6.4%. With a  $V_{OC}$  of 890 mV and a  $j_{SC}$  of  $13.9 \text{ mA/cm}^2$ , the main drawback is the low fill factor caused by parasitic resistances. Especially the series resistance (derived by the small slope at the  $V_{OC}$ ) is very high, which may be related with the design of the top contacts. Since they are evaporated through a shadow mask with a very narrow gap,

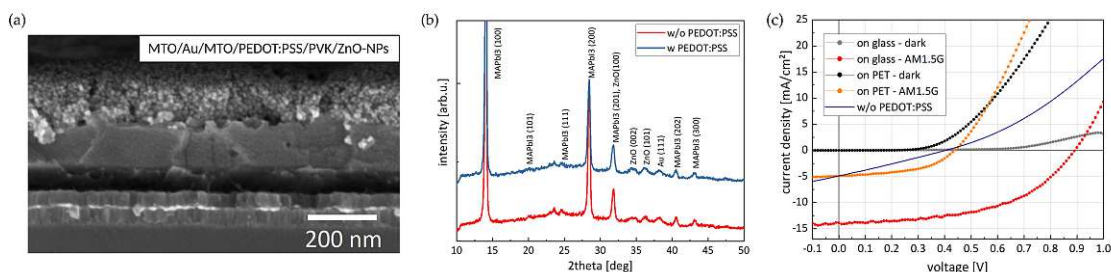


**Figure 6.1:** (a) SEM cross section image of a perovskite solar cell on glass (excluding the Ag back electrode). (b) XRD pattern of the perovskite solar cell on glass with (blue) and without (red) PEDOT:PSS. (c) *J-V* characterisation of the devices on glass and PET substrates, in dark and illuminated (AM1.5G) conditions.

they sometimes had increased resistance when the evaporated metal layer was too thin or defective. In terms of energy alignment of the hole extraction layer, it is not immediately obvious why the solar cells with PEDOT:PSS show significantly higher efficiency, since both, MTO and PEDOT:PSS, have the same work function of 5.1 eV. However, PEDOT:PSS is electrically conductive, while the 40 nm of MTO in the DMD is rather insulating, possibly causing a smaller current density. Additionally, oxygen defects which are present in the MTO, may also induce more recombination.

Figure 6.1 (c) also presents the best-performing solar cell on PET substrate with a  $V_{OC}$  of 720 mV and a  $j_{SC}$  of 11.2 mA/cm<sup>2</sup>, yielding a maximum efficiency of 2.1%. The roughness and water permeability of the PET substrates is a general challenge for flexible devices and probably causes the decrease in solar cell performance. Improvement is expected when introducing a polymer interlayer to smooth the substrate surface of PET [31].

### 6.1.2 mesoporous n-i-p structure using TNO

*The following section is part of the published article:*

Goetz, S. et al. *Low-Temperature-Processed Transparent Electrodes Based on Compact and Mesoporous Titanium Oxide Layers for Flexible Perovskite Solar Cells*. *ACS Applied Energy Materials*. (2021). [89], reproduced under the corresponding copyright agreement (8.2).

The developed electrodes based on Nb-doped TiO<sub>2</sub> (TNO, see chapter 5) incorporating the mp-TiO<sub>2</sub> layer, were implemented in mesoporous n-i-p perovskite solar cells. Figure 6.2 (a) shows a cross-section SEM image of a freshly cleaved device on glass, before the evaporation of the Au electrode. A continuous, ~300 nm-thick perovskite (PVK) layer covers the mp-TiO<sub>2</sub> layer. It should be pointed out, that the formation of a continuous, crystalline and pinhole-free perovskite layer was achieved reproducibly and with less effort on the mesoporous layer as compared to the planar DMD electrode. The dark spiro-OMeTAD hole transport layer is distinguished on top of the PVK. A top view SEM image of the PVK layer (without the spiro-OMeTAD) on PET is presented in the inset of Figure 6.2 (a), showing densely-packed grains. The XRD pattern of the whole device on glass, shown in Figure 6.2 (b), confirms full crystallisation of the perovskite (peaks marked with an asterisk in the diffractogram using beta-methylammonium lead triiodide structure reference, COD ID: 4335638), since no peaks of unreacted products can be found. The Au reflections come from the evaporated back electrodes, also visible on the photograph in the inset, and one peak is assigned to the anatase phase of the mp-TiO<sub>2</sub> layer. The XRD results are only shown for the device on glass, since the strong characteristic peak of the PET substrate superposes the diffraction peaks of the thin films and hampers the identification of smaller peaks. However, the perovskite deposition

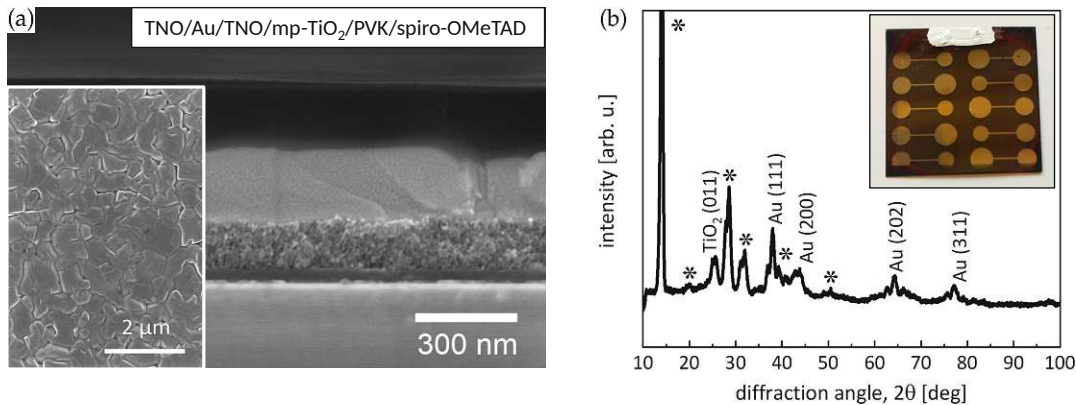


**Figure 6.2:** (a) SEM cross section image of a perovskite solar cell on glass (excluding the Au back electrode). The inset shows the top view of a perovskite layer deposited on PET/TNO/Au/TNO/mp-TiO<sub>2</sub>. (b) XRD pattern of a perovskite solar cell on glass. The inset shows a photograph of the corresponding device on PET.

followed the same procedures and heat treatment for both substrates, and we expect the same degree of crystallization on PET as on glass.

Again, both electrode designs, using Ag and Au, were tested in our experiments but the Ag-containing electrodes degraded quickly when the perovskite was deposited (as described in 6.1.1). This is contrary to recent reports on flexible perovskite solar cells with similar DMD architecture using TiO<sub>2</sub>/Ag/TiO<sub>2</sub> electrodes [95, 96] - however, a different interlayer (namely ZnO and CPTA) between the transparent electrode and the PVK or a different morphology of the TiO<sub>2</sub> itself may have prevented diffusion in this case. Additionally, other PVK formulations without iodine, especially wide band gap PVK absorbers based on Br could be the key to improve the stability of Ag-based DMDs. Indeed, in a recent study, it was demonstrated that Br-based perovskites slow-down the degradation of Ag, paving the way for stable Ag-based electrodes [127]. Such an I-free absorber, combined with a TiO<sub>2</sub>-based buffer, could be a promising combination against Ag degradation.

Dark and illuminated (AM1.5G) current density-voltage (J-V) curves of solar cells on PET and glass, both with an active area of 3.14 mm<sup>2</sup> are displayed in Figure 6.3 (c). Only a small hysteresis between forward and reverse IV directions is observed. While some hysteresis is common in most PVK solar cells, the origin of this delay between the change of properties and the external stimulation is still under debate [128]. The cells on PET yielded an open-circuit voltage ( $V_{OC}$ ) of 995 mV, a short-circuit current density ( $j_{SC}$ ) of 13.9 mA/cm<sup>2</sup> and a fill factor (FF) of 58.0% when scanned from 1.2 V to -0.1 V, and a  $V_{OC}$  of 981 mV,  $j_{SC}$  of 13.9 mA/cm<sup>2</sup> and FF of 58.7% for the reverse scanning direction. On glass, the cell performance was comparable, with a  $V_{OC}$  of 1.01 V, a short-circuit current density  $j_{SC}$  of 13.7 mA/cm<sup>2</sup> and a FF of 57.4% when scanned from 1.2 V to -0.1 V, and a  $V_{OC}$  of

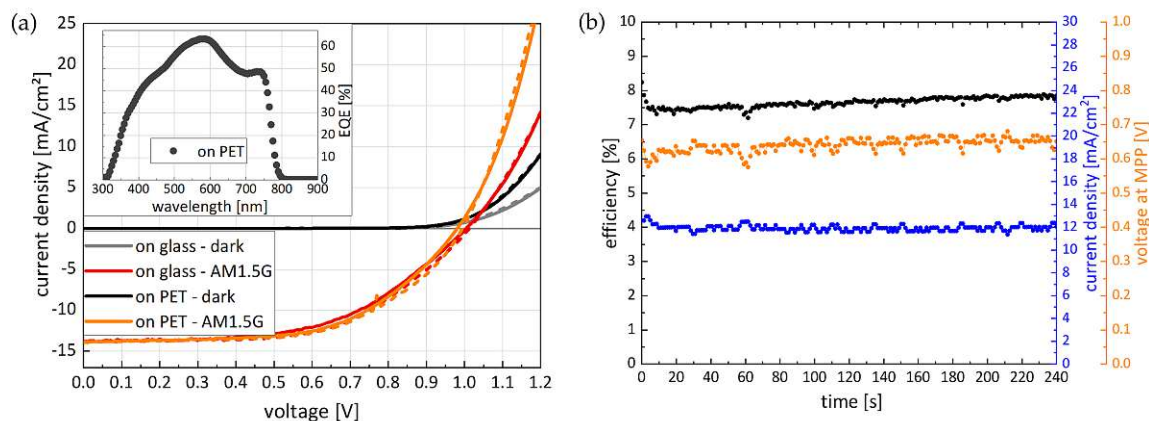


**Figure 6.3:** (a) J-V curves of solar cells on PET and glass, in dark and illuminated (AM1.5G) conditions. The solid lines represent the forward scanning direction and the dashed lines the corresponding reverse scanning direction. The inset shows an EQE measurement of a cell on PET (b) Efficiency measurements at the maximum power point (MPP) over time for a cell on PET.

1.0 V,  $j_{SC}$  of 13.8 mA/cm<sup>2</sup> and FF of 57.4% for the reverse scanning direction. Additionally, measurements at the MPP for the solar cell on PET yielded only small variations over a time of 4 minutes (Figure 6.3 (d)). The power conversion efficiencies (PCE) derived from the IV-curves are 8.01% for the cell on PET and 7.93% on glass. Considering that the used perovskite ink generally reports an efficiency close to 12% on glass/ITO [129], the results are promising but still leave room for improvement. Again, the losses are mainly due to the low fill factor caused by a high series resistance. As mentioned in 6.1.1 this is related to resistive top contacts and was improved in a subsequent experiment yielding an increased efficiency of 9.4% on PET with concomitant increase of the  $j_{SC}$ . Otherwise, further improvement of the solar cell performance may be possible by reducing the thickness of the mp-TiO<sub>2</sub> layer and by detailed interface optimization.

## 6.2 ORGANIC LIGHT-EMITTING DIODES (OLEDs)

Although the technology of organic light-emitting diodes (OLEDs) has already reached the market in screens and displays, the research is still ongoing. The aim is to move towards flexible devices and large-area fabrication. To this end the ITO, being the dominant transparent electrode, has to be replaced to reduce production costs and to prevent electrode failure under bending. In contrast, many of the light-emitting polymers are compatible with flexible and (semi)transparent applications as well as large-scale fabrication techniques as most of them are solution-processable. In the following, the PDY-123 copolymer "Super Yellow" (SY) is employed as active layer, yielding OLEDs emitting in the yellow wavelength range. Subsequently, the DMD electrodes from the previous

chapters are implemented in OLEDs, resulting in both architectures, n-i-p (using TNO) and p-i-n (using MTO).

### 6.2.1 mesoporous n-i-p architecture using TNO

The mesoporous configuration using mp-TiO<sub>2</sub>, which is common for perovskite solar cells (section 6.1.2) has - to my knowledge - not been applied to OLEDs yet. Therefore, the TNO/Ag/TNO/mp-TiO<sub>2</sub> electrodes from section 5.2 were implemented in prototype OLEDs. In contrast to the perovskite solar cells, Ag can be used as metal layer, since no reactions with the active material are observed. Generally, the application of TiO<sub>2</sub> in OLEDs usually suffers from efficiency losses due to interfacial defects and insufficient electron injection without suitable interface functionalization [130].

In order to obtain working devices, the mp-TiO<sub>2</sub> layer thickness had to be reduced by diluting the commercial Ti-Nanoxide ink (HT-L/SC from Solaronix®) with ethanol in a 1:4 volume ratio, resulting in continuous layers of approx. 60 nm when spin coated at 4000 rpm for 30 s. Afterwards, a polyethyleneimine (PEI) solution was spin coated to functionalise the TiO<sub>2</sub>, lowering the work function of metal oxides and, thus, improving the energy level alignment with the organic emitter [131, 132]. A schematic of the energy band structures of each layer is presented in Figure 6.4. The boxes are aligned by the vacuum level and represent the band gap energy, limited by the valence band maximum on the bottom and the conduction band on the top. The expected influence of the PEI on TiO<sub>2</sub> is shown by the arrow, moving the work function of TiO<sub>2</sub> Anatase to smaller values [132]. Similarly, the work function of the evaporated MoO<sub>3</sub> is estimated from literature values but as the reported values vary strongly between 4.7 and 6.9 eV, a broader range is considered here. Figure 6.5 (c) shows a cross section SEM image of the final device architecture TNO/Ag/TNO/mp-TiO<sub>2</sub>/PEI/SY/MoO<sub>3</sub>/Au (for fabrication details see 8.1.1). It is noted at this point, that the PET substrate was coated with PMMA to

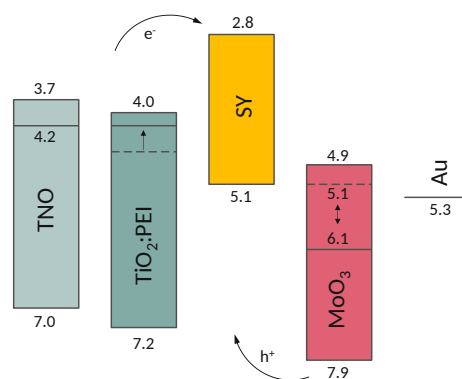


**Figure 6.4:** Schematic representation of the energy band alignment for the n-i-p structure.



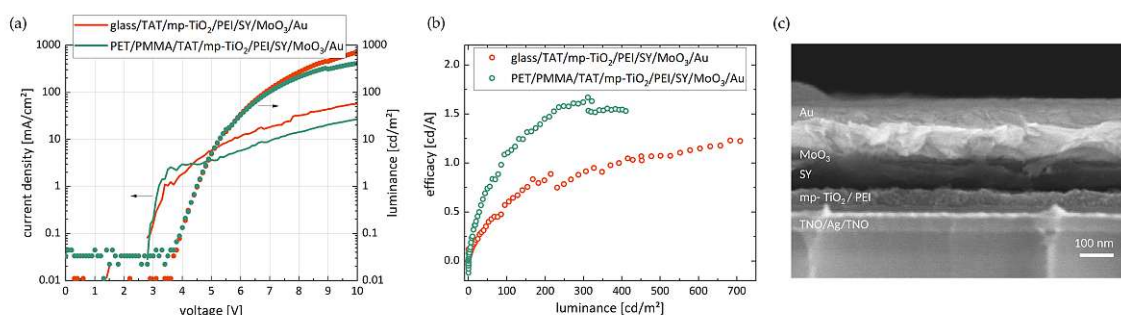


**Figure 6.5:** (a) J-V characterization and simultaneous luminance measurement of the best element achieved for TNO/Ag/TNO/mp-TiO<sub>2</sub>/PEI/SY/MoO<sub>3</sub>/Au on glass and PET/PMMA substrate. (b) Corresponding current efficacy [cd/A] as a function of the luminance. (c) SEM cross section image of the whole device on glass.

reduce the RMS surface roughness of the substrate from around 9 nm down to 4 nm [31]. The current density-voltage (J-V) curves and simultaneous luminance measurements of the best devices on glass and PET, respectively, are shown in Figure 6.5 (a). Irrespective of the substrate, both devices show small current densities, below 100 mA/cm<sup>2</sup>, which could suggest, that the TiO<sub>2</sub> layer is blocking charge carriers due to the insulating character. Also, the turn-on voltage (where the luminance is 1 cd/m<sup>2</sup>) is rather high at 4.5 V, such that the maximum luminance is only reached at an applied bias of 10 V. This is another indication for poor charge injection, as high voltage is required to produce sufficient charge recombinations for light emission. However, the working principle of the implemented architecture is demonstrated when considering the current efficacy shown in Figure 6.5 (b). Especially on the PET substrates, the efficacy yields promising results for flexible OLEDs, achieving higher efficacy than on glass. It is expected that with further optimization of the interfaces, layer thicknesses and optical properties, the performance can be significantly increased.

### 6.2.2 *p-i-n* architecture using MTO

To show the applicability of MTO, prototype organic LEDs (OLEDs) are fabricated using MTO-based transparent electrodes (described in 3.2, denoted here as MAM). With MTO having a work function of 5 eV, the energy level alignment should be suitable for hole injection to the Super Yellow (SY) polymer with a HOMO of 5.1 eV, similar to what has been shown for MoO<sub>3</sub>. However, other effects like interfacial defects and interface reactions also influence the charge injection efficiency [12]. Therefore, PEDOT:PSS was required as additional hole transport layer, resulting in the following device architecture: MTO/Ag/MTO/PEDOT:PSS/SY/ZnO-NPs:PEI/Al.

Figure 6.6 schematically presents the energy band structure of the device. The values for

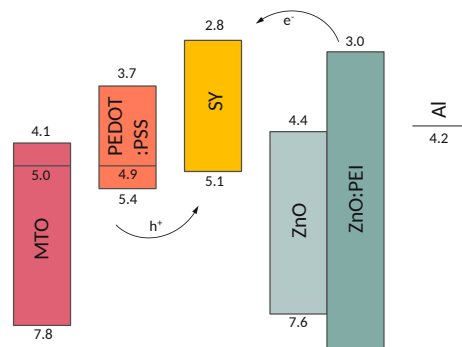


**Figure 6.6:** Schematic representation of the energy band alignment for the p-i-n structure.

PEDOT:PSS and ZnO:PEI are taken from literature [133, 131]. While the work function of MTO and PEDOT:PSS is basically the same, their band structure is different. However, the low lying valence band of MTO should be energetically suitable for hole injection (as known from pure  $\text{MoO}_3$  [134]), supporting the assumption of interface defects preventing the efficient hole transfer from MTO to the SY. On the other side, the effect of PEI is shown in direct comparison to ZnO, demonstrating a significant decrease of the work function and improving the alignment of the conduction band of ZnO with the LUMO of SY.

The same device configuration is fabricated on a commercial ITO electrode for reference. Figure 6.7 (a) shows the J-V curves and luminance values of the best devices in each electrode configuration on rigid (glass) substrates. The performance of both electrodes is comparable, with a turn-on voltage (where the luminance is  $1 \text{ cd/m}^2$ ) of 2.2 V for ITO and 2.4 V for MTO and with a maximum luminance well above  $10000 \text{ cd/m}^2$ . For both electrodes, PEDOT:PSS was necessary to achieve performing devices. It is important to underline that the use of MTO instead of  $\text{MoO}_3$  permits device processing with the water-based PEDOT:PSS, as  $\text{MoO}_3$  completely dissolves upon PH1000 application.

However, from preliminary tests we expect that with careful interface engineering of the MTO/SY interface as well as device-specific optimization of the MTO electrode, the use of PEDOT:PSS can be avoided.

As a further step, the MTO/Ag/MTO electrode is used to make flexible OLEDs, using the same architecture on PET substrates. Again, a commercial ITO-coated PET-foil is used as reference. The J-V and luminance characterization of the best performing devices are shown in Figure 6.7 (b). Again, the performance is very similar to the ones on glass, but with the lack of heat dissipation on the thin plastic foil leading to significant degradation above 5.5 V, a strong kink in the luminance curve is visible. With this, the maximum luminance on the MTO/Ag/MTO electrode is found at  $3960 \text{ cd/m}^2$  but with a low turn-on voltage of 2 V. When looking at the current efficacy (Figure 6.7 (c), (d)), the flexible devices show even higher efficacy than the ones on glass. Although the devices on MTO/Ag/MTO have approx half the efficacy of ITO, the MTO/Ag/MTO electrode has the clear advantage of high mechanical stability under bending compared to the common

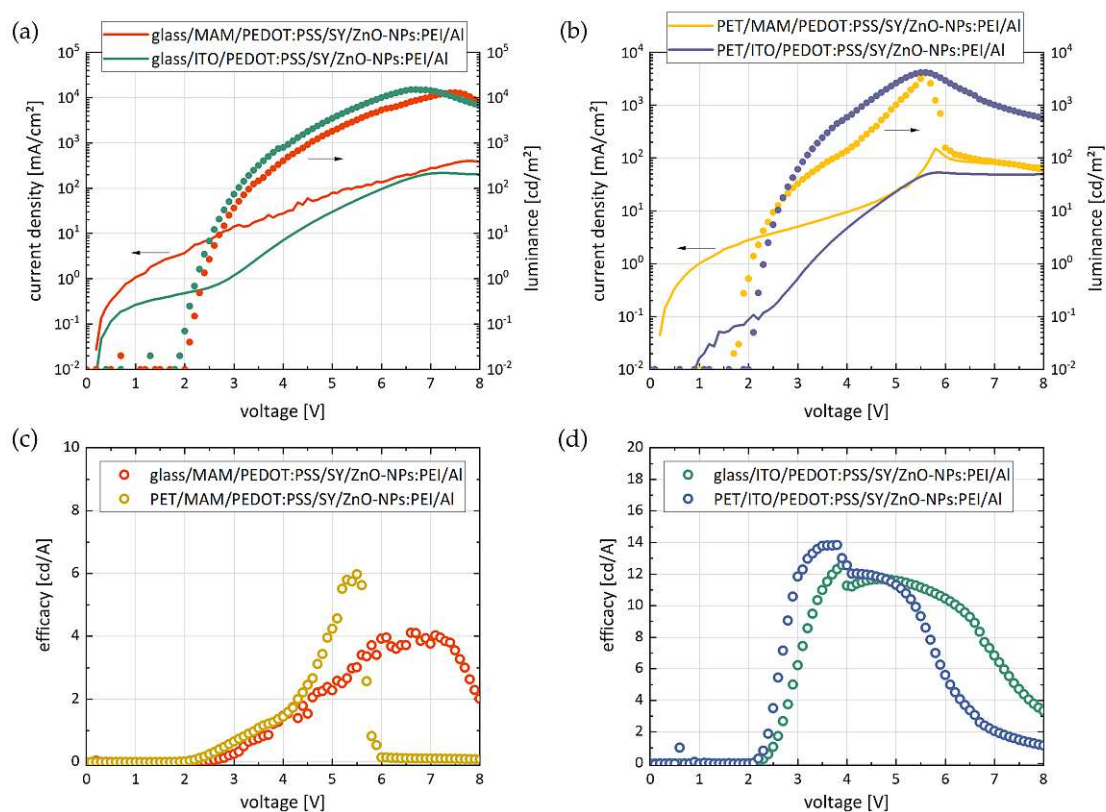


**Figure 6.7:** J-V characterization and simultaneous luminance measurement of the best elements achieved for PEDOT:PSS/SY/ZnO-NPs:PEI/Al on (a) glass/MTO-Ag-MTO(MAM) and glass/ITO, (b) PET/MTO-Ag-MTO(MAM) and PET/ITO. (c), (d) Corresponding current efficacy [cd/A] as a function of the applied voltage.

ITO (see 3.2). Furthermore, a maximal efficacy of 6 cd/A is a successfully high values when compared to other ITO-free OLEDs in recent publications [135, 134].

### 6.3 SUMMARY

In this chapter, the developed DMD electrodes were implemented in perovskite solar cells and organic LEDs to test their device-specific performance as transparent electrodes and charge transport components. While the TNO/metal/TNO/mp-TiO<sub>2</sub> electrodes yielded efficient perovskite solar cells (with up to 9% power conversion efficiency) in the designated configuration, the MTO-based electrodes required an additional PEDOT:PSS layer to achieve working devices. Nevertheless, they suffered from low fill factor due to high parasitic resistance within the device. For the OLEDs, the TNO-based electrodes were modified using thinner TiO<sub>2</sub> layers and PEI-functionalization to obtain light emission. However, more optimization is necessary to improve the efficiency of the devices in this configuration. The inverted OLED structure was realized with the MTO/Ag/MTO

electrodes. Again, PEDOT:PSS was required as additional hole transport layer, as the bare MTO electrodes did not yield well-working devices within the available time and effort. However, it was demonstrated that the MTO-based electrodes perform comparably well as the reference devices on commercial ITO. And also in this case it is expected that with further optimization of the MTO/polymer interface the PEDOT:PSS could be avoided.

---

## CONCLUSIONS AND OUTLOOK

---

In this thesis, three transition metal oxides were investigated for the use in transparent electrodes and charge-selective layers. The deposition using DC magnetron sputtering at room temperature provided compatibility with flexible substrates and the state-of-the-art industrial fabrication processing of transparent electrodes. Based on the properties of the single oxide layer, transparent dielectric/metal/dielectric electrodes were designed to maximize their transmittance. The DMD electrodes, incorporating Ag or Au proved to be highly flexible due to the ductile metal layer, irrespective of the adjacent oxide.

The first investigated material was molybdenum oxide, presented in Chapter 2. While  $\text{MoO}_x$  is already a commonly used and well-studied material for hole transport in optoelectronic devices, this work explored a less established deposition technique of  $\text{MoO}_x$  by DC sputtering from a substoichiometric oxide target that allows higher deposition rates than other PVD processes. It was found that transparent, stoichiometric  $\text{MoO}_3$  layers can only be achieved when oxygen is added to the process gas. To validate the deposition process,  $\text{MoO}_x$  thin films with different oxygen content have been characterized in detail and tailored for the use in DMD transparent electrodes. Especially on flexible (PET) substrates, these electrodes outperform the industrial standard (ITO).

In the following Chapter 3, a novel composite material was introduced: molybdenum titanium oxide (MTO). Following the same objective to achieve high deposition rates with DC sputtering, a mixed  $\text{MoO}_2$ - $\text{TiO}_2$  oxide target is used to deposit thin films with different oxygen contents. Subsequently, MTO/metal/MTO electrodes are deposited in the same architecture, resulting in even higher figure of merit values than the DMDs based on pure  $\text{MoO}_x$ . Additionally, the MTO is proven to be much more stable in humidity and water compared to  $\text{MoO}_x$ , and most importantly the electronic properties of MTO such as the high work function, are similar to  $\text{MoO}_x$ .

The water stability of the two materials was studied in detail in Chapter 4. Firstly an in-line flow-cell set-up coupled to an ICP-MS is used to quantify the dissolution of both materials,  $\text{MoO}_x$  and MTO, in pure water. These confirmed the qualitative observations

of MTO withstanding short exposure to liquid water, which has been found detrimental for the  $\text{MoO}_x$  films. In fact, the dissolution of Mo decreased in MTO by a factor of  $\sim 20$  within 10 minutes of water exposure. Furthermore, the molecular water reactions on the  $\text{MoO}_x$  and MTO films were studied by infrared spectroscopy. The films were exposed to controlled humidity conditions and their degradation was compared by the strength of water adsorption and hydrolysis. Again, the MTO was confirmed as significantly more resistant to water than  $\text{MoO}_x$  due to the presence of Ti, making it a compelling material when humidity is present or processing with water-based solutions is required.

Chapter 5 presented an oxide that is known as an electron-selective material in optoelectronic devices, namely titanium oxide. In fact, niobium-doped  $\text{TiO}_2$  (TNO) with 5 at% Nb was used to enhance the electrical conductivity of the sputtering target and, thus, enabled DC mode sputtering from an oxide target to achieve a fast deposition. In this case, no additional oxygen was required to obtain highly transparent thin films. These were characterized and further implemented in DMD transparent electrodes on rigid and flexible substrates. The DMD electrodes were combined with a mesoporous  $\text{TiO}_2$  layer, processed at low temperatures ( $< 100^\circ\text{C}$ ) to make it compatible with the temperature-sensitive flexible substrates. This combination made the electrodes an appealing substrate for optoelectronic devices, where the mp- $\text{TiO}_2$  could act as scaffold layer for the active material and simultaneously as electron-transport layer together with the TNO in the DMD electrode.

This concept was tested by implementing the DMD electrodes in perovskite solar cells and organic LEDs in Chapter 6. While the TNO/metal/TNO/mp- $\text{TiO}_2$  electrodes yielded efficient perovskite solar cells, the best-performing OLEDs were achieved with a MTO/Ag/MTO electrode only in combination with PEDOT:PSS. In fact, direct charge transfer from the sputtered oxides to the active material was found insufficient in the investigated device architectures. Without additional buffer layers or surface functionalization, the devices suffered from low efficiencies due to poor charge extraction/injection and interfacial defects. However, from the interim results it is expected that more time and effort concerning interface engineering and device-specific electrode design will enhance the efficiencies and improve the direct charge-selective transport ability of the DMDs. Moreover, on PET substrates the DMD electrodes have the clear advantage of high mechanical stability, which ultimately enables reliable bendable devices.

In summary, the three different DMD stacks proved to be compelling electrodes for flexible applications, outperforming the common ITO on PET substrates. However, to simultaneously act as charge transport layers in optoelectronic devices, more detailed interface engineering is required to reduce interfacial defects and improve the charge transfer across the junction.

---

## APPENDIX

---

### 8.1 METHODS AND INSTRUMENTATION

#### 8.1.1 *Materials and deposition methods*

##### *Sputter deposition*

2.5 × 2.5 cm<sup>2</sup> glass (Menzel Gläser<sup>®</sup>) and PET (Melinex<sup>®</sup> 504) substrates were cleaned in a 1% Hellmanex<sup>®</sup>/DI-water solution in an ultrasonic bath for 15 minutes, followed by 15 minutes of sonication in de-ionized (DI) water and finally in isopropanol. The substrates were dry-blown with nitrogen before being transferred into the load-lock of the Leybold Univex 450C sputter system. All layers were sputtered in DC magnetron mode with a base pressure of 10<sup>-7</sup> mbar and without substrate heating.

Ag and Au thin films were deposited at a pressure of 2 μbar and 42 W sputter power from 10.16 cm and 7.62 cm diameter targets, respectively, resulting in a sputter rate of 0.78 nm/s for Ag and 0.8 nm/s for Au. The sputter deposition rates were determined by a surface profilometer (KLA-Tencor, Alpha-Step IQ), measuring the step height.

##### *Perovskite solar cell fabrication*

When PEDOT:PSS was used as hole transport layer, a water-based solution of PEDOT:PSS (Clevios PH1000) was filtered through a 0.45 μm PES filter onto the transparent electrode, covering the whole substrate, and spin coating in air at 4000 rpm for 45 s, followed by 30 min of drying on a hotplate at 100°C. After the transfer into the glovebox, the substrates were again heated on a hot plate at 100°C to remove any water residue from the surface. The perovskite ink (I201 from Ossila, UK) was preheated in the glovebox to 70°C for 2 hours and removed from the hot plate 15 minutes before its use. After covering the whole substrate with the ink and leaving it to soak for 5 minutes, the spin coater was run at 5000 rpm for 1 minute. 20 seconds into the spin coating, 30 μl of chlorobenzene were dispersed. Subsequently, the samples were annealed at 90°C for 2 hours on a hot plate. For the spiro-OMeTAD layer, 170 mg bis(trifluoromethane)sulfonimide Li-salt (TFSI) were dissolved in 1 ml acetonitrile and 17 μl of this solution were added to a spiro-

OMeTAD solution with 73 mg spiro-OMeTAD dissolved in 1 ml chlorobenzene. After one hour of stirring at room temperature, 29  $\mu$ l tert-butylpyridine were added into the spiro-OMeTAD/TSFI solution. The layer was then deposited by dynamical spin-coating of 50  $\mu$ l at 4000 rpm for 50 s without additional annealing. The samples were then taken out of the glovebox and inserted into the thermal evaporator, where Au contacts were deposited through a shadow mask with a diameter of 2 mm at a rate of 0.4 nm/s. The cells were then encapsulated by applying a two-component epoxy glue (UHU® Plus Sofortfest) over the surface of the sample and a glass cover slide on top of the glue, and leaving to dry for 15 minutes.

### *OLED fabrication*

#### p-i-n architecture:

When PEDOT:PSS was used, a water-based solution of PEDOT:PSS (Clevios PH1000) was filtered through a 0.45  $\mu$ m PES filter onto the MTO/Ag/MTO transparent electrode, covering the whole substrate, and spin coating in air at 4000 rpm for 45 s, followed by 30 min of drying on a hotplate at 100°C before being transferred to the glovebox. The Super Yellow (SY) solution was prepared by dissolving 5 mg of the Super yellow light-emitting PPV copolymer (PDY-132, Sigma Aldrich) per ml toluene. When deposited, the whole substrate was covered with the SY solution and spin coated at 2500 rpm for 60 s. Subsequently, the samples were annealed for approx. 30 minutes at 50°C in the glovebox and left to dry over night. In the following, polyethyleneimine (PEI) functionalized ZnO-nanoparticles are spin coated at 2000 rpm for 60 s and annealed at 60°C for 15 minutes. For the ZnO-NPs solution the 2.4wt% Nanograde N-10 solution was diluted with isopropanol to 1wt% and was then mixed with a 0.4wt% solution of PEI in isopropanol in a 2:1 volume ratio. Finally, the samples were transferred to the evaporator and Al back electrodes were thermally evaporated through a shadow mask.

#### n-i-p architecture:

Before the material deposition, PET substrates were coated with a 2 wt% solution of PMMA in acetone (spin coated at 1000 rpm for 120 s) and dried at 100°C for 15 minutes. The commercial Ti-Nanoxide ink (HT-L/SC from Solaronix®) was diluted with ethanol in a 1:4 volume ratio to achieve thinner mesoporous (mp) TiO<sub>2</sub> layers. The TNO/Ag/TNO electrodes were spin coated with the diluted mp-TiO<sub>2</sub> solution at 4000 rpm for 30 s and dried on a hot plate at 100°C for 15 minutes. The resulting layers have a thickness of ~60 nm. Subsequently, 0.4wt% polyethyleneimine (PEI) dissolved in isopropanol were spin coated at 5000 rpm for 60 s, followed by another drying step at 100°C for 10 minutes. After transferring the samples into the glovebox, the SY is deposited as described above, before being transferred to the evaporator. Then 10 nm of MoO<sub>3</sub> (from Kurt J. Lesker



Company) were evaporated on the SY as hole transport layer before Au back contacts were evaporated through a shadow mask.

### 8.1.2 Sample characterization

Sample surfaces were characterised by atomic force microscopy (AFM, Molecular Imaging Pico Plus) in tapping mode, using SSS-NCHR tips from Nanosensors<sup>TM</sup> and by field-emission scanning electron microscopy (SEM, Zeiss Ultra 40) with a beam acceleration voltage of 5 kV. The SEM was also used for energy-dispersive X-ray spectroscopy (EDX) using an accelerating voltage of 20 kV and an EDAX Octane Elect Plus detector (from AMETEK). For spectral analysis and elemental quantification, the APEX software was used, applying a standardless eZAF evaluation for quantification. The sample's crystal structure was determined by X-Ray diffractometry (XRD) at omega angle of 2-5° using Cu-K $\alpha$  ( $\lambda = 1.5419$ ) radiation (ThermoFisher Scientific ARLEquinox 100). The diffraction patterns were evaluated by Match 3! Program (Crystal Impact, Germany) full pattern profile fitting using the reference databases from Crystallography Open Database (COD). Optical spectra were measured using a Fourier transform spectrometer (FT, Bruker Vertex 70), equipped with a visible, unpolarized light source. Visible direct transmittance spectra were obtained at normal incidence, referenced to air and reflectance spectra were recorded at 13° incidence angle in reference to a calibrated mirror (STAN-SSH-NIST, Ocean Optics). Unless stated otherwise, the optical spectra are always measured with the beam entering from the substrate side. A GaP and a Si detector were used to detect light in the wavelength range from 300-550 nm and 550-1200 nm, respectively. Infrared (IR) spectra were measured in reflectance mode at an incidence angle of 13° using a DLaTGS detector, at room temperature. The reflectivity was referenced to a sputtered Au layer on a Si substrate, acting as a reference mirror.

The electronic properties of MoO<sub>x</sub> and MTO were X-ray photoemission spectroscopy (XPS) was conducted (in a JEOL JPS-9030) using a monochromatic Al-K $\alpha$  (1486 eV) excitation source. Ultra-violet photoelectron spectroscopy (UPS) spectra were obtained using the same system employing H Lyman- $\alpha$  lamp (Excitech) for photoexcitation. To measure the secondary electron cut-off (i.e. the work function), 5 V bias were applied between the sample and the analyser. In contrast, photoelectron spectroscopy (PES) measurements of TNO were performed with a Thermo Scientific MultiLab 2000. For X-ray photoelectron spectroscopy (XPS), a monochromatic Al-K $\alpha$  (1486 eV) X-ray source was used and for ultra violet PES (UPS) a He gas discharge lamp was used for UV photon generation with energy of 21.2 eV (He I line). Photoelectrons were analysed with an Alpha 110 hemispherical sector analyser, equipped with seven channel electron multipliers. For energy calibration

of the spectra, a Au spot was deposited on the sample. XPS calibration was done with the Au  $4f^{7/2}$  peak and UPS was calibrated by the Fermi edge of Au before the measurement of the sample. In order to minimize potential charging effects, an electron flood-gun was used for charge compensation in XPS experiments (not used for UPS). The sample surface was biased with -2 V during UPS measurements in order to separate the sample surface work function from the internal work function of the spectrometer. The spectra were corrected afterwards. Evaluation of the XPS spectra and extraction of peak fitting parameters was done with CASA XPS software.

A 4-point, in-line probe (Nagy SD – 600) was used to measure the sheet resistance of the electrodes. The resistivity of single TNO layers was obtained by the Van-der-Pauw method, where the sample was contacted with Au pins and Ag paste at the corners of a  $1 \times 1 \text{ cm}^2$  sample and the voltage was measured at constant current using a Keithley 2000 Digital Multimeter. The resistivity of MTO and  $\text{MoO}_x$  layers was measured by a linear 4-point set-up (using an Agilent 4156C semiconductor parameter analyzer) after sputtering Au contacts ( $\sim 100 \text{ nm}$  thick) onto  $100 \text{ nm}$ -thick samples. For the bending experiments, a motorized test stand (MARK-10 ESM303) was used. Bending cycles were performed at a speed of  $1 \text{ m/min}$ . The electrical resistance of the sample from one edge to the other, along the strain direction, was measured in intermittent steps. Silver-paste, covered with Cu adhesive tape, were used to make the contacts and the resistance was measured with the sample in the unstrained (relaxed) state.

Current-voltage (J-V) curves of solar cells were measured with two-point measurements, using a semiconductor parameter analyser (Agilent 4156C), in ambient conditions, under dark and AM1.5G-simulated illumination (LOT Oriel solar simulator). The performance of the OLEDs was studied using a source measure unit - X200 from Ossila to measure the J-V curves and a Konica Minolta LS-160 luminance meter. The voltage is increased in  $0.1 \text{ V}$  steps with a 3 seconds time interval.

### *ICP-MS*

The dissolution experiments were conducted by inductively-coupled mass spectrometry (Agilent Technologies, 7900 ICP-MS, operated by MassHunter Software) using a specially designed flow-cell attachment, where ultrapure water (Milli-Q, with resistivity  $18.2 \text{ M}\Omega \cdot \text{cm}$ ) is directed over the solid sample surface of approx.  $7 \text{ mm}^2$  (sealed by a  $3 \text{ mm}$  diameter O-ring), and finally transferred to the ICP-MS. The laminar flow was monitored by an in-line pressure sensor and by tracking the waste electrolyte exiting the instrument over time to determine the average flow rate. External calibration was done for different pressure values with multielement standard solutions (from Agilent).

### 8.1.3 Optical simulations

Optical simulations were performed using a transfer matrix method (TMM) [136, 137] algorithm implemented and described by Ebner et al.[138] and Bauch et al.[105] in a python code. Generally, the TMM accounts for several coherent layers with up to hundreds of nanometres thickness and calculates the transmittance and reflectance of the multilayer stack by considering the transmission/reflection of light at the interfaces as well as the light propagation (absorption) within each layer using the Fresnel equations. The (thick) substrate is assumed as infinitely thick and the air/substrate interface is taken into account by calculating the transmittance and reflectance by the Fresnel equations. Surface/interface roughness can be accounted for by introducing an effective medium described by a weighted average refractive index of the two adjacent layers. Depending on the specific implementation of the TMM, the calculated output can be the transmittance/reflectance spectrum of a (multi)layer, the average transmittance as a function of the layer thickness in the form of a heat map, or inversely the refractive index. However, the calculation is always based on the basic Fresnel equations describing the scattering and propagation of light across (multiple) layers and interfaces [136].

The refractive indices of the sputtered oxides was extracted from the measured transmittance and reflectance spectra also with a TMM calculation, while the refractive indices of Ag [139] and Au[140] were taken from literature.

### 8.1.4 Tauc method

The optical band gap energies are determined using Tauc plots [103]. To this end, the absorption coefficient  $\alpha$  is calculated from the transmittance ( $T$ ) and reflectance ( $R$ ) spectra of the thin films on glass as follows:

$$\alpha = \frac{1}{d} \ln \frac{(1 - R)}{T/T_{glass}}$$

The absorption coefficient is related to the photon energy ( $h\nu$ ) and the band gap energy ( $E_g$ ) according to the following equation:

$$(\alpha h\nu)^n = A(h\nu - E_g)$$

where  $A$  is a constant (band tailing parameter) and  $n$  indicates the nature of the band gap. For direct optical transitions  $n = 2$ , while for indirect transitions  $n = 1/2$ . Plotting  $(\alpha h\nu)^n$  versus the photon energy  $h\nu$  gives a straight line in a certain region. The intersection of the  $h\nu$ -axis with a linear fit of this region then yields the band gap energy.

Depending on the chosen region of the fit, one can assume an average error of  $\pm 0.05$  eV.

## 8.2 COPYRIGHT CLEARANCES

Rightslink® by Copyright Clearance Center

https://s100.copyright.com/AppDispatchServlet#formTop



- Home
- Help
- Live Chat
- Selina Goetz

**SPRINGER NATURE**

**Thin-film metal oxides in organic semiconductor devices: their electronic structures, work functions and interfaces**

Author: Mark T Greiner et al  
 Publication: NPG Asia Materials  
 Publisher: Springer Nature  
 Date: Jul 19, 2013  
 Copyright © 2013, The Author(s)

**Creative Commons**

The request you have made is considered to be non-commercial/educational. As the article you have requested has been distributed under a Creative Commons license (Attribution-Noncommercial), you may reuse this material for non-commercial/educational purposes without obtaining additional permission from Springer Nature, providing that the author and the original source of publication are fully acknowledged (please see the article itself for the license version number). You may reuse this material without obtaining permission from Springer Nature, providing that the author and the original source of publication are fully acknowledged, as per the terms of the license. For license terms, please see <http://creativecommons.org>

BACK CLOSE WINDOW

© 2023 Copyright - All Rights Reserved | Copyright Clearance Center, Inc. | Privacy statement | Data Security and Privacy  
 | For California Residents | Terms and Conditions Comments? We would like to hear from you. E-mail us at [customer@copyright.com](mailto:customer@copyright.com)

Die approbierte gedruckte Originalversion dieser Dissertation ist an der TU Wien Bibliothek verfügbar.  
 The approved original version of this doctoral thesis is available in print at TU Wien Bibliothek.



RightsLink Printable License

<https://s100.copyright.com/AppDispatchServlet>

## SPRINGER NATURE LICENSE TERMS AND CONDITIONS

Jan 19, 2023

---

This Agreement between Selina Goetz ("You") and Springer Nature ("Springer Nature") consists of your license details and the terms and conditions provided by Springer Nature and Copyright Clearance Center.

License Number	5472550050260
License date	Jan 19, 2023
Licensed Content Publisher	Springer Nature
Licensed Content Publication	Journal of Materials Science
Licensed Content Title	Fast sputter deposition of MoOx/metal/MoOx transparent electrodes on glass and PET substrates
Licensed Content Author	Selina Goetz et al
Licensed Content Date	Feb 15, 2021
Type of Use	Thesis/Dissertation
Requestor type	non-commercial (non-profit)
Format	print and electronic
Portion	full article/chapter
Will you be translating?	no



Help ▾ Live Chat



**Transparent electrodes based on molybdenum-titanium-oxide with increased water stability for use as hole-transport/hole-injection components**

**Author:** Selina Goetz et al  
**Publication:** Journal of Materials Science  
**Publisher:** Springer Nature  
**Date:** May 6, 2022

*Copyright © 2022, The Author(s)*

**Creative Commons**

This is an open access article distributed under the terms of the [Creative Commons CC BY](#) license, which permits unrestricted use, distribution, and reproduction in any medium, provided the original work is properly cited.


You are not required to obtain permission to reuse this article.  
To request permission for a type of use not listed, please contact [Springer Nature](#)

© 2023 Copyright - All Rights Reserved | [Copyright Clearance Center, Inc.](#) | [Privacy statement](#) | [Data Security and Privacy](#)  
| [For California Residents](#) | [Terms and Conditions](#)Comments? We would like to hear from you. E-mail us at [customer-care@copyright.com](mailto:customer-care@copyright.com)

Die approbierte gedruckte Originalversion dieser Dissertation ist an der TU Wien Bibliothek verfügbar.  
The approved original version of this doctoral thesis is available in print at TU Wien Bibliothek.




Rightslink® by Copyright Clearance Center

<https://s100.copyright.com/AppDispatchServlet>


[Home](#) | [? Help](#) | [Live Chat](#) | [Selina Goetz](#)

---



**Low-Temperature-Processed Transparent Electrodes Based on Compact and Mesoporous Titanium Oxide Layers for Flexible Perovskite Solar Cells**

**Author:** Selina Goetz, Daniella Mehanni, Neha Bansal, et al

**Publication:** ACS Applied Energy Materials

**Publisher:** American Chemical Society

**Date:** May 1, 2022

Copyright © 2022, American Chemical Society

**PERMISSION/LICENSE IS GRANTED FOR YOUR ORDER AT NO CHARGE**

This type of permission/license, instead of the standard Terms and Conditions, is sent to you because no fee is being charged for your order. Please note the following:

- Permission is granted for your request in both print and electronic formats, and translations.
- If figures and/or tables were requested, they may be adapted or used in part.
- Please print this page for your records and send a copy of it to your publisher/graduate school.
- Appropriate credit for the requested material should be given as follows: "Reprinted (adapted) with permission from (COMPLETE REFERENCE CITATION). Copyright (YEAR) American Chemical Society." Insert appropriate information in place of the capitalized words.
- One-time permission is granted only for the use specified in your RightsLink request. No additional uses are granted (such as derivative works or other editions). For any uses, please submit a new request.

If credit is given to another source for the material you requested from RightsLink, permission must be obtained from that source.

[BACK](#)
[CLOSE WINDOW](#)

© 2023 Copyright - All Rights Reserved | [Copyright Clearance Center, Inc.](#) | [Privacy statement](#) | [Data Security and Privacy](#)  
 | [For California Residents](#) | [Terms and Conditions](#) Comments? We would like to hear from you. E-mail us at [customer@copyright.com](mailto:customer@copyright.com)





---

## BIBLIOGRAPHY

---

- [1] Snehangshu Mishra, Subrata Ghosh, and Trilok Singh. Progress in Materials Development for Flexible Perovskite Solar Cells and Future Prospects. *ChemSusChem*, 14(2):512–538, jan 2021.
- [2] Jin Hyuck Heo, David S. Lee, Dong Hee Shin, and Sang Hyuk Im. Recent advancements in and perspectives on flexible hybrid perovskite solar cells. *Journal of Materials Chemistry A*, 7(3):888–900, 2019.
- [3] Xiangfei Xu, Liya Sun, Kang Shen, and Shiming Zhang. Organic and hybrid organic-inorganic flexible optoelectronics: Recent advances and perspectives. *Synthetic Metals*, 256(March):116137, 2019.
- [4] Hao Chen, Hao Wang, Jiang Wu, Feng Wang, Ting Zhang, Yafei Wang, Detao Liu, Shibin Li, Richard V. Penty, and Ian H. White. Flexible optoelectronic devices based on metal halide perovskites. *Nano Research*, 13(8):1997–2018, aug 2020.
- [5] Kenjiro Fukuda, Kilho Yu, and Takao Someya. The Future of Flexible Organic Solar Cells. *Advanced Energy Materials*, 10(25):1–10, 2020.
- [6] Yue Feng Liu, Jing Feng, Yan Gang Bi, Da Yin, and Hong Bo Sun. Recent Developments in Flexible Organic Light-Emitting Devices. *Advanced Materials Technologies*, 4(1):1–19, 2019.
- [7] Hyun Suk Jung and Nam Gyu Park. Perovskite solar cells: From materials to devices. *Small*, 11(1):10–25, 2015.
- [8] Hanul Min, Do Yoon Lee, Junu Kim, Gwisu Kim, Kyoung Su Lee, Jongbeom Kim, Min Jae Paik, Young Ki Kim, Kwang S. Kim, Min Gyu Kim, Tae Joo Shin, and Sang Il Seok. Perovskite solar cells with atomically coherent interlayers on SnO<sub>2</sub> electrodes. *Nature*, 598(7881):444–450, oct 2021.
- [9] Caleb C. Boyd, Rongrong Cheacharoen, Tomas Leijtens, and Michael D. McGehee. Understanding Degradation Mechanisms and Improving Stability of Perovskite Photovoltaics. *Chemical Reviews*, 119(5):3418–3451, 2019.
- [10] Fu Yang, Yuting Huang, Yaowen Li, and Yongfang Li. Large-area flexible organic solar cells. *npj Flexible Electronics*, 5(1):1–12, 2021.

- [11] S. Sharma, S. Shriwastava, S. Kumar, K. Bhatt, and C. Charu Tripathi. Alternative transparent conducting electrode materials for flexible optoelectronic devices. *Opto-Electronics Review*, 26(3):223–235, sep 2018.
- [12] Mark T. Greiner and Zheng Hong Lu. Thin-film metal oxides in organic semiconductor devices: Their electronic structures, work functions and interfaces. *NPG Asia Materials*, 5(7):e55–16, 2013.
- [13] Mark T. Greiner, Michael G. Helander, Wing-Man Tang, Zhi-Bin Wang, Jacky Qiu, and Zheng-Hong Lu. Universal energy-level alignment of molecules on metal oxides. *Nature Materials*, 11(1):76–81, jan 2012.
- [14] Jens Meyer, Sami Hamwi, Michael Kröger, Wolfgang Kowalsky, Thomas Riedl, and Antoine Kahn. Transition metal oxides for organic electronics: Energetics, device physics and applications. *Advanced Materials*, 24(40):5408–5427, 2012.
- [15] Xinge Yu, Tobin J. Marks, and Antonio Facchetti. Metal oxides for optoelectronic applications. *Nature Materials*, 15(4):383–396, apr 2016.
- [16] S. Berg and T. Nyberg. Fundamental understanding and modeling of reactive sputtering processes. *Thin Solid Films*, 476(2):215–230, 2005.
- [17] Tadatsugu Minami. Transparent conducting oxide semiconductors for transparent electrodes. *Semiconductor Science and Technology*, 20(4), 2005.
- [18] Klaus Ellmer. Past achievements and future challenges in the development of optically transparent electrodes. *Nature Photonics*, 6, 2012.
- [19] Elvira Fortunato, David Ginley, Hideo Hosono, and David C Paine. Transparent for Photovoltaics Transparent Conducting Oxides :. *Mrs Bulletin*, 32(March 2007):242–247, 2017.
- [20] C. Guillén and J. Herrero. TCO/metal/TCO structures for energy and flexible electronics. *Thin Solid Films*, 520(1):1–17, 2011.
- [21] Kirill Zilberberg and Thomas Riedl. Metal-nanostructures: a modern and powerful platform to create transparent electrodes for thin-film photovoltaics. *J. Mater. Chem. A*, 2016.
- [22] David S. Hecht, Liangbing Hu, and Glen Irvin. Emerging transparent electrodes based on thin films of carbon nanotubes, graphene, and metallic nanostructures. *Advanced Materials*, 23(13):1482–1513, 2011.
- [23] L. Cattin, J. C. Bernède, and M. Morsli. Toward indium-free optoelectronic devices: Dielectric/metal/dielectric alternative transparent conductive electrode in

- organic photovoltaic cells. *Physica Status Solidi (A) Applications and Materials Science*, 210(6):1047–1061, 2013.
- [24] John C. C. Fan, Frank J. Bachner, George H. Foley, and Paul M. Zavracky. Transparent heat-mirror films of  $\text{TiO}_2/\text{Ag}/\text{TiO}_2$  for solar energy collection and radiation insulation. *Applied Physics Letters*, 25(12):693–695, dec 1974.
- [25] L. Cattin, Y. Lare, M. Makha, M. Fleury, F. Chandezon, T. Abachi, M. Morsli, K. Napo, M. Addou, and J. C. Bernède. Effect of the Ag deposition rate on the properties of conductive transparent  $\text{MoO}_3/\text{Ag}/\text{MoO}_3$  multilayers. *Solar Energy Materials and Solar Cells*, 117:103–109, 2013.
- [26] Zhao Zhao and T.L. Alford. The optimal  $\text{TiO}_2/\text{Ag}/\text{TiO}_2$  electrode for organic solar cell application with high device-specific Haacke figure of merit. *Solar Energy Materials and Solar Cells*, 157:599–603, dec 2016.
- [27] Po Ching Kao, Cheng Jie Hsieh, Ze Hui Chen, and Sy Hann Chen. Improvement of  $\text{MoO}_3/\text{Ag}/\text{MoO}_3$  multilayer transparent electrodes for organic solar cells by using UV–ozone treated  $\text{MoO}_3$  layer. *Solar Energy Materials and Solar Cells*, 186(September 2017):131–141, 2018.
- [28] T. Abachi, L. Cattin, G. Louarn, Y. Lare, A. Bou, M. Makha, P. Torchio, M. Fleury, M. Morsli, M. Addou, and J.C. Bernède. Highly flexible, conductive and transparent  $\text{MoO}_3/\text{Ag}/\text{MoO}_3$  multilayer electrode for organic photovoltaic cells. *Thin Solid Films*, 545:438–444, oct 2013.
- [29] Xuanhuai Lin, Hui Luo, Xiangkun Jia, Jinfeng Wang, Jianping Zhou, Ziyao Jiang, Likun Pan, Sumei Huang, and Xiaohong Chen. Efficient and ultraviolet durable inverted polymer solar cells using thermal stable GZO-AgTi-GZO multilayers as a transparent electrode. *Organic Electronics*, 39:177–183, 2016.
- [30] Hongjiang Li, Xiaohui Liu, Weiyan Wang, Yuehui Lu, Jinhua Huang, Jia Li, Junjun Xu, Pengxuan Fan, Junfeng Fang, and Weijie Song. Realization of Foldable Polymer Solar Cells Using Ultrathin Cellophane Substrates and  $\text{ZnO}/\text{Ag}/\text{ZnO}$  Transparent Electrodes. *Solar RRL*, 2(10):1–9, 2018.
- [31] Lukas Kinner, Martin Bauch, Rachmat Adhi Wibowo, Giovanni Ligorio, Emil J.W. List-Kratochvil, and Theodoros Dimopoulos. Polymer interlayers on flexible PET substrates enabling ultra-high performance, ITO-free dielectric/metal/dielectric transparent electrode. *Materials and Design*, 168:107663, 2019.
- [32] Anies Mutiari, Theodoros Dimopoulos, Martin Bauch, Ankit Mittal, Matthias Weil, and Rachmat Adhi Wibowo. Design and implementation of an ultrathin dielectric/metal/dielectric transparent electrode for  $\text{Cu}_2\text{ZnSnS}_4$  thin-film photovoltaics. *Solar Energy Materials and Solar Cells*, 230(June):111247, sep 2021.

- [33] Selina Goetz, Rachmat Adhi Wibowo, Martin Bauch, Neha Bansal, Giovanni Ligorio, Emil List-Kratochvil, Christian Linke, Enrico Franzke, Jörg Winkler, Markus Valtiner, and Theodoros Dimopoulos. Fast sputter deposition of MoOx/metal/MoOx transparent electrodes on glass and PET substrates. *Journal of Materials Science*, 56(15):9047–9064, may 2021.
- [34] Maria Vasilopoulou, Antonios M. Douvas, Dimitra G. Georgiadou, Leonidas C. Palilis, Stella Kennou, Labrini Sygellou, Anastasia Soultati, Ioannis Kostis, Giorgos Papadimitropoulos, Dimitris Davazoglou, and Panagiotis Argitis. The influence of hydrogenation and oxygen vacancies on molybdenum oxides work function and gap states for application in organic optoelectronics. *Journal of the American Chemical Society*, 134(39):16178–16187, 2012.
- [35] M. Kröger, S. Hamwi, J. Meyer, T. Riedl, W. Kowalsky, and A. Kahn. Role of the deep-lying electronic states of MoO<sub>3</sub> in the enhancement of hole-injection in organic thin films. *Applied Physics Letters*, 95(12):2–4, 2009.
- [36] K. Inzani, M. Nematollahi, F. Vullum-Bruer, T. Grande, T. W. Reenaas, and S. M. Selbach. Electronic properties of reduced molybdenum oxides. *Physical Chemistry Chemical Physics*, 19(13):9232–9245, 2017.
- [37] Tarsame S. Sian and G. B. Reddy. Optical, structural and photoelectron spectroscopic studies on amorphous and crystalline molybdenum oxide thin films. *Solar Energy Materials and Solar Cells*, 82(3):375–386, 2004.
- [38] David O. Scanlon, Graeme W. Watson, D. J. Payne, G. R. Atkinson, R. G. Egdell, and D. S.L. Law. Theoretical and experimental study of the electronic structures of MoO<sub>3</sub> and MoO<sub>2</sub>. *Journal of Physical Chemistry C*, 114(10):4636–4645, 2010.
- [39] André L.F. Cauduro, Roberto Dos Reis, Gong Chen, Andreas K. Schmid, Christophe Méthivier, Horst Günter Rubahn, Léo Bossard-Giannesini, Hervé Cruguel, Nadine Witkowski, and Morten Madsen. Crystalline Molybdenum Oxide Thin-Films for Application as Interfacial Layers in Optoelectronic Devices. *ACS Applied Materials and Interfaces*, 9(8):7717–7724, 2017.
- [40] Corsin Battaglia, Xingtian Yin, Maxwell Zheng, Ian D. Sharp, Teresa Chen, Stephen McDonnell, Angelica Azcatl, Carlo Carraro, Biwu Ma, Roya Maboudian, Robert M. Wallace, and Ali Javey. Hole selective MoOx contact for silicon solar cells. *Nano Letters*, 14(2):967–971, 2014.
- [41] Jens Meyer. Electronic structure of molybdenum-oxide films and associated charge injection mechanisms in organic devices. *Journal of Photonics for Energy*, 1(1):011109, jan 2011.

- [42] Kevin J. Rietwyk, David A. Keller, Adam Ginsburg, Hannah-Noa Barad, Maayan Priel, Koushik Majhi, Zhi Yan, Shay Tirosh, Assaf Y. Anderson, Lothar Ley, and Arie Zaban. Universal Work Function of Metal Oxides Exposed to Air. *Advanced Materials Interfaces*, 6(12):1802058, jun 2019.
- [43] Isabela Alves de Castro, Robi Shankar Datta, Jian Zhen Ou, Andres Castellanos-Gomez, Sharath Sriram, Torben Daeneke, and Kouros Kalantar-zadeh. Molybdenum Oxides – From Fundamentals to Functionality. *Advanced Materials*, 29(40):1–31, 2017.
- [44] N. Miyata and S. Akiyoshi. Preparation and electrochromic properties of rf-sputtered molybdenum oxide films. *Journal of Applied Physics*, 58(4):1651–1655, 1985.
- [45] André L. Fernandes Cauduro, Zacarias E. Fabrim, Mehrad Ahmadpour, Paulo F. P. Fichtner, Søren Hassing, Horst-Günter Rubahn, and Morten Madsen. Tuning the optoelectronic properties of amorphous MoO<sub>x</sub> films by reactive sputtering. *Applied Physics Letters*, 106(20):202101, may 2015.
- [46] C. Z. Chen, Y. Li, and X. D. Tang. Evidence of oxygen vacancy and possible intermediate gap state in layered  $\alpha$ -MoO<sub>3</sub> single-crystal nanobelts. *Physica B: Condensed Matter*, 481:192–196, 2016.
- [47] S. H. Mohamed and S. Venkataraj. Thermal stability of amorphous molybdenum trioxide films prepared at different oxygen partial pressures by reactive DC magnetron sputtering. *Vacuum*, 81(5):636–643, 2007.
- [48] M. Sendova-Vassileva, Hr Dikov, P. Vitanov, G. Popkirov, R. Gergova, G. Grancharov, and V. Gancheva. Magnetron Sputtered Molybdenum Oxide for Application in Polymers Solar Cells. *Journal of Physics: Conference Series*, 764(1):012022, oct 2016.
- [49] G. Haacke. New figure of merit for transparent conductors. *Journal of Applied Physics*, 47(9):4086–4089, 1976.
- [50] Ozan Akdemir, Mona Zolfaghari Borra, Hisham Nasser, Raşit Turan, and Alpan Bek. MoO<sub>x</sub>/Ag/MoO<sub>x</sub> multilayers as hole transport transparent conductive electrodes for n-type crystalline silicon solar cells. *International Journal of Energy Research*, 44(4):3098–3109, 2020.
- [51] Kiyoshi Chiba and Kenji Nakatani. Photoenhance migration of silver atoms in transparent heat mirror coatings. *Thin Solid Films*, 112(4):359–367, feb 1984.
- [52] L. Cattin, El Jouad, N. Stephant, G. Louarn, M. Morsli, M. Hsein, Y. Mouchaal, S. Thouiri, M. Addou, A. Khelil, and J. C. Bernède. Dielectric/metal/dielectric

- alternative transparent electrode: Observations on stability/degradation. *Journal of Physics D: Applied Physics*, 50(37):375502, sep 2017.
- [53] Jonathan Griffin, Darren C. Watters, Hunan Yi, Ahmed Iraqi, David Lidzey, and Alastair R. Buckley. The Influence of MoO<sub>x</sub> Anode Stoichiometry on the Performance of Bulk Heterojunction Polymer Solar Cells. *Advanced Energy Materials*, 3(7):903–908, jul 2013.
- [54] Xiaxia Liao, Ah Reum Jeong, Regan G. Wilks, Sven Wiesner, Marin Rusu, Roberto Félix, Ting Xiao, Claudia Hartmann, and Marcus Bär. Tunability of MoO<sub>3</sub> Thin-Film Properties Due to Annealing in Situ Monitored by Hard X-ray Photoemission. *ACS Omega*, 4(6):10985–10990, jun 2019.
- [55] Sang-II Park, Jong-Hyun Ahn, Xue Feng, Shuodao Wang, Yonggang Huang, and John A. Rogers. Theoretical and Experimental Studies of Bending of Inorganic Electronic Materials on Plastic Substrates. *Advanced Functional Materials*, 18(18):2673–2684, sep 2008.
- [56] Selina Goetz, Rachmat Adhi Wibowo, Martin Bauch, Neha Bansal, Giovanni Ligorio, Emil List-Kratochvil, Christian Linke, Enrico Franzke, Jörg Winkler, Markus Valtiner, and Theodoros Dimopoulos. Transparent electrodes based on molybdenum–titanium–oxide with increased water stability for use as hole-transport/hole-injection components. *Journal of Materials Science*, 57(19):8752–8766, 2022.
- [57] Bohao Li, He Ren, Hongyi Yuan, Alamgir Karim, and Xiong Gong. Room-Temperature, Solution-Processed MoO<sub>x</sub> Thin Film as a Hole Extraction Layer to Substitute PEDOT/PSS in Polymer Solar Cells. *ACS Photonics*, 1(2):87–90, feb 2014.
- [58] Fengxia Wang, Xianfeng Qiao, Tao Xiong, and Dongge Ma. The role of molybdenum oxide as anode interfacial modification in the improvement of efficiency and stability in organic light-emitting diodes. *Organic Electronics*, 9(6):985–993, 2008.
- [59] Mehrad Ahmadpour, André L. Fernandes Cauduro, Christophe Méthivier, Birgit Kunert, Chiara Labanti, Roland Resel, Vida Turkovic, Horst Günter Rubahn, Nadine Witkowski, Andreas K. Schmid, and Morten Madsen. Crystalline molybdenum oxide layers as efficient and stable hole contacts in organic photovoltaic devices. *ACS Applied Energy Materials*, 2(1):420–427, 2019.
- [60] Keith T. Butler, Rachel Crespo-Otero, John Buckeridge, David O. Scanlon, Edward Bovill, David Lidzey, and Aron Walsh. Band energy control of molybdenum oxide by surface hydration. *Applied Physics Letters*, 107(23), 2015.
- [61] Michael C. Gwinner, Riccardo Di Pietro, Yana Vaynzof, Kathryn J. Greenberg, Peter K.H. Ho, Richard H. Friend, and Henning Sirringhaus. Doping of organic

- semiconductors using molybdenum trioxide: A quantitative time-dependent electrical and spectroscopic study. *Advanced Functional Materials*, 21(8):1432–1441, 2011.
- [62] Irfan, Huanjun Ding, Yongli Gao, Cephas Small, Do Young Kim, Jegadesan Subbiah, and Franky So. Energy level evolution of air and oxygen exposed molybdenum trioxide films. *Applied Physics Letters*, 96(24):10–12, 2010.
- [63] Tarsame S. Sian and G.B. Reddy. Effect of stoichiometry and microstructure on hydrolysis in MoO<sub>3</sub> films. *Chemical Physics Letters*, 418(1-3):170–173, jan 2006.
- [64] Zhu Luo, Ran Miao, Tran Doan Huan, Islam M. Mosa, Altug S. Poyraz, Wei Zhong, Jacqueline E. Cloud, David A. Kriz, Srinivas Thanneeru, Junkai He, Yashan Zhang, Rampi Ramprasad, and Steven L. Suib. Mesoporous MoO<sub>3-x</sub> Material as an Efficient Electrocatalyst for Hydrogen Evolution Reactions. *Advanced Energy Materials*, 6(16), 2016.
- [65] Ashley R. Head, Chiara Gattinoni, Lena Trotochaud, Yi Yu, Osman Karslıoğlu, Sven Pletincx, Bryan Eichhorn, and Hendrik Bluhm. Water (Non-)Interaction with MoO<sub>3</sub>. *Journal of Physical Chemistry C*, 123(27):16836–16842, 2019.
- [66] M. Pourbaix. *Atlas of Electrochemical Equilibria in Aqueous Solutions*, volume 2. National Association of Corrosion Engineers, 1974.
- [67] Eom Ji Kim, Jaewook Shin, Junu Bak, Sang Jae Lee, Ki hyun Kim, Dong Hoon Song, Jeong Han Roh, Yongju Lee, Hyo Won Kim, Kug Seung Lee, and Eun Ae Cho. Stabilizing role of Mo in TiO<sub>2</sub>-MoO<sub>x</sub> supported Ir catalyst toward oxygen evolution reaction. *Applied Catalysis B: Environmental*, 280(May 2020), 2021.
- [68] Ke Chen, Shaofeng Deng, Yun Lu, Mingxing Gong, Yezhou Hu, Tonghui Zhao, Tao Shen, and Deli Wang. Molybdenum-doped titanium dioxide supported low-Pt electrocatalyst for highly efficient and stable hydrogen evolution reaction. *Chinese Chemical Letters*, 32(2):765–769, 2021.
- [69] Abdul Qayyum Khan, Shuai Yuan, Sheng Niu, Lijuan Zheng, Wenxue Li, and Heping Zeng. Synthesis of molybdenum oxide-titanium dioxide nanocomposites with ultrashort laser ablation in water. *Optics Express*, 25(12):A539, 2017.
- [70] Anna Khlyustova, Nikolay Sirotkin, Valeriy Titov, and Alexander Agafonov. Effect of low-temperature underwater plasma produced of new properties of Mo–Ti mixed oxide composites for electron transport layer in the dye-sensitized solar cells. *Journal of Alloys and Compounds*, 858:157664, 2021.
- [71] Hui Liu, Ting Lv, Chunkui Zhu, and Zhenfeng Zhu. Direct bandgap narrowing of TiO<sub>2</sub>/MoO<sub>3</sub> heterostructure composites for enhanced solar-driven photocatalytic activity. *Solar Energy Materials and Solar Cells*, 153:1–8, 2016.

- [72] Ning Li, Yamei Li, Wenjing Li, Shidong Ji, and Ping Jin. One-Step Hydrothermal Synthesis of  $\text{TiO}_2@\text{MoO}_3$  Core-Shell Nanomaterial: Microstructure, Growth Mechanism, and Improved Photochromic Property. *Journal of Physical Chemistry C*, 120(6):3341–3349, 2016.
- [73] Martijn F. J. Vos, Bart Macco, Nick F. W. Thissen, Ageeth A. Bol, and W. M. M. (Erwin) Kessels. Atomic layer deposition of molybdenum oxide from  $(\text{N t Bu})_2(\text{NMe}_2)_2\text{Mo}$  and  $\text{O}_2$  plasma. *Journal of Vacuum Science & Technology A: Vacuum, Surfaces, and Films*, 34(1):01A103, 2016.
- [74] Christian Stelling, Chetan R. Singh, Matthias Karg, Tobias A.F. König, Mukundan Thelakkat, and Markus Retsch. Plasmonic nanomeshes: Their ambivalent role as transparent electrodes in organic solar cells. *Scientific Reports*, 7(January):1–13, 2017.
- [75] Swagato Sarkar, Vaibhav Gupta, Mohit Kumar, Jonas Schubert, Patrick T. Probst, Joby Joseph, and Tobias A.F. König. Hybridized Guided-Mode Resonances via Colloidal Plasmonic Self-Assembled Grating. *ACS Applied Materials and Interfaces*, 11(14):13752–13760, 2019.
- [76] Thomas Siefke, Stefanie Kroker, Kristin Pfeiffer, Oliver Puffky, Kay Dietrich, Daniel Franta, Ivan Ohlídal, Adriana Szeghalmi, Ernst Bernhard Kley, and Andreas Tünnermann. Materials Pushing the Application Limits of Wire Grid Polarizers further into the Deep Ultraviolet Spectral Range. *Advanced Optical Materials*, 4(11):1780–1786, 2016.
- [77] M. Landmann, T. Köhler, S. Köppen, E. Rauls, T. Frauenheim, and W. G. Schmidt. Fingerprints of order and disorder in the electronic and optical properties of crystalline and amorphous  $\text{TiO}_2$ . *Physical Review B - Condensed Matter and Materials Physics*, 86(6):24–28, 2012.
- [78] Bin Hu, Liqiang Mai, Wen Chen, and Fan Yang. From  $\text{MoO}_3$  nanobelts to  $\text{MoO}_2$  nanorods: Structure transformation and electrical transport. *ACS Nano*, 3(2):478–482, 2009.
- [79] R. T. Poole. The colour of the noble metals. *Physics Education*, 18(6):280–283, 1983.
- [80] J. B. Malherbe, S. Hofmann, and J. M. Sanz. Preferential sputtering of oxides: A comparison of model predictions with experimental data. *Applied Surface Science*, 27(3):355–365, 1986.
- [81] H. M. Naguib and R. Kelly. On the increase in the electrical conductivity of  $\text{MoO}_3$  and  $\text{V}_2\text{O}_5$  following ion bombardment. Studies on bombardment-enhanced conductivity-I. *Journal of Physics and Chemistry of Solids*, 33(7-9):1751–1759, 1972.



- [82] Bing-Yue Tsui and Chih-Feng Huang. Wide range work function modulation of binary alloys for MOSFET application. *IEEE Electron Device Letters*, 24(3):153–155, mar 2003.
- [83] Shun Kashiwaya, Jan Morasch, Verena Streibel, Thierry Toupance, Wolfram Jaegermann, and Andreas Klein. The Work Function of TiO<sub>2</sub>. *Surfaces*, 1(1):73–89, sep 2018.
- [84] Shahram Shafaei, Daniel Van Opdenbosch, Tobias Fey, Marcus Koch, Tobias Kraus, Josef Peter Guggenbichler, and Cordt Zollfrank. Enhancement of the antimicrobial properties of orthorhombic molybdenum trioxide by thermal induced fracturing of the hydrates. *Materials Science and Engineering C*, 58:1064–1070, 2016.
- [85] K. U. Rempel, A. E. Williams-Jones, and A. A. Migdisov. The solubility of molybdenum dioxide and trioxide in HCl-bearing water vapour at 350 °C and pressures up to 160 bars. *Geochimica et Cosmochimica Acta*, 72(13):3074–3083, 2008.
- [86] Md Maniruzzaman, Chae Hwi Lim, Kiyul Yang, Chiyoun Lee, Ho Seok Nam, and Jaegab Lee. Indium tin oxide-free PEDOT:PSS/SAM/MoO<sub>3</sub>/Au/MoO<sub>3</sub> multilayer electrodes for organic solar cells. *Journal of Nanoscience and Nanotechnology*, 14(10):7779–7783, 2014.
- [87] The Merck Index, 10th Ed. Edited By Martha Windholz. Merck. *Journal of Pharmaceutical Sciences*, 73(6):862, jun 1984.
- [88] Claudine Noguera. *Physics and Chemistry at Oxide Surfaces*. Cambridge University Press, 1996.
- [89] Selina Goetz, Daniella Mehanni, Neha Bansal, Bernhard Kubicek, Rachmat Adhi Wibowo, Martin Bauch, Christian Linke, Enrico Franzke, Jörg Winkler, Toby Meyer, Stephanie Narbey, David Stock, Markus Valtiner, and Theodoros Dimopoulos. Low-Temperature-Processed Transparent Electrodes Based on Compact and Mesoporous Titanium Oxide Layers for Flexible Perovskite Solar Cells. *ACS Applied Energy Materials*, sep 2021.
- [90] Taro Hitosugi, Naoomi Yamada, Shoichiro Nakao, Yasushi Hirose, and Tetsuya Hasegawa. Properties of TiO<sub>2</sub>-based transparent conducting oxides. *Physica Status Solidi (A) Applications and Materials Science*, 207(7):1529–1537, 2010.
- [91] S. X. Zhang, D. C. Kundaliya, W. Yu, S. Dhar, S. Y. Young, L. G. Salamanca-Riba, S. B. Ogale, R. D. Vispute, and T. Venkatesan. Niobium doped TiO<sub>2</sub>: Intrinsic transparent metallic anatase versus highly resistive rutile phase. *Journal of Applied Physics*, 102(1):1–5, 2007.

- [92] S.M.M. Ramos, B. Canut, R. Brenier, L. Gea, L. Romana, M. Brunel, and P. Thevenard. Electrical conductivity in niobium implanted TiO<sub>2</sub> rutile. *Nuclear Instruments and Methods in Physics Research Section B: Beam Interactions with Materials and Atoms*, 80-81:1123–1127, jan 1993.
- [93] Girija Sahasrabudhe, Jason Krizan, Susanna L. Bergman, Robert J. Cava, and Jeffrey Schwartz. Million-fold Increase of the Conductivity in TiO<sub>2</sub>Rutile through 3Niobium Incorporation. *Chemistry of Materials*, 28(11):3630–3633, 2016.
- [94] Stefan Seeger, Klaus Ellmer, Michael Weise, Daniela Gogova, Daniel Abou-Ras, and Rainald Mientus. Reactive magnetron sputtering of Nb-doped TiO<sub>2</sub> films: Relationships between structure, composition and electrical properties. *Thin Solid Films*, 605:44–52, 2016.
- [95] Mi-Hee Jung, Nae-Man Park, and Sun-Young Lee. Color tunable nanopaper solar cells using hybrid CH<sub>3</sub>NH<sub>3</sub>PbI<sub>3-x</sub>Br<sub>x</sub> perovskite. *Solar Energy*, 139:458–466, dec 2016.
- [96] Hongjiang Li, Xiaodong Li, Weiyan Wang, Jinhua Huang, Jia Li, Shiqiang Huang, Bing Fan, Junfeng Fang, and Weijie Song. Ultraflexible and biodegradable perovskite solar cells utilizing ultrathin cellophane paper substrates and TiO<sub>2</sub>/Ag/TiO<sub>2</sub> transparent electrodes. *Solar Energy*, 188(May):158–163, 2019.
- [97] Naoomi Yamada, Taro Hitosugi, Junpei Kasai, Ngoc Lam Huong Hoang, Shoichiro Nakao, Yasushi Hirose, Toshihiro Shimada, and Tetsuya Hasegawa. Direct growth of transparent conducting Nb-doped anatase TiO<sub>2</sub> polycrystalline films on glass. *Journal of Applied Physics*, 105(12), 2009.
- [98] Kashif Safeen, V. Micheli, R. Bartali, G. Gottardi, Akif Safeen, Hafeez Ullah, and N. Laidani. Synthesis of conductive and transparent Nb-doped TiO<sub>2</sub> films: Role of the target material and sputtering gas composition. *Materials Science in Semiconductor Processing*, 66(January):74–80, 2017.
- [99] Stephan Ulrich, Christian Szyszko, Sebastian Jung, and Michael Vergöhl. Electrochromic properties of mixed oxides based on titanium and niobium for smart window applications. *Surface and Coatings Technology*, 314:41–44, 2017.
- [100] Naoomi Yamada, Taro Hitosugi, Junpei Kasai, Ngoc Lam Huong Hoang, Shoichiro Nakao, Yasushi Hirose, Toshihiro Shimada, and Tetsuya Hasegawa. Transparent conducting Nb-doped anatase TiO<sub>2</sub> (TNO) thin films sputtered from various oxide targets. *Thin Solid Films*, 518(11):3101–3104, 2010.
- [101] Mohammed Rasheed and Régis Barillé. Optical constants of DC sputtering derived ITO, TiO<sub>2</sub> and TiO<sub>2</sub>:Nb thin films characterized by spectrophotometry and spec-

- troscopic ellipsometry for optoelectronic devices. *Journal of Non-Crystalline Solids*, 476(May):1–14, 2017.
- [102] A. V. Manole, M. Dobromir, M. Gîrtan, R. Mallet, G. Rusu, and D. Luca. Optical properties of Nb-doped TiO<sub>2</sub> thin films prepared by sol-gel method. *Ceramics International*, 39(5):4771–4776, 2013.
- [103] J. Tauc. Optical properties and electronic structure of amorphous Ge and Si. *Materials Research Bulletin*, 3(1):37–46, jan 1968.
- [104] Maria Covei, Luminita Predoana, Petre Osiceanu, Jose Maria Calderon-Moreno, Mihai Anastasescu, Silviu Preda, Madalina Nicolescu, Mariuca Gartner, and Maria Zaharescu. Niobium/Vanadium doped TiO<sub>2</sub> multilayered sol-gel films: Structure, surface chemistry and optical properties. *Ceramics International*, 42(12):13805–13811, 2016.
- [105] M Bauch and T Dimopoulos. Design of ultrathin metal-based transparent electrodes including the impact of interface roughness. *Materials and Design*, 104:37–42, 2016.
- [106] Dong Geon Lee, Min-cheol Kim, Byeong Jo Kim, Dong Hoe Kim, Sang Myeong Lee, Mansoo Choi, Sangwook Lee, and Hyun Suk Jung. Effect of TiO<sub>2</sub> particle size and layer thickness on mesoscopic perovskite solar cells. *Applied Surface Science*, 477:131–136, may 2019.
- [107] Hao Lu, Kaimo Deng, Nina Yan, Yulong Ma, Bangkai Gu, Yong Wang, and Liang Li. Efficient perovskite solar cells based on novel three-dimensional TiO<sub>2</sub> network architectures. *Science Bulletin*, 61(10):778–786, 2016.
- [108] Peng Wang, Jing Zhang, Renjie Chen, Zhaobing Zeng, Xiaokun Huang, Liming Wang, Jie Xu, Ziyang Hu, and Yuejin Zhu. Planar Heterojunction Perovskite Solar Cells with TiO<sub>2</sub> Scaffold in Perovskite Film. *Electrochimica Acta*, 227:180–184, 2017.
- [109] Atsushi Kogo, Masashi Ikegami, and Tsutomu Miyasaka. A SnO<sub>x</sub>–brookite TiO<sub>2</sub> bilayer electron collector for hysteresis-less high efficiency plastic perovskite solar cells fabricated at low process temperature. *Chemical Communications*, 52(52):8119–8122, 2016.
- [110] Xinyi Zhang, Jianfeng Yao, Muataz Ali, Jing Wei, Huanting Wang, Leslie Y. Yeo, James R. Friend, and Douglas R. MacFarlane. UV/ozone-assisted low temperature preparation of mesoporous TiO<sub>2</sub> with tunable phase composition and enhanced solar light photocatalytic activity. *Journal of Materials Chemistry A*, 2(44):18791–18795, 2014.
- [111] Francesco Di Giacomo, Valerio Zardetto, Alessandra D’Epifanio, Sara Pescetelli, Fabio Matteocci, Stefano Razza, Aldo Di Carlo, Silvia Licocchia, Wilhelmus M.M.

- Kessels, Mariadriana Creatore, and Thomas M. Brown. Flexible perovskite photovoltaic modules and solar cells based on atomic layer deposited compact layers and UV-irradiated TiO<sub>2</sub> scaffolds on plastic substrates. *Advanced Energy Materials*, 5(8):1–9, 2015.
- [112] F. Di Giacomo, V. Zardetto, G. Lucarelli, L. Cinà, A. Di Carlo, M. Creatore, and T. M. Brown. Mesoporous perovskite solar cells and the role of nanoscale compact layers for remarkable all-round high efficiency under both indoor and outdoor illumination. *Nano Energy*, 30(October):460–469, 2016.
- [113] Daniel J.V. Pulsipher and Ellen R. Fisher. O<sub>2</sub> plasma treatment of mesoporous and compact TiO<sub>2</sub> photovoltaic films: Revealing and eliminating effects of Si incorporation. *Surface and Coatings Technology*, 203(16):2236–2242, may 2009.
- [114] Sanjib Das, Gong Gu, Pooran C. Joshi, Bin Yang, Tolga Aytug, Christopher M. Rouleau, David B. Geohegan, and Kai Xiao. Low thermal budget, photonic-cured compact TiO<sub>2</sub> layers for high-efficiency perovskite solar cells. *Journal of Materials Chemistry A*, 4(24):9685–9690, 2016.
- [115] Benjamin Feleki, Guy Bex, Ronn Andriessen, Yulia Galagan, and Francesco Di Giacomo. Rapid and low temperature processing of mesoporous TiO<sub>2</sub> for perovskite solar cells on flexible and rigid substrates. *Materials Today Communications*, 13(September):232–240, dec 2017.
- [116] H. C. Weerasinghe, P. M. Sirimanne, G. V. Franks, G. P. Simon, and Y. B. Cheng. Low temperature chemically sintered nano-crystalline TiO<sub>2</sub> electrodes for flexible dye-sensitized solar cells. *Journal of Photochemistry and Photobiology A: Chemistry*, 213(1):30–36, 2010.
- [117] Nam Gyu Park, Kwang Man Kim, Man Gu Kang, Kwang Sun Ryu, Soon Ho Chang, and Yu Ju Shin. Chemical sintering of nanoparticles: A methodology for low-temperature fabrication of dye-sensitized TiO<sub>2</sub> films. *Advanced Materials*, 17(19):2349–2353, 2005.
- [118] Atsushi Kogo, Yoshitaka Sanehira, Masashi Ikegami, and Tsutomu Miyasaka. Brookite TiO<sub>2</sub> as a low-temperature solution-processed mesoporous layer for hybrid perovskite solar cells. *Journal of Materials Chemistry A*, 3(42):20952–20957, 2015.
- [119] Th E. Weirich, M. Winterer, S. Seifried, H. Hahn, and H. Fuess. Rietveld analysis of electron powder diffraction data from nanocrystalline anatase, TiO<sub>2</sub>. *Ultramicroscopy*, 81(3-4):263–270, 2000.
- [120] Wheeler P. Davey. Precision Measurements of the Lattice Constants of Twelve Common Metals. *Physical Review*, 25(6):753–761, jun 1925.

- [121] Isabel Mesquita, Luísa Andrade, and Adélio Mendes. Perovskite solar cells: Materials, configurations and stability. *Renewable and Sustainable Energy Reviews*, 82(July 2017):2471–2489, 2018.
- [122] Giorgio Schileo and Giulia Grancini. Lead or no lead? Availability, toxicity, sustainability and environmental impact of lead-free perovskite solar cells. *Journal of Materials Chemistry C*, 9(1):67–76, 2021.
- [123] Juan-Pablo Correa-Baena, Michael Saliba, Tonio Buonassisi, Michael Grätzel, Antonio Abate, Wolfgang Tress, and Anders Hagfeldt. Promises and Challenges of Perovskite Solar Cells in Portable Applications. *Science*, 358(November):739–744, 2017.
- [124] Gill Sang Han, Seongha Lee, Matthew Lawrence Duff, Fen Qin, Minlin Jiang, Guangyong Li, and Jung Kun Lee. Multi-functional transparent electrode for reliable flexible perovskite solar cells. *Journal of Power Sources*, 435(May):226768, 2019.
- [125] Yuichi Kato, Luis K. Ono, Michael V. Lee, Shenghao Wang, Sonia R. Raga, and Yabing Qi. Silver Iodide Formation in Methyl Ammonium Lead Iodide Perovskite Solar Cells with Silver Top Electrodes. *Advanced Materials Interfaces*, 2(13):1500195, sep 2015.
- [126] Giuliana Giuliano, Sebastiano Cataldo, Michelangelo Scopelliti, Fabio Principato, Delia Chillura Martino, Tiziana Fiore, and Bruno Pignataro. Nonprecious Copper-Based Transparent Top Electrode via Seed Layer-Assisted Thermal Evaporation for High-Performance Semitransparent n-i-p Perovskite Solar Cells. *Advanced Materials Technologies*, 4(5):1–12, 2019.
- [127] Sebastian Svanström, T. Jesper Jacobsson, Gerrit Boschloo, Erik M.J. Johansson, Håkan Rensmo, and Ute B. Cappel. Degradation Mechanism of Silver Metal Deposited on Lead Halide Perovskites. *ACS Applied Materials and Interfaces*, 12(6):7212–7221, 2020.
- [128] Ranbir Singh and Mritunjaya Parashar. Origin of Hysteresis in Perovskite Solar Cells. In *Soft-Matter Thin Film Solar Cells*, volume 041111, chapter 1, pages 1–42. AIP Publishing, 2020.
- [129] Ossila. <https://www.ossila.com/en-eu/products/perovskite-ink-nitrogen>.
- [130] Chunxiu Zang, Hui Wang, Shihao Liu, Wenbin Guo, Letian Zhang, and Wenfa Xie. Efficiency enhancement in an inverted organic light-emitting device with a TiO<sub>2</sub> electron injection layer through interfacial engineering. *Journal of Materials Chemistry C*, 8(24):8206–8212, 2020.

- [131] Lin Zhou, Xiaohong Chen, Feng Zhu, Xinxing Sun, and Zhuo Sun. Improving temperature-stable AZO-Ag-AZO multilayer transparent electrodes using thin Al layer modification. *Journal of Physics D: Applied Physics*, 45(50), 2012.
- [132] Dong Yang, Ping Fu, Fujun Zhang, Nan Wang, Jian Zhang, and Can Li. High efficiency inverted polymer solar cells with room-temperature titanium oxide/polyethylenimine films as electron transport layers. *J. Mater. Chem. A*, 2(41):17281–17285, sep 2014.
- [133] Rabina Bhujel, Sadhna Rai, Utpal Deka, Gautam Sarkar, Joydeep Biswas, and Bibhu P. Swain. Bandgap engineering of PEDOT:PSS/rGO a hole transport layer for SiNWs hybrid solar cells. *Bulletin of Materials Science*, 44(2):72, jun 2021.
- [134] Michael Hengge, Konstantin Livanov, Natalia Zamoshchik, Felix Hermerschmidt, and Emil J W List-Kratochvil. ITO-free OLEDs utilizing inkjet-printed and low temperature plasma-sintered Ag electrodes. *Flexible and Printed Electronics*, 6(1):015009, mar 2021.
- [135] Lukas Kinner, Theodoros Dimopoulos, Giovanni Ligorio, Emil J.W. List-Kratochvil, and Felix Hermerschmidt. High performance organic light-emitting diodes employing ITO-free and flexible TiO<sub>x</sub>/Ag/Al:ZnO electrodes. *RSC Advances*, 11(28):17324–17331, 2021.
- [136] Emanuele Centurioni. Generalized matrix method for calculation of internal light energy flux in mixed coherent and incoherent multilayers. *Applied Optics*, 44(35):7532, 2005.
- [137] Leif A. A. Pettersson, Lucimara S. Roman, and Olle Inganäs. Modeling photocurrent action spectra of photovoltaic devices based on organic thin films. *Journal of Applied Physics*, 86(1):487–496, jul 1999.
- [138] David Ebner, Martin Bauch, and Theodoros Dimopoulos. High performance and low cost transparent electrodes based on ultrathin Cu layer. *Optics Express*, 25(8):A240, 2017.
- [139] Aleksandar D. Rakić, Aleksandra B. Djurišić, Jovan M. Elazar, and Marian L. Majewski. Optical properties of metallic films for vertical-cavity optoelectronic devices. *Applied Optics*, 37(22):5271, aug 1998.
- [140] P. B. Johnson and R. W. Christy. Optical Constants of the Noble Metals. *Physical Review B*, 6(12):4370–4379, dec 1972.







---

## LIST OF PUBLICATIONS

---

### Published:

**Selina Goetz**, Martin Bauch, Theodoros Dimopoulos, Stephan Trassl. *Ultrathin sputter-deposited plasmonic silver nanostructures*. *Nanoscale Advances*, 2, 869-877, 2020.

**Selina Goetz**, Rachmat Adhi Wibowo, Martin Bauch, Neha Bansal, Giovanni Ligorio, Emil List-Kratochvil, Christian Linke, Enrico Franzke, Jörg Winkler, Markus Valtiner, and Theodoros Dimopoulos. *Fast sputter deposition of MoO<sub>x</sub>/metal/MoO<sub>x</sub> transparent electrodes on glass and PET substrates*. *Journal of Materials Science*, 56, 9047–9064, 2021.

**Selina Goetz**, Daniella Mehanni, Neha Bansal, Bernhard Kubicek, Rachmat Adhi Wibowo, Martin Bauch, Christian Linke, Enrico Franzke, Jörg Winkler, Toby Meyer, Stephanie Narbey, David Stock, Markus Valtiner, and Theodoros Dimopoulos. *Low-Temperature-Processed Transparent Electrodes Based on Compact and Mesoporous Titanium Oxide Layers for Flexible Perovskite Solar Cells*. *ACS Applied Energy Materials*, 5, 5318–5330, 2021.

**Selina Goetz**, Rachmat Adhi Wibowo, Martin Bauch, Neha Bansal, Giovanni Ligorio, Emil List-Kratochvil, Christian Linke, Enrico Franzke, Jörg Winkler, Markus Valtiner, and Theodoros Dimopoulos. *Transparent electrodes based on molybdenum–titanium–oxide with increased water stability for use as hole-transport/hole-injection components*. *Journal of Materials Science*, 57, 8752–8766, 2022.

### Submitted:

**Selina Goetz**, Stefan Edinger, Christian Linke, Enrico Franzke, Jörg Winkler, Markus Valtiner, Theodoros Dimopoulos. *Humidity-driven degradation of sputtered molybdenum oxide and molybdenum-titanium-oxide thin films*. *Journal of Materials Chemistry C*, 2023.

